universität
wien

DIPLOMARBEIT

Titel der Diplomarbeit

Construction of a Multi-Anode Ionization Chamber for AMS at VERA

Verfasser

Josef Buchriegler

angestrebter akademischer Grad

Magister der Naturwissenschaften (Mag. rer. nat.)

Wien, 2013

Contents

List of Figures

List of Tables

Abstract

AMS (Accelerator Mass Spectrometry) is a technique to measure long-lived radionuclides with an extreme abundance sensitivity (e.g. $^{14}C/^{12}C \approx 1 \times 10^{-15}$). At the very end of the detection beamline, a high-resolution detector providing multiple energy loss signals, can obtain sufficient information for final identification of the individual ions at energies around 1 MeV/amu. The availability of thin, amorphous and homogeneous silicon nitride foils, used as entrance window, triggered a revival of ionization chambers. The energy resolution at low energies is no longer limited by additional energy loss straggling in the window.

Based on detailed investigations of recent experimental data for isobar separation of ^{36}Cl from ^{36}S and results of simulations, a new state-of-the-art gas ionization chamber comprising multiple anodes was designed and built at VERA (Vienna Environmental Research Accelerator).

The flexible, easy-to-modify design of the new chamber allowed to explore the influence of different geometrical parameters on the total energy resolution. One important outcome is that the gas contribution to the energy resolution is smaller than expected by previous evaluations (140 keV vs. 170 keV with 24 MeV chlorine/sulfur ions).

Measurement series with a variety of isotopes were performed to get information on the performance of the detector under realistic conditions. For the chlorine/sulfur isobars at 24 MeV an absolute energy resolution of 157 keV (0.66% relative resolution) could be reached. For beryllium/boron the resolution was 0.86% for 7.2 MeV ions. This is a significant improvement compared to the previously used compact ionization chamber (1.0% with 7.2 MeV Be/B and 0.86% with 24 MeV Cl/S).

In combination with the time-of-flight system at VERA, one configuration of the detector having a large entrance window improves the detection capabilities for measurements of heavy ions, e.g. ^{236}U at low energies.

Zusammenfassung

AMS (Beschleuniger-Massenspektrometrie für engl. „Accelerator Mass Spectrometry") ist eine Technik zum Nachweis von langlebigen Radionukliden mit sehr hoher Nachweisempfindlichkeit (z.B. $^{14}C/^{12}C \approx 1 \times 10^{-15}$). Ein Detektor mit hoher Energieauflösung und mehreren Energieverlustsignalen erlaubt die Identifizierung von Isotopen bzw. die Unterscheidung von Isobaren am Ende des Strahlenwegs einer Beschleunigeranlage bei Energien im Bereich von 1 MeV/amu. Durch die Verfügbarkeit dünner, amorpher und sehr homogener Siliziumnitrid-Folien, die als Eintrittsfenster zum Einsatz kommen, wurde die Entwicklung von Ionisationskammern neu belebt. Die hohe Energieauflösung bei niedrigen Energien wird nicht länger durch die zusätzliche Energieverschmierung im Eintrittsfenster eingeschränkt.

Ausgehend von Untersuchungen an neuen experimentellen Daten für die Trennung von ^{36}Cl von ^{36}S und Ergebnissen aus Simulationen, wurde bei VERA (Vienna Environmental Research Accelerator) eine moderne, aus mehreren Anoden bestehende Ionisationskammer nach Stand der Technik entworfen und gebaut.

Der flexible und leicht veränderbare Aufbau der neuen Kammer ermöglicht die Untersuchung des Einflusses verschiedener geometrischer Parmeter auf die Gesamtenergieauflösung. Ein wichtiges Ergebnis ist ein geringerer Gasbeitrag zur Energieauflösung als aufgrund früherer Auswertungen erwartet wurde (140 keV vs. 170 keV mit 24 MeV Chlor-/Schwefelionen).

Messserien mit unterschiedlichen Isotopen wurden durchgeführt, um Informationen über die Leistungsfähigkeit des Detektors unter realistischen Messbedingungen zu erhalten. Für Chlor-/Schwefel Isobare mit 24 MeV konnte eine absolute Energieauflösung von 157 keV (0.66% relative Auflösung) erreicht werden. Für Beryllium-/Borionen mit 7.2 MeV wurde eine Auflösung von 0.86% erzielt. Im Vergleich zur früher verwendeten Kompakt-Ionisationskammer ist das eine signifikante Verbesserung (1.0% mit 7.2 MeV Be/B und 0.86% mit 24 MeV Cl/S).

In Kombination mit dem Time-of-Flight System bei VERA konnten die Detektionsmöglichkeiten für schwere Ionen (z.B. ^{236}U bei niedrigen Energien) durch das Verwenden eines großen Eintrittsfensters verbessert werden.

1 Introduction

1.1 AMS

Accelerator Mass Spectrometry (AMS) is a measurement technique for counting trace isotopes with an extreme high level of sensitivity and selectivity [Kut90]. In most cases one is interested in the abundance ratio of a rare radionuclide to its stable isotope(s). The investigation of long-lived radionuclides is an important application of AMS in geoscience, climate and environmental research, archeology, medicine and astrophysics [FS93]. The most famous application is radiocarbon dating, for which ^{14}C is compared with its stable isotopes (^{13}C and ^{12}C).
AMS facilities used as beam producing facilities can also contribute to ion beam analysis (IBA) [AB05] where surfaces and thin films of matter can be inspected in a non-destructive way.

In general, AMS facilities consist of two mass spectrometers (injector, analyzer) linked with a tandem-accelerator. Basically, AMS uses the electromagnetic force ($\vec{F}$) acting on charged particles:

$$\vec{F} = q \left(\vec{E} + \vec{v} \times \vec{B} \right) \tag{1.1}$$

q ... charge of particle
$\vec{v}$ ... velocity of particle
$\vec{E}$ ... electric field
$\vec{B}$ ... magnetic field

AMS facilities allow to separate and identify the isotope under investigation by a series of filters. Negative ions are extracted from the ion source, where the sample material is sputtered by bombarding it with cesium. Since some elements do not form negative ions (e.g. nitrogen), this is a first filtering stage. Leaving the source, the ions are accelerated to keV-energies and pass an electrostatic analyzer, where a certain energy to charge ratio is selected. In a following injector magnet only ions with the right momentum to charge ratio are bent towards the accelerator. Together these two elements form the low energy side mass spectrometer.
The ions and molecules are then accelerated towards the positively charged terminal in the center of the accelerator, where they pass the stripper device. There, by flying through a foil or a section of low gas pressure, the ions lose electrons, molecules are dissociated and the particles' charge states are changed, respectively.

Leaving the terminal, the positively charged fragments are accelerated again towards the exit of the accelerator. Depending on their charge state, they have then got different corresponding kinetic energies:

$$E_{he} = (E_{inj} + q_{le}U_T)\frac{m_{he}}{m_{le}} + q_{he}U_T \qquad (1.2)$$

E_{inj} ... energy after injection magnet
q_{le} ... charge state at low energy side
q_{he} ... charge state at high energy side
m_x ... particle mass[a]
U_T ... terminal voltage

Now, the ions have gained kinetic energy in the order of some ten MeV, allowing for additional filtering, separation and identification of the isotopes.
The main filter incorporated into the high-energy side beamline is another bending magnet, selecting particles of certain magnetic rigidity, and another electrostatic analyzer for suppression of ions having wrong energy over charge ratios.
Finally, detection systems for ion identification are mounted.

1.2 VERA

The Vienna Environmental Research Accelerator (VERA) went into operation in spring 1996. The 3-MV-Pelletron tandem accelerator and most of the main components were built by National Electrostatics Corporation (NEC).
By now, two MCSNICS (Multi Cathode Source of Negative Ions by Cesium Sputtering), 45° electrostatic analyzers (r = 30 cm, E/q = 90 keV) and a 90° injector magnet (r = 45.7 cm, mE/q^2 = 17 MeV amu) with a multi beam switcher are available on the low-energy side. An analyzing magnet (r = 127 cm, mE/q^2 = 176 MeV amu) and an electrostatic analyzer (r = 200 cm, E/q = 4.4 MeV) are carrying out the filtering on the high-energy side. For specific detection purposes, four different beamline sections are accessible by a switching magnet (B = 1.66 T).

The design of VERA allows the measurement of most of the important radionuclides (^{10}Be, ^{14}C, ^{26}Al, ^{36}Cl, ^{129}I, ^{23x}U, ^{244}Pu) [SGK$^+$04]. It can also search for super heavy elements (SHE) [DFG$^+$10] and can deliver protons for PIXE [MRA$^+$08]. In figure 1.1 the main parts of the VERA facility are depicted.

---

[a] due to the law of energy conservation, the ions of interest get only the fraction m_{he}/m_{le} of the energy of the incident molecule with the mass m_{le} (m_{he} is the mass of the ion of interest after stripping)
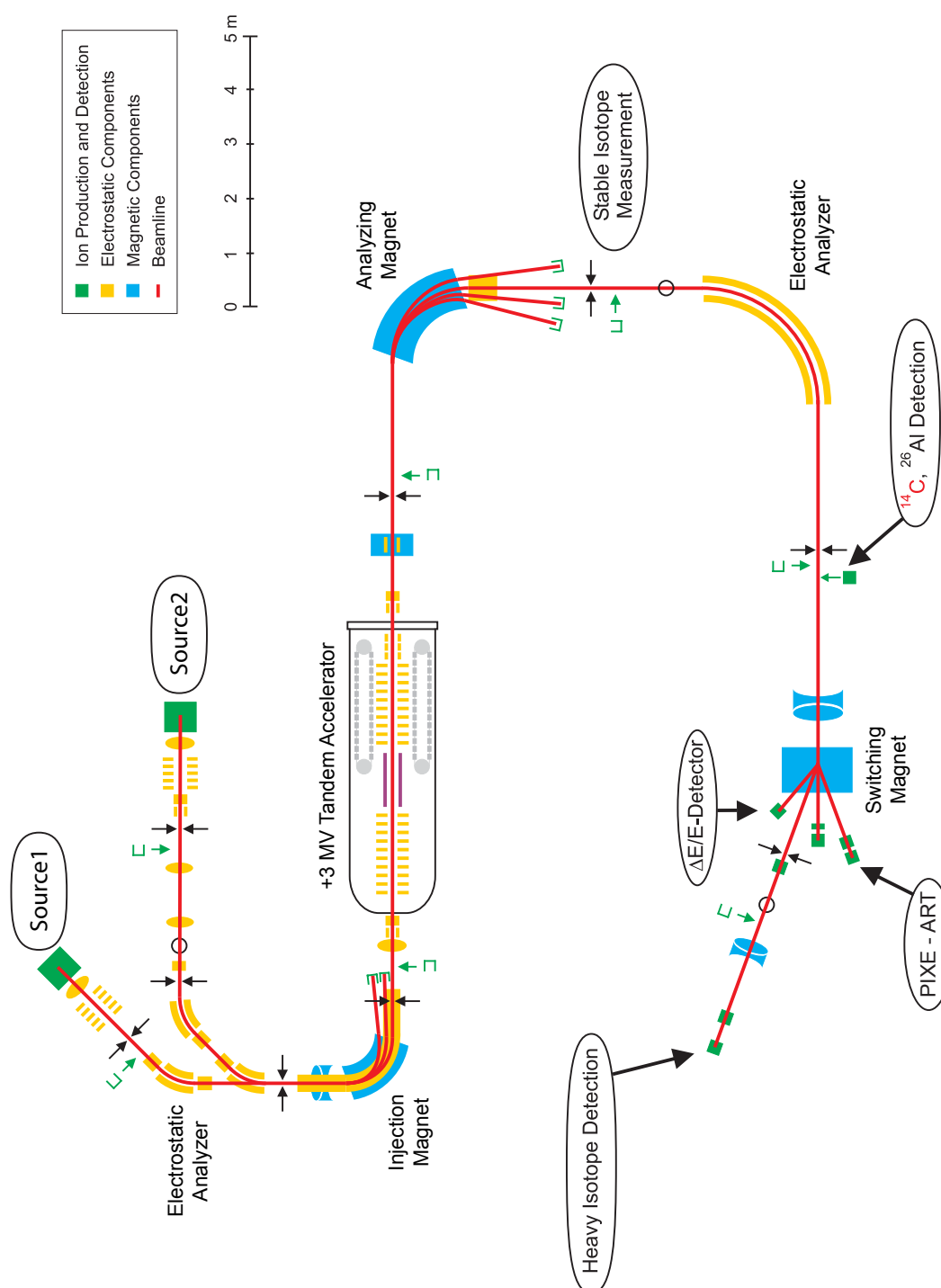
Figure 1.1: Overview of VERA in 2012 showing the main components.

1.3 Motivation for a new ionization chamber

Some years ago, the availability of thin, homogeneous silicon nitride membrane windows [Sil] made possible the use of ionization chamber for the identification of ions with energies much less than 1 MeV/amu. Using these windows, the AMS group of the ETH Zurich has demonstrated the increased performance of small ionization chambers, built for their low energy AMS systems [SSS07]. Especially, the achieved energy resolution encouraged the AMS group at VERA to build a compact ionization chamber with two anodes [FMA$^+$08]. This detector, based on the design of the ETH ionization chamber, was used in particular for the separation and identification of the isobars ^{36}Cl and ^{36}S.

Recent investigations of the suppression of sulfur against chlorine [Mar12] suggest an ionization chamber with a different anode design, optimized for high-resolution energy measurements. For optimum separation with the compact ionization chamber, the residual energy had to be measured with an additional energy detector behind the gas detector, introducing a decrease in total energy resolution by an exit window at the end of the chamber. One of the main intentions of building an ionization chamber with more anodes was to omit this separate residual energy detector. Furthermore, the compact design of the two-anode ionization chamber required relatively high gas pressures to stop the ions within its active volume. Hence, a thicker entrance window, withstanding the higher gas pressure was needed, which reduced the detector resolution additionally by angular and energy straggling.

Another design criteria for the new detector was the intention to achieve as high as possible beam transmission efficiency into the detector for AMS with heavy isotopes ($m > 100$ amu). At VERA, in front of the heavy ion detector, a time of flight (TOF) detector [VGK$^+$05] is used for particle identification. There the particles have to pass two thin foils (for start and stop signal generation, respectively), which blow up the transversal dimensions of the ion beam due to the angular straggling within these foils. Although a magnetic quadrupole positioned in the center of the TOF section partly compensates for this, a large entrance window of the detector is favorably to get most of the particles into the active detector volume.

To comply with very different requirements, a modular design of the new detector is desirable. The geometry of the anodes and the electrodes distances should be application-specifically adaptable with reasonable effort.
The detector performance for isotopes measured at VERA should be at least as good as that of the compact ionization chamber at energies around 1 MeV/amu. A flexible construction should also allow to study the influence of different detector parameters by their variation. Comparison of results obtained from measurements with calculations and simulations, respectively, should gain more profound understanding of the physics of ionization chambers at low energies.

2 Ions in matter

The main principle of any detector is a physical interaction to measure, for instance, energy or momentum of incoming particles (projectiles) or radiation. In our case electrically charged particles with kinetic energies of MeV are interacting via the coulomb force with gas molecules inside the active detector. They lose their energy mainly through ionization processes yielding charged particles (electrons and ionized gas), which can be collected by applying an electrostatic field. The produced amount of electrons and ions in the detector volume corresponds to the loss of energy of the decelerated projectiles.
In order to identify the incident particles, our aim is to gather informations about their typical energy loss characteristics inside the gas volume.

A small part of the particle's energy is lost to different processes which do not produce collectable charges. These are processes like excitation, rotation and vibration of molecules or atoms, elastic scattering, etc.

One also has to consider that interactions of the particles with residual gas in the beamline and the entrance window affect the beam's properties (e.g. energy and angular distribution) in advance.

I will give a brief summary of the most dominant processes relevant for gas ionization chambers within the typical energy range of about 1 MeV/amu used for AMS measurements at VERA.

2.1 Stopping power

The deceleration of fast moving charged particles in matter takes place in a large number of coulomb-interactions with electrons of the target material. These discrete processes of energy loss (ΔE) are depending on the particle's momentary energy. Due to their large number it is appropriate to treat this *stopping cross section* as a continuous function:

$$\mathcal{E}(E) = -\lim_{\Delta x \to 0} \frac{1}{N} \frac{\Delta E(E)}{\Delta x} = -\frac{1}{N} \frac{dE(E)}{dx} \qquad (2.1)$$

The denominator of this function is the product of the atomic density (N) and the thickness (Δx) of the regarding layer. It is called *areal density*:

$$\rho_A = N \Delta x \qquad (2.2)$$

This value allows a characterization of the target material neglecting density or geometrical issues. Usually, areal density is given in units of mg/cm² and can be varied by changing the pressure in case of gas targets.

The related *stopping power* (also called *specific energy loss*) is defined as

$$S(E) = -\frac{dE(E)}{dx} \tag{2.3}$$

2.1.1 Areal density vs. gas pressure

For experimental handling, the areal density is an inconvenient value. For detector gases similar to ideal gases (e.g. noble gases, isobutane in a certain range of temperature and pressure), the relationship can be expressed in terms of molar mass and pressure:

$$\rho_A = \frac{m_{mol}}{V_{mol}} \cdot x \cdot \frac{p}{p_0} \tag{2.4}$$

m_{mol} ... molar mass of the gas
V_{mol} ... molar volume at SATP[a](24.5 l/mol)
x ... thickness of stopping layer
p ... gas pressure
p_0 ... gas pressure at SATP

For example, 10 cm of isobutane (C_4H_{10}) at 30 mbar pressure corresponds to an areal density of 0.70 mg/cm² ($= \frac{(12 \cdot 4 + 1 \cdot 10) \times 10^3}{24.5 \times 10^3} \cdot 10 \cdot \frac{30}{1013}$).

2.1.2 Electronic stopping

The dominant stopping process for charged particles in a wide range of energies is electronic stopping. For non-relativistic particle velocities ($v \ll c$) the stopping power can be described by the *Bethe formula*:

$$-S_{electronic} = \frac{4\pi Z_P^2}{m_e v^2} \frac{e^4}{(4\pi\epsilon_0)^2} N Z_T \left[\ln\left(\frac{2m_e v^2}{I(1-\beta^2)} \right) - \beta^2 \right] \tag{2.5}$$

Z_P ... atomic number of the projectile
Z_T ... atomic number of the target material
v ... relative velocity between projectiles and target atoms
N ... atomic density of the target material
I ... mean excitation and ionization potential of the target atoms[b]
β ... ratio to speed of light (v/c)

---

[a]standard ambient temperature and pressure: 298.15 K/25°C and 101.3 kPa

This relation is limited to fully stripped particles with velocities higher than the classical velocity of the innermost electrons ($v_e = Z_P \cdot v_0$)[c]. Due to the small value of β ($\approx 4\%$), the last term in equation 2.5 can be neglected.

For lower velocities, the probability for electron capture by the projectiles increases and they are not fully stripped any longer. The charge state is fluctuating around an equilibrium charge, which depends on several variables (velocity, atomic number, density). This effective charge (Z_{eff}) of the projectile turns to lower values for decreasing velocities. It is difficult to calculate this value from a theoretical point of view, but semi-empirical formulas have been developed [Say77] to estimate the charge state depending on the projectile's energy.

Under these circumstances equation 2.5 has to be modified and reads:

$$-S_{electronic} = \frac{4\pi Z_{eff}{}^2}{m_e v^2} \frac{e^4}{(4\pi\epsilon_0)^2} N Z_T \ln\left(\frac{2m_e v^2}{I}\right) \qquad (2.6)$$

with

$$E_P = \frac{m_P v^2}{2} \rightarrow v^2 = \frac{2E_P}{m_P} \qquad (2.7)$$

and summarizing constants ($C = \frac{4\pi e^4}{m_e(4\pi\epsilon_0)^2} = \frac{e^4}{4\pi m_e\epsilon_0{}^2} = 7.601 \times 10^{-23}$ m^4 A V s^{-1}), this formula can be rearranged:

$$-S_{electronic} = C \, \frac{m_P}{2E_P} \, Z_{eff}{}^2 \, Z_T \, N \, \ln\left(\frac{4m_e E_P}{I \, m_P}\right) \qquad (2.8)$$

Under invariant conditions for the target material, the deposit of energy is proportional to $Z_{eff}{}^2$. Knowing this correlation, one can use measured characteristic energy loss information to distinguish between particles of the same energy and mass (equal velocity) but different atomic number (isobar separation).

2.1.3 Energy loss characteristics

Formula 2.8 predicts that the stopping power decreases roughly like $1/E_P$ for increasing particle energies. With increasing distance inside the target material, more and more kinetic energy is deposited and the velocity decreases. The maximum of energy loss, called *Bragg maximum*, is reached when the momentum transfer between projectile and target electrons is at its maximum. The mean time for interaction between projectile and target atoms becomes large because of decreasing projectile velocity, and electron pickup becomes significant. From this point onwards, the stopping power drops down proportional to the projectile's velocity. In figure 2.1 the typical shape of this so called *Bragg curve* is shown.

---

[b]mean energy requirement to form a electron-ion-pair (e.g. 23.4 eV in isobutane [IRC79])

[c]v_0 is the Bohr velocity $= \alpha \cdot c = 2.19 \times 10^6$ m/s ($\alpha \approx 1/137$, $c = 2.998 \times 10^8$ m/s)
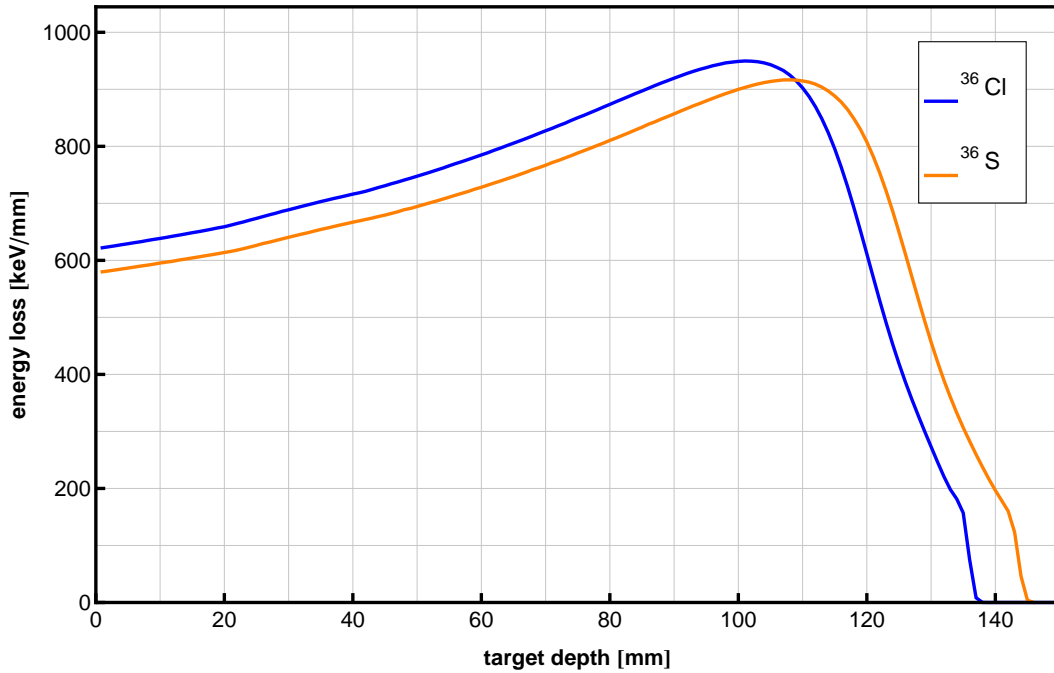
Figure 2.1: Mean stopping power for chlorine (blue) and sulfur (orange) projectiles against penetration depth in 100 mbar isobutane. Initial energy is 100 MeV. The plot is based on SRIM simulations.

At the very end of the stopping path *nuclear stopping* becomes the dominant process. This effect is typically a small part of the total energy deposited and does only partly contribute to the detector's signal via secondary ionization processes. It will not be discussed here in detail.

2.1.4 Straggling

For a sample of incident particles passing through matter its energy distribution and angular momentum is widened, because, both the amount of energy transfer and the number of interactions in the target material are statistical processes and cause so-called *energy loss straggling*.

For the separation of isobars, one is interested in the differential energy loss signals on several sections of the stopping range (cf. section 2.2.2). In this case energy loss straggling is a major limitation especially for heavy particles.

The statistical behavior is also the reason for *angular straggling*. The angular spread of the particles increases during the large number of interactions with the stopping matter. This angular widening of the ion beam has to be considered in the design of the detector geometry (see section 3.3.3).

2.2 Ionization chambers

The simplest model of an ionization chamber is a detector consisting of two parallel electrodes producing an intermediate constant electric field (see figure 2.2).
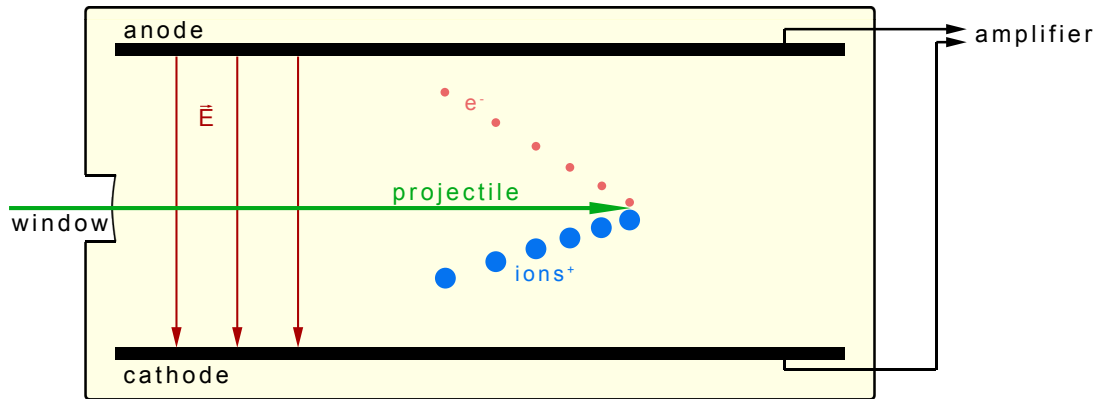
Figure 2.2: Schematic drawing of a simple gas ionization detector.

The volume between this anode and cathode is filled with a suitable gas, which does not form negative ions readily (e.g. argon, isobutane, mixtures with methane). A particle passing through the gas volume creates ion-electron-pairs, which are separated by the electric field. The moving charges induce a current on the anode and the cathode, respectively. The current on the anode is collected by a charge sensitive amplifier (the following signal processing chain is discussed in section 4.4).
The signal coming from the electrons is roughly proportional to the energy deposited in the gas between the plates. The remaining gas ions, traveling to the cathode about 1000 times slower than the electrons, induce a signal too. Because they are moving slowly compared to the electrons, their signal is usually not used to derive energy loss information.

2.2.1 Frisch grid

The rise time and the height of the anode's signal depend on the drift velocity of the electrons and on the distance from the place of ion-electron-pair creation to the anode, respectively. This dependency can be almost eliminated by placing a grid between the volume where ionization takes place and the anode.
This so called *Frisch grid* is composed of thin wires which can be arranged as grid [BCH49] or forming a mesh [Göö08], respectively. The creation of the anode's signal by the image charges of the electrons is postponed until the electrons pass through the grid. This means, that for the anode it looks as if all electrons were created at the same distance (the grid distance). The influence of the actual

charge production site on the signal's height is almost gone. Additionally, the influence of the positive gas ions, traveling to the cathode, is drastically reduced by the shielding of the grid.

Furthermore, the grid allows to apply different field strengths in the volume between anode and grid, and between grid and cathode. Thus, drift velocities in these detector volumes can be chosen to be different. This is important to achieve optimum detector resolution since the ratio of these field strengths has to be a compromise between several parameters (e.g. maximum anode voltage, shaping time, recombination probability, see section 3.3.3).
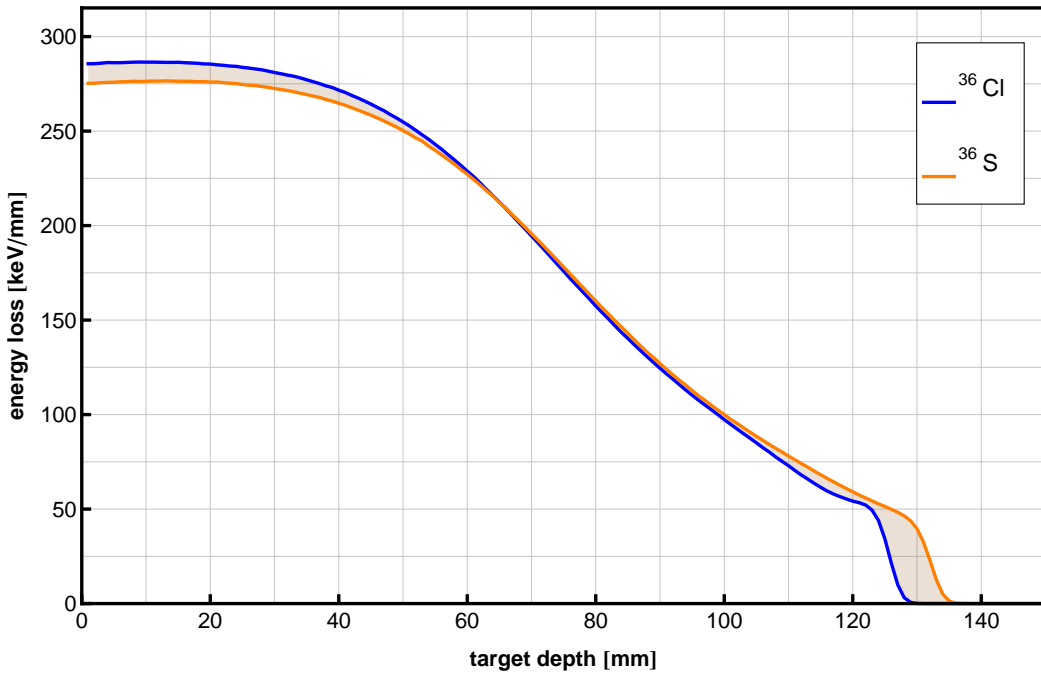
Figure 2.3: Isobars having different atomic number have different energy loss characteristics. The plotted curves show chlorine (blue) and sulfur (orange) in 30 mbar isobutane with 25 MeV initial energy based on SRIM simulations.

2.2.2 Anode splitting

For particle identification, the anode has to be split into several sections, to get more information on the shape of the Bragg curve. As shown in figure 2.3 and formula 2.8, the energy deposited in each section depends on the squared effective atomic number of the incident particle. The different anode's signals and their combined signal heights allow the creation of two- or multidimensional spectra facilitating the identification of different ions (see section 5.1.2).
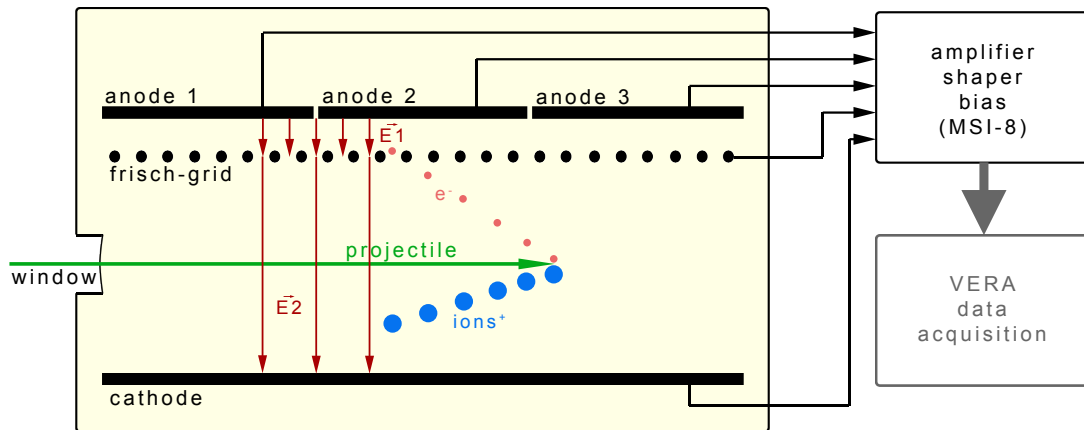
Figure 2.4: Schematic drawing of a 3-anode ionization detector with Frisch grid, $\vec{E}1$ and $\vec{E}2$ are the electric fields. The strengths are represented by the density of the arrows.

In case of diagonally split anodes, additional information on possibly scattered projectiles can be gathered. Due to their asymmetric trajectory a different amount of energy is deposited on the respective anodes. This technique is not yet applied in our new detector, but can be readily implemented. Meanwhile an aperture inside the active detector volume is used to suppress scattered projectiles having too much tilted tracks. In figure 2.4 the multi-anode design, the Frisch grid and the connection to the VERA data acquisition system are shown schematically.

2.3 SRIM

To allow predictions concerning the behavior of different types of ions in various types of stopping matter, one can use computer software including a lot of empirical data and the ability to deal with the theory of stopping power.

SRIM (Stopping and Range of Ions in Matter) is a famous computer program for calculating the interaction of ions in matter [ZB08]. The core of the simulation software is TRIM (TRansport of Ions in Matter), which is based on the Monte Carlo simulation method and allows to calculate the motion and interaction behavior of every type of ion in any kind of matter with lattice-like structure. The most important materials are already included in a so-called 'compound dictionary' containing (semi-)empirical data on their composition. It is also possible to compose own compounds by declaring parameters like atomic numbers, atomic weights and stoichiometry of the participating atoms.

The software became popular due to its easy-to-use user interface, where the input parameters can be adjusted in a structured way. Different types of calculations

and outputs can be selected. They are displayed and saved as plots or lists of parameters (see section 3.1.1).

The program package also contains tables and plots concerning experimentally determined ranges and stopping powers for the most common materials. In figure 2.5 a screenshot of SRIM during calculation is depicted.
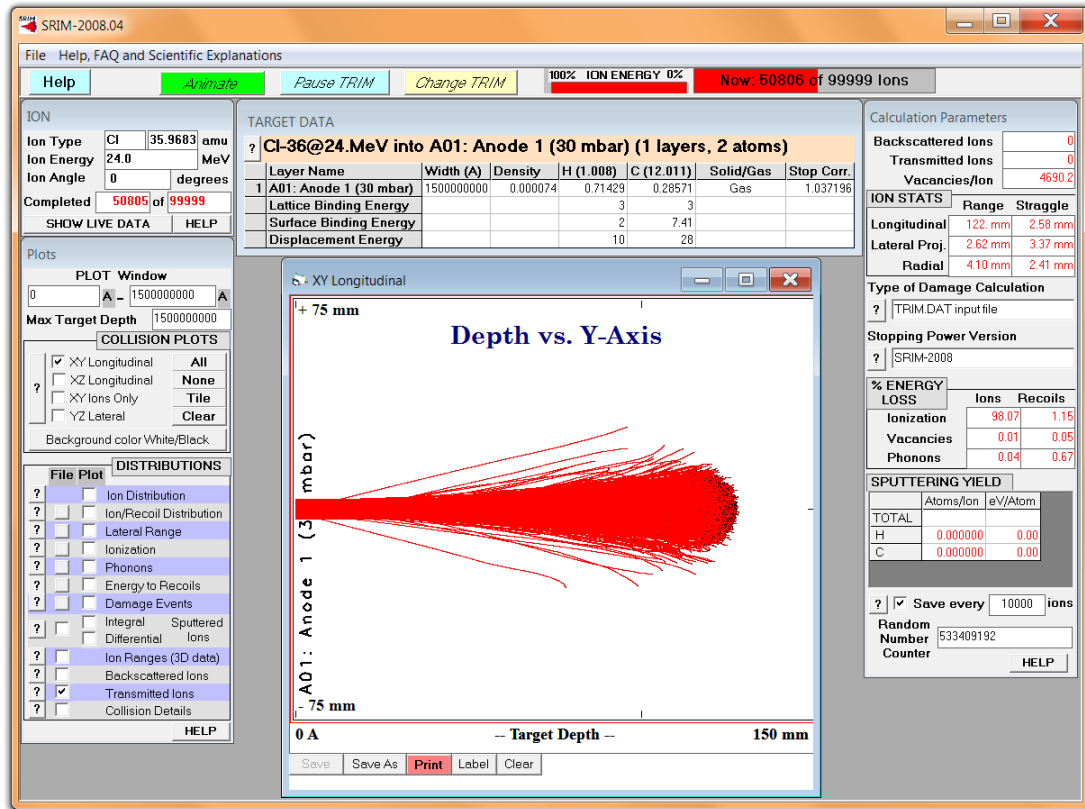
Figure 2.5: Screenshot of SRIM giving an impression of its abilities.

3 Planning phase

In order to meet all requirements for the new ionization chamber (cf. section 1.3), a lot of thought was given to gas handling, detector housing, easy operation, etc. Calculations and/or Monte Carlo simulations of the processes in the detector were performed to get more thorough understanding of basic principles, as well as to get a feeling for the influence of several effects on the detector performance under different detector geometries.

Start point for the design of the new detector were experiences with the already existing compact ionization chamber, used for AMS measurements with ^{10}Be and ^{36}Cl. We first reviewed the design of our compact detector. Together with a silicon strip detector behind it, full energy at low gas pressures and lateral displacement of the projectiles could be measured [Mar12, page 15 ff].

parameter	label[a]	value
total anodes length	l	60.0 mm
anode partitions	$a1/a2$	30.0/30.0 mm
anode width	b	47.5 mm
clearance anode-grid	p	5.0 mm
clearance cathode-grid	q	26.0 mm
grid wire diameter	$2r$	20 μm
grid wire spacing	d	0.5 mm
anode voltage	U_a	200 V
grid voltage	U_g	120 V
cathode voltage	U_c	0 V
field grid-anode	E_p	160 V/cm
field cathode-grid	E_q	46 V/cm

Table 3.1: Specifications of the compact ionization chamber

The dimensions as well as the typical voltages of the compact ionization chamber are listed in table 3.1.

---

[a]these variable names will be discussed and used in the following sections (cf. figure 3.5)

3.1 Simulations

In order to find the optimum dimensions of the active detector volume at realistic detector gas pressures, which silicon nitride windows can withstand, Monte Carlo calculations using SRIM-2008 were done. The following routine AMS-isotopes were simulated at different pressures in isobutane, entering the detector with their typical ion energies at VERA: ^{10}Be, ^{14}C, ^{26}Al, ^{36}Cl, ^{129}I, ^{236}U.
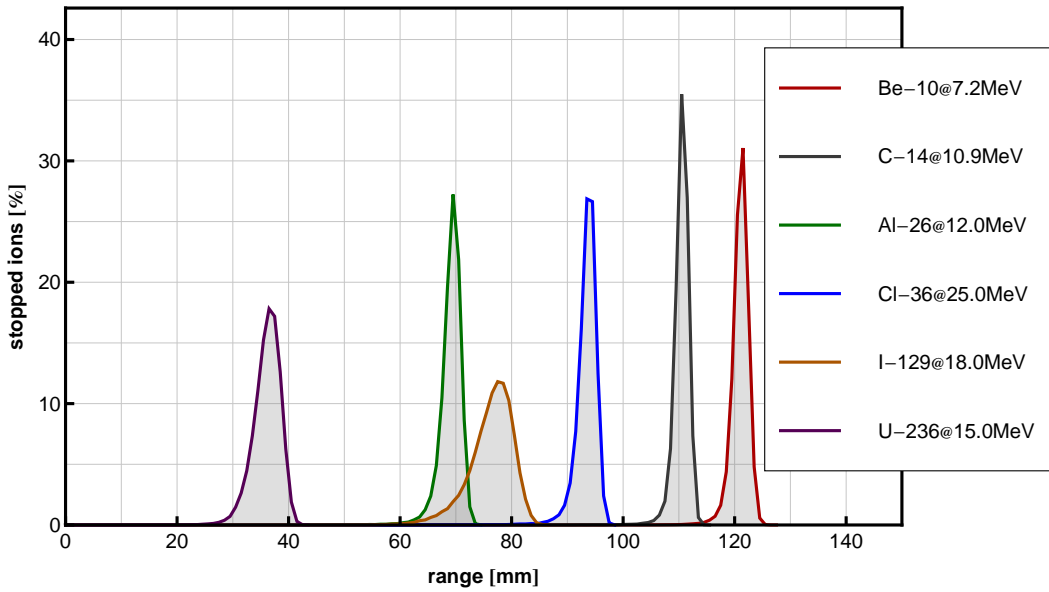
Figure 3.1: Ranges of the common AMS-isotopes at VERA in 40 mbar isobutane; the position where the ions are stopped finally, is shown against their relative occurrence, based on SRIM simulations.

As one can see in figure 3.1 an active length of 150 mm is sufficient to stop the common isotopes in isobutane at a pressure of 40 mbar. The transversal widening of a typical ion beam (2 mm FWHM[b]) increases inside the gas volume to about 7 mm FWHM near the end of the track (figure 3.2).

To achieve a homogeneous electric field in the area of ionization an adequate anode width of 30 to 50 mm appears sufficient. An optimum cathode to grid distance of about the same dimension makes possible the use of a 6-way cross (DN 160) as detector housing. This housing had to be mounted at the very end of the 20° beamline replacing an old Bragg-type detector.

---

[b]**F**ull **W**idth at **H**alf **M**aximum
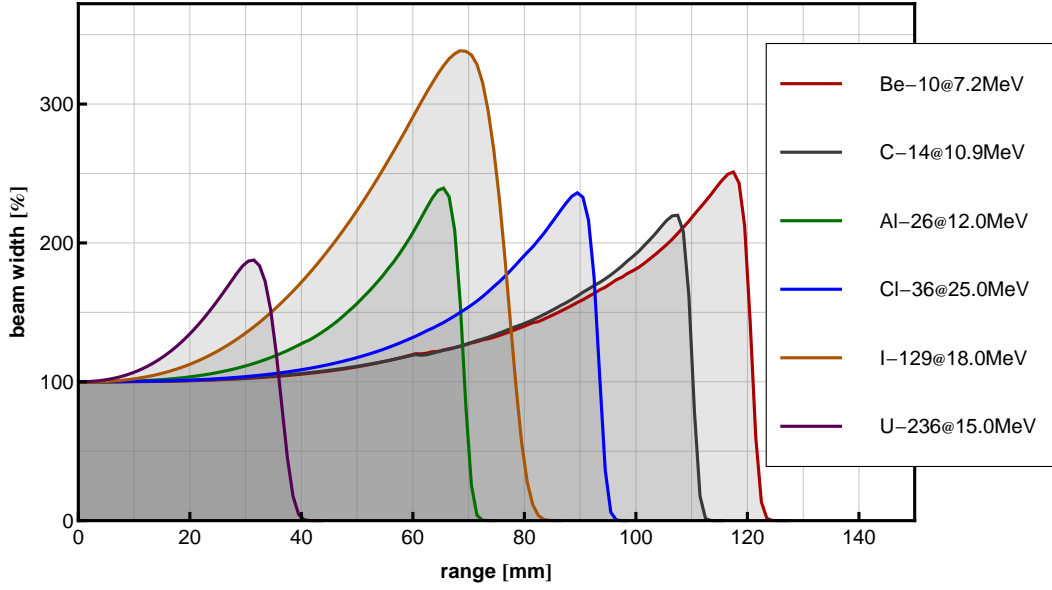
Figure 3.2: Widening of the beam inside the gas volume; the relative change of the beam diameter (FWHM) with increasing penetration depth is shown, based on SRIM simulations with a Gaussian beam profile (2 mm FWHM) in 40 mbar isobutane.

3.1.1 Handling of SRIM

It is laborious to get simulations with similar conditions by putting in the calculation parameters manually for each run. Therefore some kind of automation is desirable to prevent typing errors and to have a defined procedure of simulations. Additionally some discrepancies in simulations of multi-layer materials of very different thickness, observed in the past, are calling for a recipe to deal with. These discrepancies originate from inappropriately chosen step sizes by the program, when simulating layers with very different depths (e.g. entrance window + gas volume for an ionization chamber). Dividing the simulation into two single-layer steps leads to consistent results.

Therefore the output file, containing the ion parameters at the end of the first layer, has to be taken as input file for the next layer. The SRIM documentation states a compatibility of the output file ("TRANSMIT.TXT") format as input file ("TRIM.DAT") for further simulations. Aside from the first character in each line of the output file, this is correct.

Both, the ion's data (atomic number, mass, energy) and the target's data (thickness, composition of elements, density) can be modified and selected in the user interface and are stored in the file called "TRIM.IN". By setting the only value in the file "TRIMAUTO" to "1", the simulation can be started without further inputs by running "TRIM.EXE". Depending on the selected output parameters

(which are also stored in "TRIM.IN"), several output files are generated and stored in the subdirectories of SRIM.

Doing these modifications and formatting by hand is very monotonous and an inexhaustible source of errors. So this job is predestined for a computer program. To ensure a uniform modification of these files in every simulation, Mathematica seemed to be a suited programming environment to develop such programs.

3.1.2 Mathematica & AutoSRIM

Mathematica is a very powerful software used in a wide range of science and technical computing [Wol].

In first instance this platform was used as an environment to operate automated SRIM simulations. For this purpose I programmed Mathematica files to manipulate the in- and output files of SRIM. In an iterative process the code was developed and optimized to run TRIM taking all necessary parameters from a self defined configuration file (see example-file on page 87) and predefined TRIM.IN-files containing the target's properties. The simulation of multi-layers was automated also by programming modules for the re-formatting of the required in- and output files.

Finally these enhancements lead to a prosperous tool, which I called *AutoSRIM*. This set of Mathematica files allows to simulate several detector setups and ion types in an easy way. The results of the simulations can be viewed in a self defined log-file, where the most important informations are summarized. Additionally the output files of SRIM are modified and stored in a (file-)structure, which permits further evaluation of the simulation data. A series of Mathematica files has been created to explore different questions concerning the behavior of the ion beam in the detector. Most of the diagrams in this work based on SRIM simulations are generated using such evaluation files.

3.2 Peripheral equipment

3.2.1 Mounting & Operation

Because of multiple fields of operation of the detector, different types of entrance windows are needed. Especially for heavy ion detection in VERA's TOF-beamline [VGK+05] a large diameter is utile to achieve a high detection efficiency.
Isobar suppression and identification on the other hand requires very thin windows to minimize loss of resolution. Unfortunately thin windows with large diameters are not strong enough to withstand the required gas pressures. Therefore smaller windows and thus smaller window holders are needed for this kind of application. Hence, changing the detector window is a frequent task, which should be realizable with slight effort and within a reasonably short time.

We decided to put the whole detector housing onto slide rails with a rotatable mounting point. By pulling away the 6-way double cross and swiveling it out of the beamline, the window holder can easily be replaced.
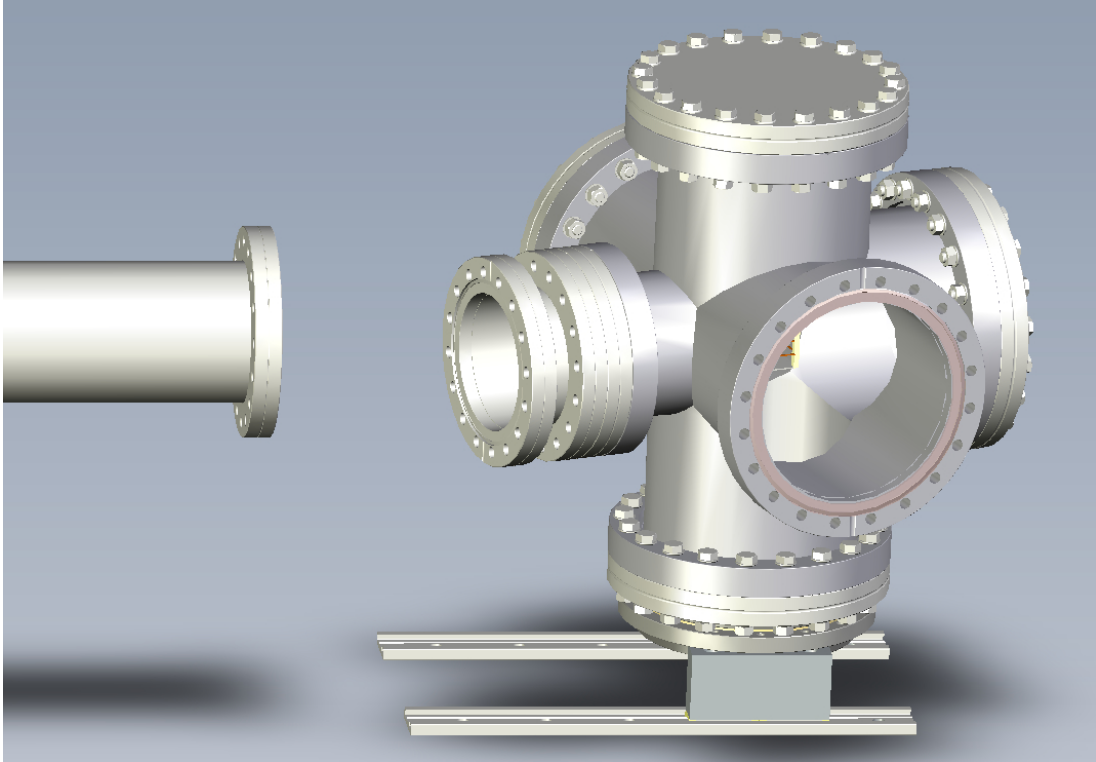
Figure 3.3: First design study of the housing and mounting of the planned detector (by Alfred Priller).

3.2.2 Gas handling

Different radionuclides need different steady gas pressures to achieve good measurement results. A constant areal density, and thereby a constant gas pressure, can be ensured by shutting-off the detector volume from the gas supply. Unfortunately in this case the counter gas slowly changes it properties due to outgasing of individual components or leakage (air and thereby oxygen can accumulate inside the detector housing). This affects the reproducibility and resolution of the measurement negatively.

The gas handling system, consisting of two metering valves and a PID-controller, can prevent this by a continuous throughflow of counter gas. At the first valve (metering-in) the flow rate and therefore the exchange rate of the gas inside the detector volume is adjusted. Connected to dedicated pressure sensors a PID-controller is regulating the pressure by manipulating the opening of the second

valve (metering-out). The detector is placed inside this regulated volume in between the valves. It has to be considered, that this technique is regulating the gas pressure and not the areal density. However, this is sufficient since the gas temperature stays almost constant.

Based on an existing gas handling system incorporating a commercial PID-controller and a mechanically adjustable metering-out valve, the construction of a new and modern gas handling system was initiated.

To allow maximum flexibility and expandability, the core of the new system has been realized in LabVIEW [Nat]. Running on a dedicated computer, this software is connected via a data acquisition (DAQ) box to all required parts of the system. The screenshot in figure 3.4 shows the user interface of the gas handling system in LabVIEW. The principal design and the actual state of the system is intuitively understandable.
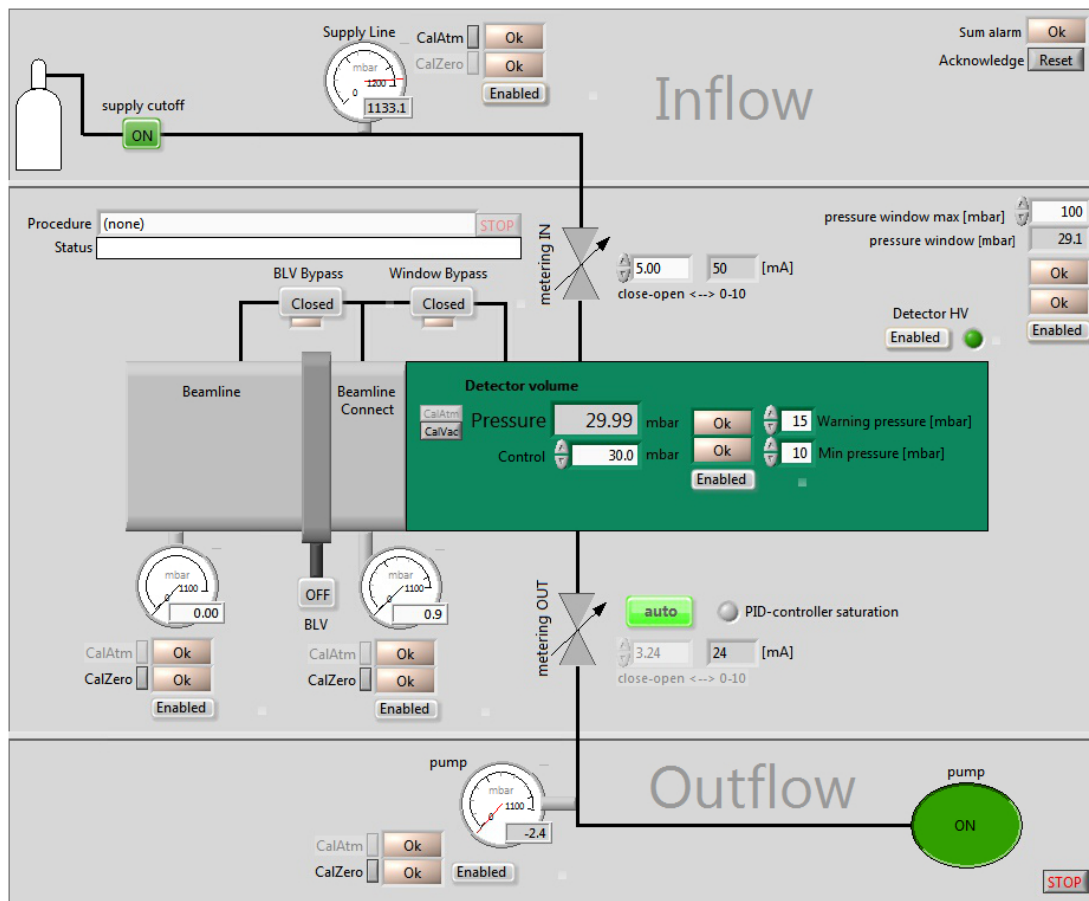
Figure 3.4: Screenshot of the gas handling system's user interface in LabVIEW.

Aiming to improve the detector resolution, a major enhancement of the new gas handling had to be a more stable pressure regulation. This could be realized

by optimizing the parameters of the software-based PID-controller. The metering valves used in the new setup are chosen especially for their typical regime of pressure and can be adjusted very sensitively by a current-controlled solenoid coil. A dedicated control board has been developed to assure these accurate requests of valve adjustments. The integration of a read back signal from the valves gives further monitoring options to the software.

The bypasses, needed for save connection and disconnection of the detector housing, are equipped with computer controlled servo-motors, which are also connected via a dedicated controller board to the DAQ-box.

The pressure in each of the volumes (beamline, beamline connect, detector volume - cf. figure 4.1) is read out by low-cost but high-performance pressure sensors controlled by special designed amplifier boards. They are mounted near the sensors to amplify the signals, before transmitting them to the DAQ-box using shielded cables.

With this degree of automation and the availability of many pressure sensors, it was advisable to implement a security system, which brings the system into a save state in case of emergency (e.g. run out of gas, breaking of the window, etc). By making the control computer accessible via the Internet, another welcome side effect is the ability for remote control of the gas handling system.

3.2.3 Electronics

For processing the detector signals, suitable electronics has to collect the pulses generated by the particles penetrating the active detector volume.

To prevent disturbing influence from any kind of electronics surrounding the detector, the current signals from the anodes have to be converted into voltage pulses and amplified near their place of creation. The preamplifier providing this impedance conversion is included in the Mesytec [Mesc] MSI-8 box, which is mounted directly on the detector's housing. So the pulses have to cover a distance in the range of 15 to 30 cm inside the gas volume. Special low-capacitive conductors were mounted inside the detector volume to avoid crosstalk between the individual signals, and to keep electronic noise as low as possible (see section 3.3.4).

The cable length outside the vacuum is reduced to about 15 cm (CF flange with sub-D feedthrough to Lemo plugs). The MSI-8 amplifier combines a preamplifier, a shaper, and a timing amplifier for eight channels individually. The output signal then is fed into the VERA data acquisition system.

3.3 Detector resolution

The total energy resolution (δE_{tot} = FHWM of the distribution of the measured energy loss values[c]) of the detection system is limited by different effects altering the final shape of the spectra. These effects can be regarded as statistically independent uncertainties of the measured energy signal height. These uncertainties will be discussed individually in more detail in the following sections.

$$\delta E_{tot} = \sqrt{{\delta E_{beam}}^2 + {\delta E_{window}}^2 + {\delta E_{geom}}^2 + {\delta E_{electr}}^2 + {\delta E_{gas}}^2} \qquad (3.1)$$

3.3.1 Ion beam

The width of the energy distribution of the ion beam provided by the accelerator, is mainly determined by the stability of the terminal voltage (equation 1.2). The FWHM of the ion beam was measured to be 0.05%. This corresponds to an uncertainty of 12 keV for typical chlorine and sulfur energies of about 24 MeV at VERA.

3.3.2 Window

In order to endure the gas pressure used for the compact ionization chamber (50 to 100 mbar), a 100 nm thick silicon nitride window with 5x5 mm membrane size is necessary to separate the detector's gas volume from the vacuum of the beamline.

Having enough space inside the 6-way cross of the new design, it is possible to make the anodes longer, which allows to use lower gas pressure for completely stopping the ions inside the active detector volume. The new design facilitates pressures for isobutane in the range of 20 to 40 mbar.

The lower gas pressure allows the use of thinner silicon nitride windows, which are also available with a nominal thickness of 50 or 30 nm. SRIM simulations were made to estimate energy loss and energy straggling due to these foils. The simulation results are shown in table 3.2.

Concerning the energy straggling (δE_{window}) the SRIM results have to be corrected, since these values are underestimated by 10 to 15% [Mar12, page 26 ff]. In doing so, the widening of the energy distribution can be estimated to 50 keV for 50 nm windows and 39 keV for 30 nm windows, respectively, for a 24.0 MeV sulfur/chlorine beam.

Another advantage using thinner foils is the higher remaining energy of the passed ions, especially for heavy ions.

---

[c]δ represents FHWM = 2,35σ (standard deviation)

isotope	thickness [nm]	ΔE [keV]	δE_{window} [keV]
^{36}Cl	100	597	65
^{36}S	100	574	59
^{36}Cl	50	299	44
^{36}S	50	288	43
^{36}Cl	30	179	34
^{36}S	30	173	34

Table 3.2: Energy loss (ΔE) and energy straggling (δE) in silicon nitride foils with different commercially available nominal thicknesses. The stated values are based on SRIM simulations with a density of 3.1 g/cm^3 [Mül09] and a stoichiometry of $Si_3N_{3.1}H_{0.06}$ [DKS$^+$04] (24.0 MeV initial energy).

3.3.3 Geometry

By studying the geometrical dependencies concerning the detector's behavior, several issues with optimization potential were found to be worth investigating in detail. The main geometrical parameters of the ionization chamber are shown in figure 3.5. For values of the compact ionization chamber refer also to table 3.1.
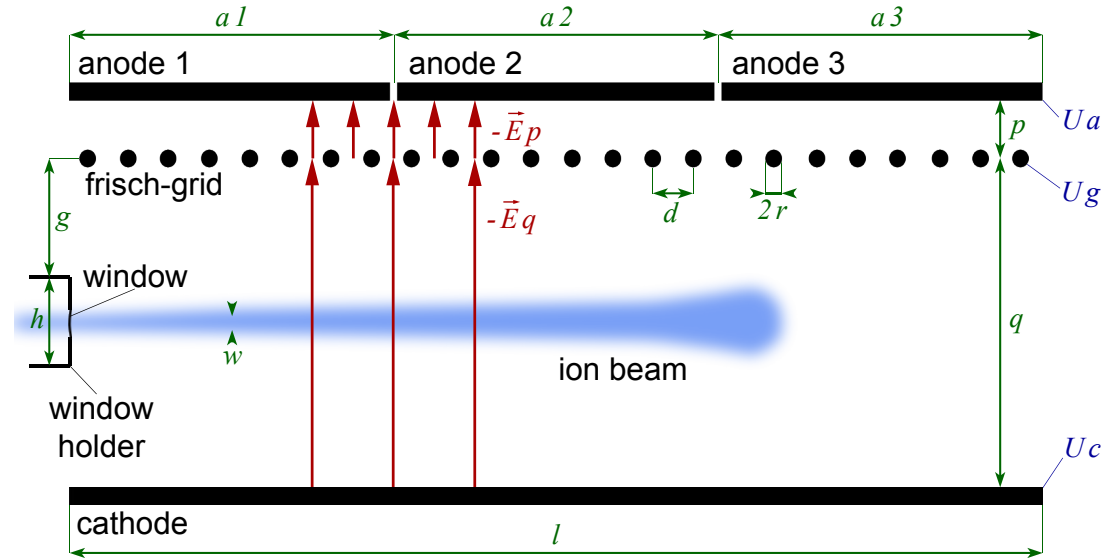
Figure 3.5: Sketch depicting the parameters used in the following sections to describe the influence of detector geometry on the detector resolution

The Frisch grid is substantially determining the signal forming process inside the detector, as introduced in section 2.2.1. One important purpose is to reduce the signal's dependency on the path length of the electrons between the place of

creation (ionization) and the anode. Another aim of the grid is the elimination of the influence of the positive gas ions on the anode's signal. Since the grid has to be permeable for electrons, the impact of the slowly traveling ions is still visible to a small extent in the anode's signal. Similar to the gas ions, the electrons also have a small influence on the anode before their passage through the grid. Both, the shielding of the electrons "behind" the grid and the ions' effect from perspective of the anode, are described by the *inefficiency* of shielding [BCH49]:

$$\sigma = \frac{dE_p}{dE_q} \approx \frac{d}{2\pi p} \ln\left(\frac{d}{2\pi r}\right) \tag{3.2}$$

For our compact ionization chamber this value is 3.3%. Studying equation 3.2 makes one recognize, that σ can be decreased by choosing a grid with minimal wire diameter and pitch. Despite of being desirable, it seemed to be hard to construct an even finer grid than that of the compact ionization chamber ($2r = 20\ \mu$m, $d = 0.5$ mm) with reasonable effort (see section 4.3.2). So the remaining adjustable parameter for optimizing the inefficiency is the distance between grid and anodes (p).

Additionally, there is an indirect influence of the inefficiency on the shape of the anodes' signals. Due to the lateral width of the ion beam (w) the place of ionization is fluctuating around the ideal beam path. This variation corresponds to the width of the beam entering the gas volume and increases along the stopping path according to the widening due to angular straggling (see figure 3.2). Based on calculations concerning the induced charge on the anodes [Göö08, page 38], the following relation was derived for the uncertainty of an anode's signal:

$$\delta E_{geom} \propto \Delta E \sigma \frac{w}{q} \tag{3.3}$$

with ΔE quantifying the total energy deposited at the corresponding anode.

As one can see in this formula, the variability of path length (e.g. 3.5 mm mean beam diameter[d] vs. 25 mm distance $\approx 14\%$) has to be multiplied with the value of the inefficiency. Therefore, the typical signal uncertainty due to this geometrical effect is small (in the per mill range). Nevertheless, the contribution of this effect will become sigificant for compact ionization chambers/geometries due to their short distance between the place of ionization and the grid. Not having a compact, parallel ion beam will make this contribution noticeable as well.

The impact of these uncertainties in drift path length are superimposed by effects of pulse shaping in the signal processing chain of the data acquisition. Adjusting the ratio of drift velocities, determined by the field ratio, may also contribute to minimize these geometrical effects.

---

[d]the widening of the beam due to angular straggling along the stopping path is worsening this value towards the end of the path

Apart from these arguments, calling for large distances of the electrodes, several effects necessitate to keep them as short as possible.

The height of the anodes' signals can be blurred by the diffusion of the electron cloud along their path to the anodes. Depending on field strengths and path length, this widening is in the range of 200 to 350 μm (FWHM). In the region of adjacent areas of the anodes, the transversal diffusion of the electrons may cause a contribution to the signal's height of the "wrong" anode. Detailed calculations (convolution of ionization density and distribution of electrons) demonstrated, that this effect is negligible for slowly changing ionization density. But at the end of the particle's path inside the gas volume, the ionization density is decreasing rapidly (cf. figure 2.3, page 22, approximately at a penetration depth of 130 mm). In case of an unfavorably chosen anode splitting or unsuitable gas pressure such that the end of the particles' paths is in the region of the anode's splitting, the coming anode's signal can be noticeably harmed by electrons associated to the previous anode. This distortion is that significant because of the small amount of energy, and thus electrons, remaining for the last anode, in comparison with the "spill-over" of electrons belonging to the previous anode. By adapting the gas pressure, this influence can be reduced to a negligible level (per mill range).

The longitudinal diffusion of the electrons along their drift path may also cause some smearing of the anodes' signal due to the spread in drift times.

Also with regard to the timing of the signals, the field strengths and the ratio (s) of upper (E_p) to lower (E_q) electrical field have to be taken in account, what strongly is related to the distances between electrodes and grid (p and q). The drift velocity of the electrons traveling to the anode depends on these field strengths and on the gas pressure (figure 3.6) [Ful79]:

$$v_{drift} = \mu p_0 \cdot \frac{E}{p} \tag{3.4}$$

where μ is the mobility of electrons at standard pressure p_0.

The amount of electrons passing the grid strongly depends on the field ratio, too, and has a significant influence on the detector's resolution (see experiments in section 5.2.4). By selecting a high enough field ratio ($\approx 2-3$, depending on the grid geometry) the fraction of electric field lines, which represent the ideal path of the electrons, ending on the grid can theoretically be reduced to zero [BCH49]. A small percentage of the electrons is however lost on the grid due to diffusion processes causing a divergence in their trajectories.

Field strength and pressure are also crucial for the probability of recombination. For higher density or lower electrical field, respectively, there is an increasing chance for electrons to neutralize with positive ions in the gas. This loss of electrons can noticeable harm the signal height on the anodes, what leads to poorer resolution due to incomplete collection of charges. Choosing a high enough lower field strength can diminish this probability to a certain extent.
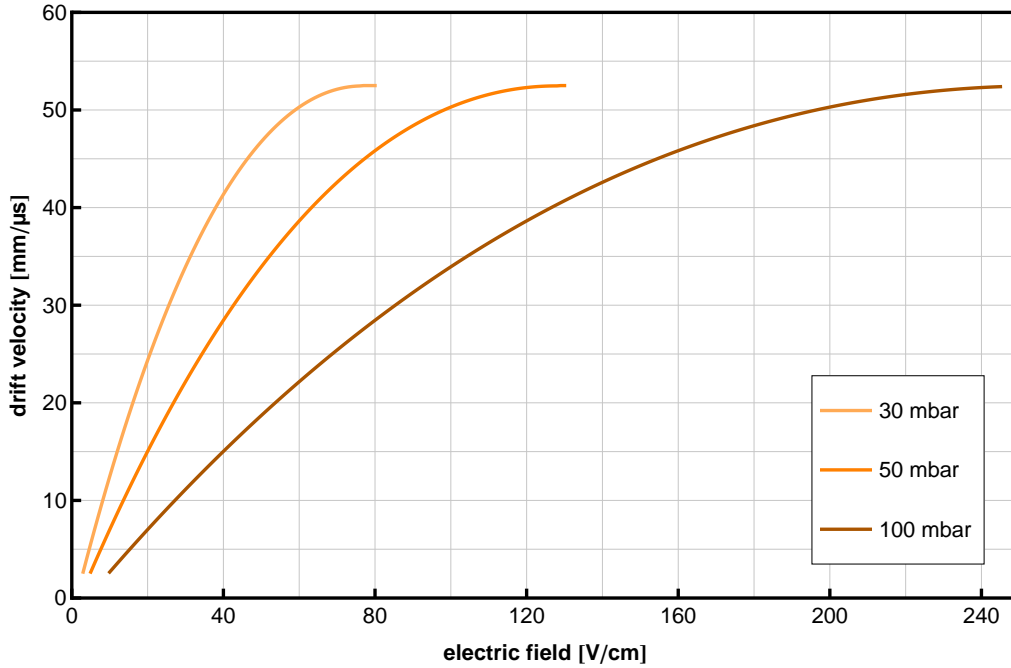
Figure 3.6: Drift velocity of electrons in isobutane for different pressures and typical electric fields, based on data by [SG78].

On the other hand, the field strength and thereby the ratio of fields cannot be arbitrarily increased, because the voltage is limited by the maximum bias voltage rated for the MSI-8 box (400 V). The distance between window holder and grid (g) is another constraint not to select a too high lower field strength (E_q). The potential of the window holder was chosen to be the same as the cathode's (U_c), to ensure, that all Coulomb force vectors point to the grid and no electrons are deflected in the wrong direction. Due to the small clearance between window holder and grid, the local field strength can reach critically high values. For small gas pressures, there is an increasing probability for gas discharges therefore. To avoid possible damage of the electronics, the security system of the gas handling system deactivates the voltage supply in case of falling gas pressure below a selectable value ($\approx 5-10$ mbar). The critical pressure for an electrical flashover depends on the type of gas and the effective field strength in the decisive region. This relation is described by Paschen's law [Pas89] and can be found in so called *Paschen curves.*

The capacity of the detector as well as the cable length between anodes and amplifier are consequences of the geometry and will be discussed in detail in the next section.

3.3.4 Electronic noise

A major part of the contribution of the electronics to the detector resolution is caused by the capacitance (C) of detector and cables.

For the detector the *capacitance* is proportional to the area of the electrodes and inversely proportional to their distance:

$$C_{plate} = \epsilon \, \frac{A}{p} \tag{3.5}$$

with *permittivity*

$$\epsilon = \epsilon_r \epsilon_0 \tag{3.6}$$

ϵ_r ... relative permittivity[e]
ϵ_0 ... vacuum permittivity
A ... area of the plate $(= l \cdot b)$

The total length (l) of the electrodes is mainly determined by the requirements to measure ions with certain energies at pressures, which are suitable for thin entrance windows. To provide an adequately homogeneous field in between the plates, the width (b) can not be made too small (see section 3.1). The remaining free parameter is once again the distance of the electrodes, whereby larger clearance will improve the detector's behavior concerning its capacity.

The cable's capacitance is described by the formula for coaxial geometry:

$$C_{cable} = \frac{2\pi\epsilon l_{cable}}{\ln(r_{wire}/r_{shield})} \tag{3.7}$$

with l_{cable} for the cable's length, r_{wire} for the conductor's half diameter and r_{shield} for the radius of the cable's shielding.

Outside the detector housing commercially available coaxial cables (LEMO[f]) with specified capacitance per length (100 pF/m) were used. It was our aim to make the distance, which the signal has to cover before entering the amplifier, as short as possible ($\approx 20 - 30$ cm inside the detector housing and about 15 cm between feedthrough and amplifier).

Inside the gas volume, specially constructed "pipes" where used to optimize the ratio between r_{wire} and r_{shield} and therefore to reduce the capacity (see section 4.3.3).

Another key value of the signal processing chain is the *shaping time*. This time is determined by the duration to collect all electrons belonging to one incident particle.

Increasing the electric fields inside the detector would allow to lower the shaping

---

[e]$\epsilon_r(gas) \approx \epsilon_r(vacuum) = 1$
[f]connector manufacturer, who has set several connector standards

time due to the higher resulting drift velocity of the electrons. The rise time for typical distances ($q/2 + p \approx 20 - 35$ mm) and fields ($E_q \approx 20 - 60$ V/cm and $E_p \approx 80 - 250$ V/cm) is in the range of 300 to 900 ns. For signal forming only the upper part of the path (p) is relevant and so the shaping time usually is chosen to be 0.5 or 1 μs. In order to allow high count rates (several 10^3 cps[g]), the shaping time has to be short. But decreasing it also results in higher electronic noise.

For our Mesytec[h] amplifier incorporating charge sensitive preamplifier modules ("MMPR1 for 35 MeV") [Mesb], the noise in keV (FWHM) is specified by the following formula:

$$N_{electr} = (N_0 + C_{det} \cdot N_s) \cdot \sqrt{1/\Delta t} \tag{3.8}$$

N_0 ... noise factor at capacity 0 (= 2.7 keV)
N_s ... noise factor slope (= 0.031 keV/pF)
C_{det} ... capacity ($C_{plate} + C_{cables}$) [pF]
Δt ... shaping time (FWHM) [μs]

The equation is intended to calculate the uncertainty of silicon semiconductor detectors (3.6 eV per charged couple). The result has to be rescaled for the different yield of charge carriers in isobutane (23.4 eV per charged couple - cf. section 2.1.2):

$$\delta E_{electr} = f_{corr} \cdot N_{electr} = 6.5 \cdot N_{electr} \tag{3.9}$$

with $f_{corr} = 23.4/3.6$.

For typical values ($C_{plate} = 1.2$ pF, $C_{pipe} = 4$ pF, $C_{cable} = 15$ pF, $\Delta t = 1$ μs) the electronic noise is about 22 keV for each anode. The contribution of the plates to the total capacity is negligible compared to the cables capacitance. Hence, reduction of cable lengths has to be the most important goal.

Of course this electronic noise has to be considered for each anode individually. For three anodes this leads to a total contribution of $22 \cdot \sqrt{3} \approx 38$ keV for total energy measurements. Therefore, the reasonable number of anodes is limited since the total contribution of electric noise scales with their square root.

3.3.5 Detector gas

Unfortunately the major contribution to the detector's resolution is the least assessable one. The statistical behaviour of the stopping processes in the gas leads to energy and angular straggling, as already mentioned in section 2.1.4.

The energy loss distribution caused by energy straggling has been well studied for alpha particles and light ions since the 1940s. This uncertainty in energy loss is the main limitation for the differential energy determination in ionization

---

[g]counts per second
[h]Mesytec GmbH & Co. KG, www.mesytec.com

chambers. For high velocities (above the Bragg maximum) the effects can be calculated and are well reproducible. For heavy ions, which are not fully stripped and change their charge state during the stopping process, the straggling effects can not be calculated straightforward. Especially at low energies accurate calculations are not available. Based on empirical data [SBH78] the straggling's contribution to the uncertainty can be estimated to be 300 to 400 keV for energies of about 10 MeV typically deposited on an anode's partition. This is in the range of a few percent and thus the most dominant effect worsening the resolution of the single anode's signals. For larger energy losses the situation becomes better due to the focusing effect of the projectiles. Particles depositing less energy in the earlier section of the path through the gas, lose more energy in the later sections and the other way round.

For full energy stopping this straggling effect is not relevant since it cancels when summing up the signals from the individual anodes. Nevertheless the detector gas significantly influences the resolution by additional smearing of the energy signal due to the ionization process. The number of created electron-ion-pairs is fluctuating around a mean value, which is determined by the mean ionization energy (I) to form such a coupled pair (cf. section 2.1.2). For a typical energy loss (on average 24 MeV) about 10^6 electrons are available for the signal forming process. The relative uncertainty of this value is generally described by the Fano formula:

$$\sigma_{rel} = \sqrt{\frac{F \cdot I}{\Delta E}} \tag{3.10}$$

with F the Fano factor[i].
This corresponds to an uncertainty of less than 12 keV (FWHM).

But similar to the straggling effects, this theory is an insufficient description for heavy particles and low energies. Furthermore, the growing influence of nuclear stopping in the actual energy range and competitive excitation mechanisms are not taken into account by the Fano formula.

It would require detailed investigations to disentangle all effects contributing to the uncertainty caused by the gas. An extensive appraisal of measurements performed under similar conditions [Mar12] led to a value of about 170 keV for the uncertainty originated by the gas in case of fully stopping 24 MeV particles. Focusing on optimization of directly changeable parameters of the ionization chamber, this value was adopted, to assess the resolution of the planned detector.

The use of alternative counting gases was not investigated in this work. Studies concerning this topic were made recently [Mar12, page 40 ff]. They indicate, that isobutane is a good compromise regarding different properties (drift velocity, isobar separation, availability, handling, etc.).

---

[i]the Fano factor depends on the target material and was experimentally determined to be 0.26 for isobutane [PBC97]

3.3.6 Design conclusions

Although different contributions to the total uncertainty can be treated individually, especially the geometrical parameters have an impact on all parts of formula 3.1. In table 3.3 a comparison of different detector setups concerning their total energy resolution for sulfur at 24 MeV is shown. The values have been calculated considering all the mutual influences discussed above. "MAIC.0"[j] is as similar as possible to the setup of our compact ionization chamber ("CIC") for the purpose of comparison. The column "MAIC.1" is listing all parameters, which were finally used in the first measurements (see section 5.1). In column "MAIC.2" and "MAIC.3", variations of the detector geometry under similar field conditions are shown.

In addition to the contributions discussed above, the count rate has a fundamental effect on the detector's behavior. Increasing the count rate (10^4 cps[k] and more) is reducing the energy resolution. Due to the slowly traveling gas ions in between grid and cathode, the electric field strength is reduced, what results in decreasing drift velocities of the electrons. Furthermore, the presence of slowly drifting ions is increasing the probability for recombination. This reduces the number of collectable electrons per incident particle available for the signal forming process. From this point of view, high electric fields, thus high drift velocities and a small distance between beam path and cathode would be desirable.

As on can see, it is difficult to accurately assess all different contributions. Depending on the actual application different effects will be dominant. On this basis a flexible geometry seems to be advisable in order to allow customized setups.

---

[j]MAIC was chosen to be the new detector's name: **M**ulti **A**node **I**onization **C**hamber
[k]counts per second

	CIC	MAIC.0	MAIC.1	MAIC.2	MAIC.3	
total length (l)	60.0	60.0	150.0	150.0	150.0	mm
1. partition	30.0	30.0	50.0	50.0	50.0	mm
2. partition	-	60.0	100.0	100.0	100.0	mm
anode - grid (p)	5.0	5.0	7.0	7.0	11.6	mm
grid - cathode (q)	26.2	26.2	49.0	39.0	39.0	mm
gas pressure	55	55	30	30	30	mbar
anode voltage (U_a)	200	200	250	214	263	V
grid voltage (U_g)	120	120	175	139	139	V
cathode voltage (U_c)	0	0	0	0	0	V
upper field (E_p)	160	160	107	107	107	V/cm
lower field (E_q)	46	46	36	36	36	V/cm
field ratio (s)	3.5	3.5	3.0	3.0	3.0	
inefficiency (σ)	3.30	3.30	2.36	2.36	1.42	%
upper drift velocity	52	52	52	52	52	mm/μs
lower drift velocity	29	29	38	38	38	mm/μs
upper drift time	95	95	133	133	221	ns
lower drift time	446	446	638	508	508	ns
total drift length	18.1	18.1	31.5	26.5	31.1	mm
mean particle energy	24.0	24.0	24.0	24.0	24.0	MeV
ΔE at anode 1	10	14.0	13.0	13.0	13.0	MeV
ΔE at anode 2	10	8.0	8.4	8.4	8.4	MeV
ΔE at anode 3	-	1.4	2.2	2.2	2.2	MeV
window thickness	100	100	50	50	50	nm
shaping time	0.5	0.5	1.0	1.0	1.0	μs
δE_{beam}	12	12	12	12	12	keV
δE_{window}	70	70	50	50	50	keV
δE_{geom}	60	64	25	31	19	keV
δE_{electr} (all anodes)	46	53	38	38	38	keV
δE_{gas}	170	*170*	*170*	*170*	*170*	keV
δE_{tot}	200	202	183	184	183	keV
energy resolution	0.86	0.86	0.78	0.78	0.77	%

Table 3.3: Comparison of different detector setups concerning their total energy resolution measuring sulfur/chlorine ions. Based on estimations discussed in section 3.3. Red values have been taken from [Mar12] (CIC = compact ionization chamber).

4 Construction

4.1 Gas handling system

The development of the new gas handling system was done within the framework of two bachelor theses[a] at VERA. During the main steps of the project, I was involved to coordinate the work concerning its compatibility with our new ionization chamber.
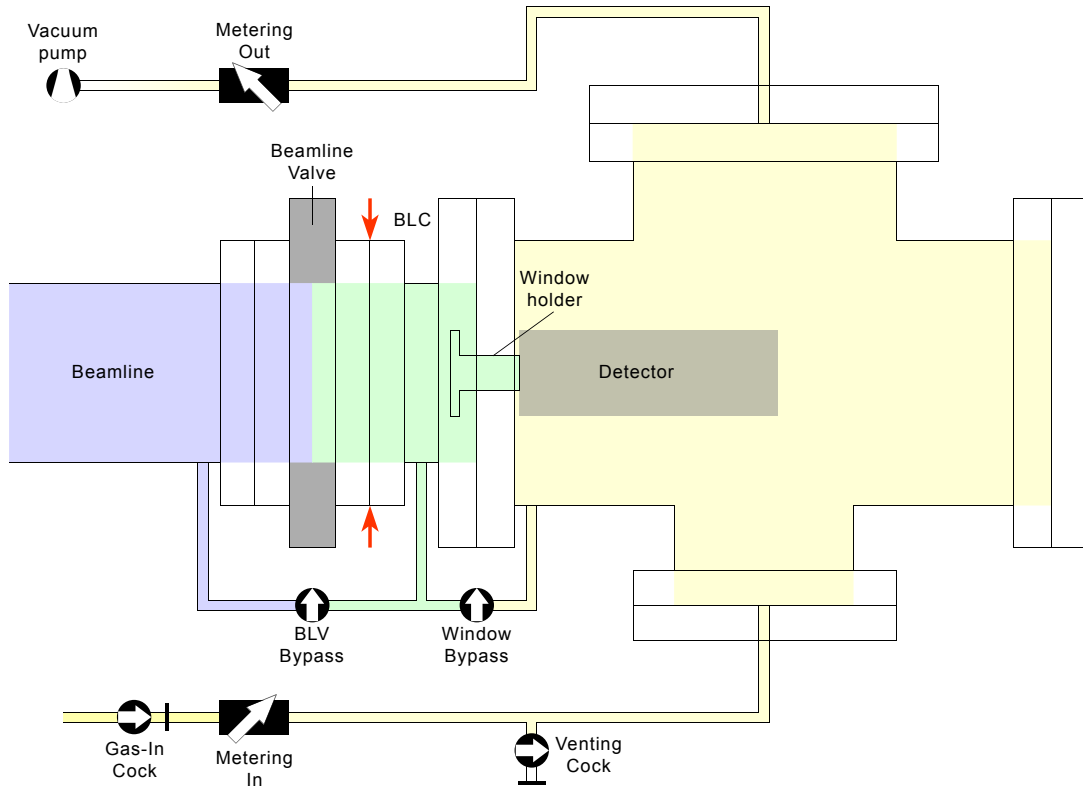
Figure 4.1: Diagram depicting the volumes of the gas handling system (blue = beamline, green = beamline-connect, yellow = gas volume of the detector), the orange arrows indicate the position, where the detector housing can be dis-/connected from the beamline.

In principle the gas handling system monitors three volumes separated by a beamline valve (BLV) and the entrance window of the detector. In figure 4.1 the relevant parts of the beamline and the detector housing are depicted true to scale in top view, whereas the bypasses and the gas-lines are shown schematically.

The metering valves and the bypasses are computer controlled, as discussed in section 3.2.2. In case of system failures (e.g. power outage), the bypass valves can be operated manually also. The metering valves are closing without current supply, what saves the present state of pressure. Under normal operation conditions, there is no need to change the valve position of gas-in or venting cock. These valves are necessary for procedures only, where detailed check lists or computer assisted procedures should prevent any wrong usage (venting or evacuating the detector volume for exchange of the entrance window).

The gas-in line starts with a bottle, containing up to 5 kg (= 14.3 l) isobutane, where a regulator provides the gas with constant pressure ($\approx$ 1200 mbar). Near the bottle a storage container ($\approx$ 15 l), buffering gas, allows the exchange of the gas bottle during detector operation. With 6 mm stainless steel pipes the gas is distributed along the different beamlines to potential places, where a detector needing a gas supply may be operated. For compatibility with existing detectors, these ports are realized as KF-16[b] flanges with a quarter turn cock (gas-in cock) in front.

The metering valves (RME 005 A from Pfeiffer Vacuum) had to be chosen with adequate gas rate capacity. Depending on the difference in pressure, where the valves have to operate, the regulation range is typically given in units of [mbar l/s] or [sccm][c]. For a pressure difference of about 1170 mbar (gas supply pressure - detector gas pressure) at the metering-in valve, the type with a flow rate ranging from 0.0017 to 0.17 mbar l/s is suitable. For a typical flow rate of 0.1 mbar l/s, one bottle of gas is enough for an operation time of more than 200 days. Due to the small difference in pressure at the gas-out line (detector gas pressure - vacuum) a metering valve type with a higher flow rate range of 0.085 - 8.5 mbar l/s is necessary.

Last part of the gas-out line is a scroll pump (Agilent SH-110[d]) evacuating the tube after the metering-out valve.

The construction of the gas lines was an important part of my work, giving me the opportunity to learn more about the handling of pipes and tubes, adapting pipelines to given facts, efficient use of fittings and junctions, and especially, dealing with vacuum. Before using the new lines for isobutane, evacuation and an extensive leakage test took place.

The bypasses are necessary for venting and evacuating procedures. To ensure

---

[b]vacuum flange type for high vacuum (HV, $10^{-3} - 10^{-7}$ mbar)

[c]standard cubic centimeter per minute

[d]pumping speed $\approx$ 60 l/min in the range of a few mbar, ultimate pressure: 6.6×10^{-2} mbar

equal change of pressure on both sides of the entrance window, the opened window bypass prevents inadequate force on the thin window. Venting or evacuating the detector volume has to be done very carefully, to beware of pressure gradients destroying the window.

Similar to the window bypass, the BLV-bypass guarantees a balance of pressure between beamline and the volume between BLV and detector window (beamline-connect = BLC). In this case, the bypass should prevent stressing the turbo pump on the beamline side, when opening the beamline valve. By connecting the volumes via the bypass first, not all residual gas molecules can enter the beamline simultaneously because of the small cross-section.
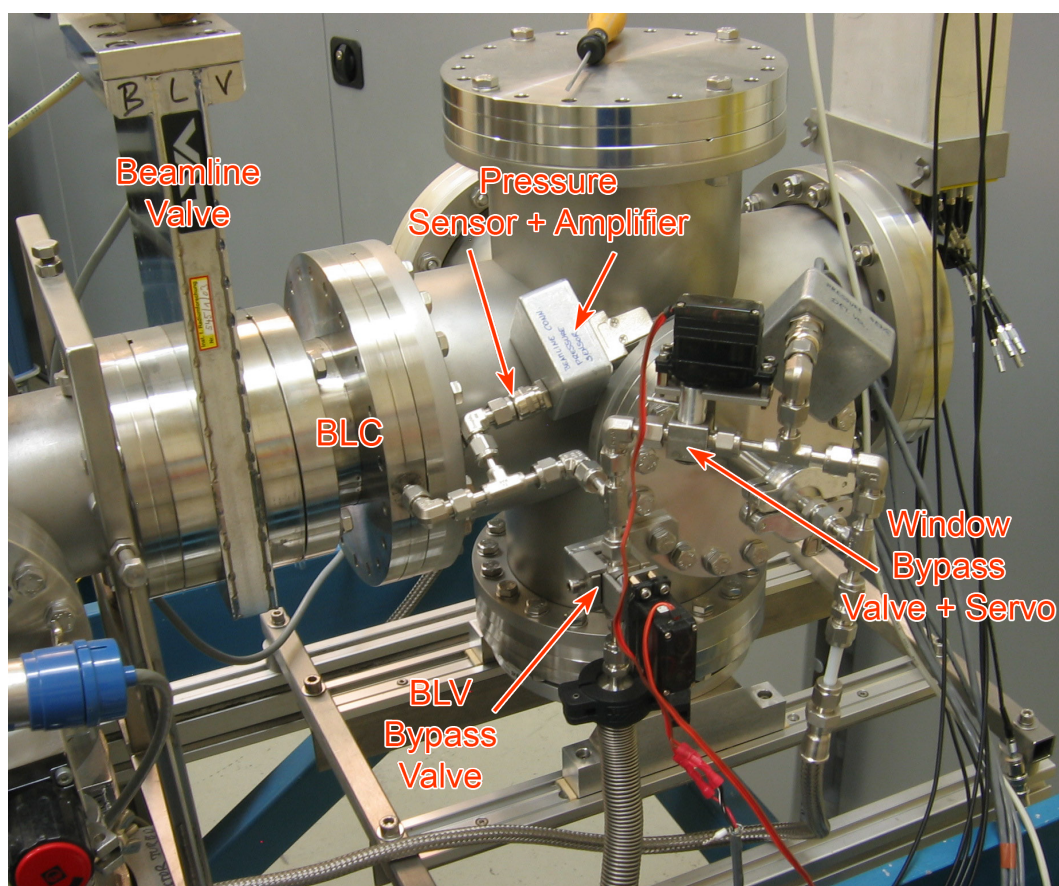
Figure 4.2: Assembly of the bypasses fixed on the detector housing.

In figure 4.2 one can see, how the assembly of the bypasses and the model depicted in figure 4.1 compare to each other.

With the exception of the PVC-tube between the metering-out valve and the vacuum pump, all parts containing detector gas are made from stainless steel to avoid any contamination by outgasing components. The major part of the fittings needed for the gas lines and the bypasses are built by Swagelok® components.

The development of the gas handling system, especially the electronics, was done in a test setup by the bachelor students. After wiping out most of the teething troubles, the parts have been assembled in a 19" rack pictured in figure 4.3.
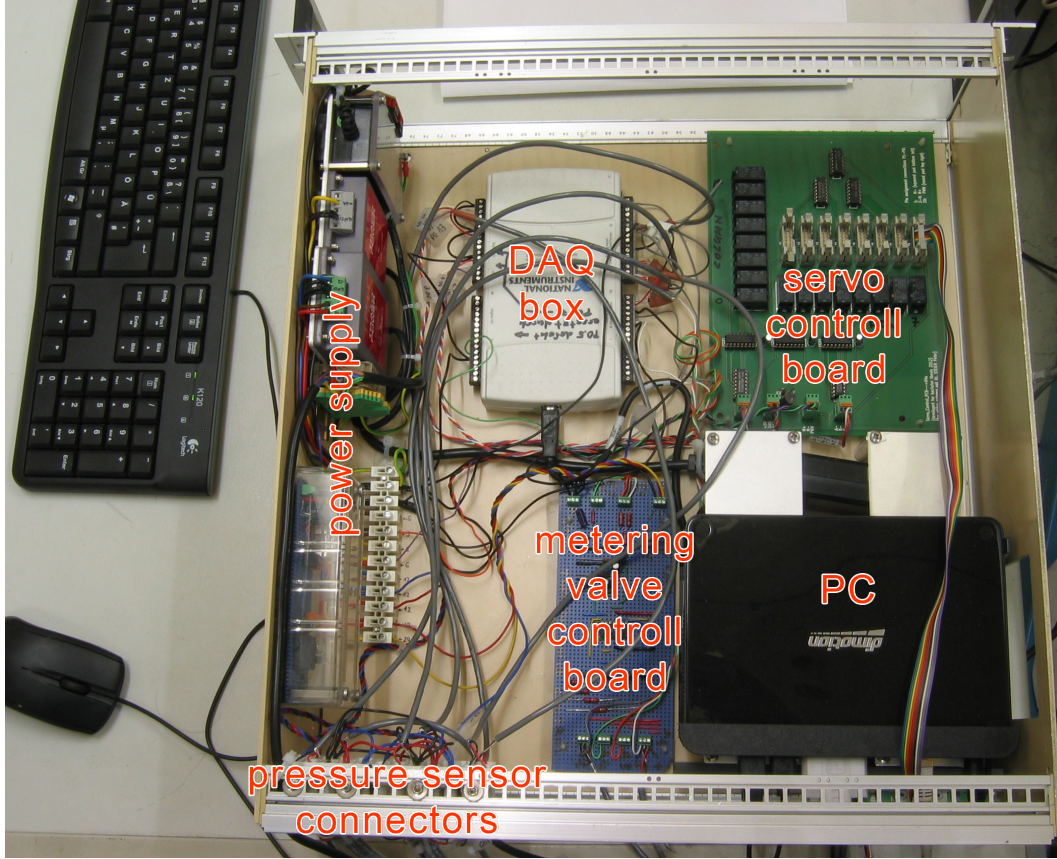
Figure 4.3: Picture of the rack containing most of the gas handling system electronics (cf. section 3.2.2).

4.2 Detector housing

The detector housing was chosen to be a 6-way CF[e] cross consisting of stainless steel (steel grade AISI 304) with 5 DN160 flanges (3 of them rotatable) and one DN100 flange. This number and size of ports allow a flexible and easy working in the volume, where the detector has to be installed.

The DN100 flange (inner diameter = 100 mm) originally was planned to be connected in the direction of the beamline. By modeling the arrangement of the new

---

[e]ConFlat vacuum flange type for ultra high vacuum (UHV, $10^{-7} - 10^{-12}$ mbar)

detector inside the housing with SolidWorks[f], it turned out, that mounting the detector in one of the larger flanges (inner diameter = 150 mm) would increase flexibility and avoid problems concerning the risk of electrical discharges.

The feedthroughs, necessary for the gas handling, are realized by KF-16 tubulations. They were welded into the center of blank flanges by the VERA-workshop. Flexible hoses with braid reinforcement and a core of stainless steel are connecting the detector volume with the metering valves. These bendable linkage allows to remove the detector housing from the beamline, without disconnecting the gas lines.
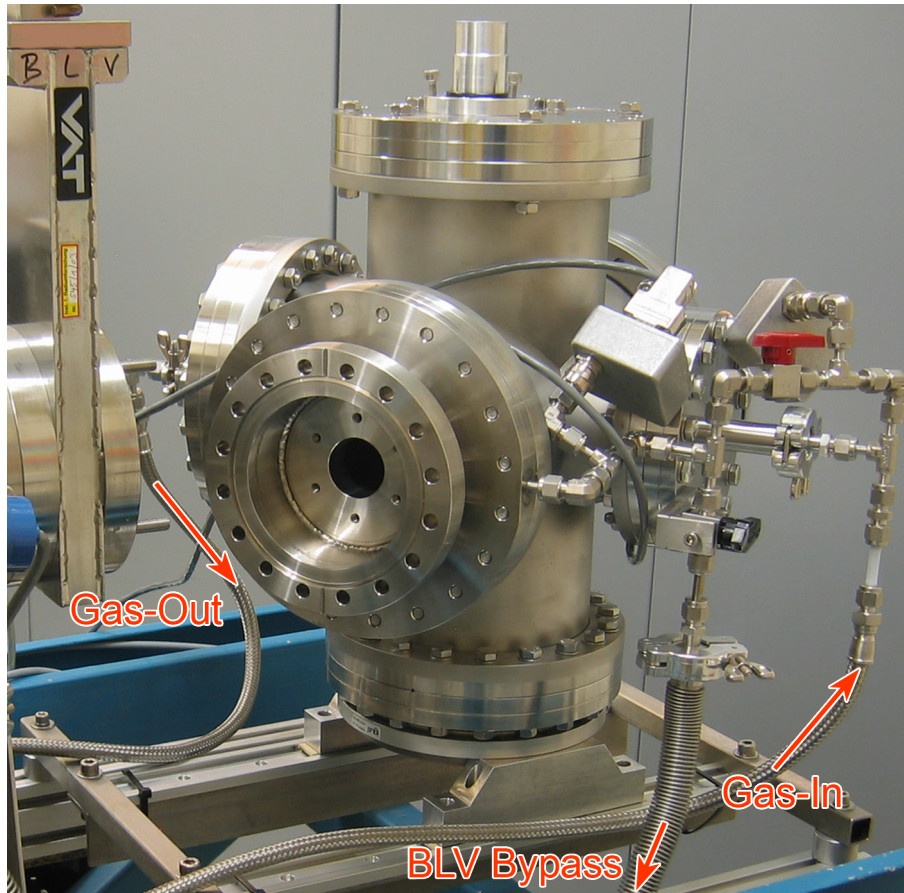
Figure 4.4: Opened detector housing, ready for the installation of a window holder, this picture was taken in an early stage of assembling.

On the bottom flange of the housing a rotary table (Igus®) is mounted on slide rails to allow to pull back and swivel it. The construction carrying this structure and the swiveled out detector housing is depicted in figures 4.2 and 4.4.
The connection piece (BLC) between the 6-way cross and the beamline, hosting

---

[f]3D computer-aided design (CAD) program

the window holder, was assembled in our workshop, too. On the detector's side, the flange has threaded holes to save space. Using nuts would hamper the closing and opening procedures of the detector housing. In order to make the BLC-volume accessible via bypasses, a channel has been drilled through the larger blank flange. At the end a welded pipe socket is supporting the bypass construction.

An insulated mounting of the detector housing was another objective to be obtained. Separating the housing's potential allows better handling of electric influences originating from other components along the beamline. This insulation is realized by using plastic KF clamps, intermediate PTFE[g] pieces, insulating foils, and non-conductive slide bearings, respectively.

The construction carrying the detector is attached to the rear flange (looking in beam direction). Two steel support rods, which are screwed into the rear flange, snap into recesses on the front flange when the whole detector is pushed into the housing. The electrical feedthroughs are situated in the rear flange, too. This simplifies taking out the detector for maintenance work (e.g. modification of geometrical parameters or anodes). The pipe-construction assembled for optimum signal transmission inside the detector housing is discussed in section 4.3.3 in detail.

The use of different kinds and sizes of entrance windows (cf. section 3.2.1), calls for window holders with various diameters. Three types of holders consisting of aluminum have been produced in our workshop to handle the common window sizes (5×5 mm, 10×10 mm, see figure 4.5) used at the VERA laboratory. The biggest type of window holder, having a circular orifice with 25 mm inner diameter, is intended especially for heavy isotope measurements. Each of the
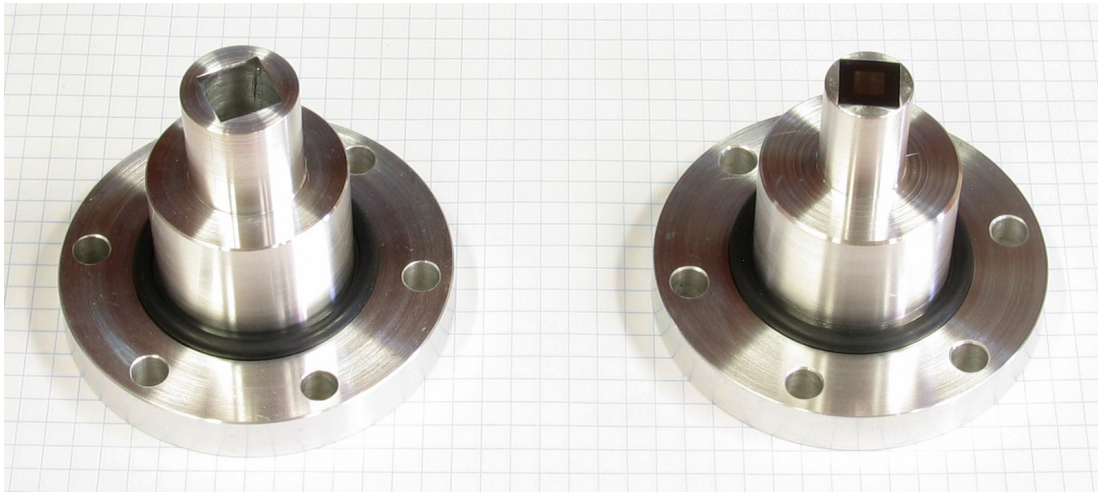
Figure 4.5: Window holders for medium (left) and small (right) windows. On the latter, a 5x5 mm silicon nitride window (10x10 mm frame size) is glued on.

---

[g]polytetrafluoroethylene ("Teflon")

holders is fixed by 3 or 6 screws from the BLC side and seals the detector volume
by an O-ring. The respective window has to be attached at the end of the nozzle
with a two-component glue.

Similar to the gas lines, a leakage test of the detector housing was done to
guarantee tightness of the new casing. Ports to be opened frequently like the BLC
to beamline connection or the rear flange of the detector housing, are sealed with
flat gaskets consisting of FKM[h]. All other ports are sealed with copper gaskets.
Vacuum tightness of all potentially leaking parts was checked with helium.

4.3 Detector

Before the production of the main parts of the new detector took place, detailed
three-dimensional studies have been made to evaluate difficulties that might be-
come obvious during manufacturing. In figure 4.6 the essential components are
depicted and labeled.
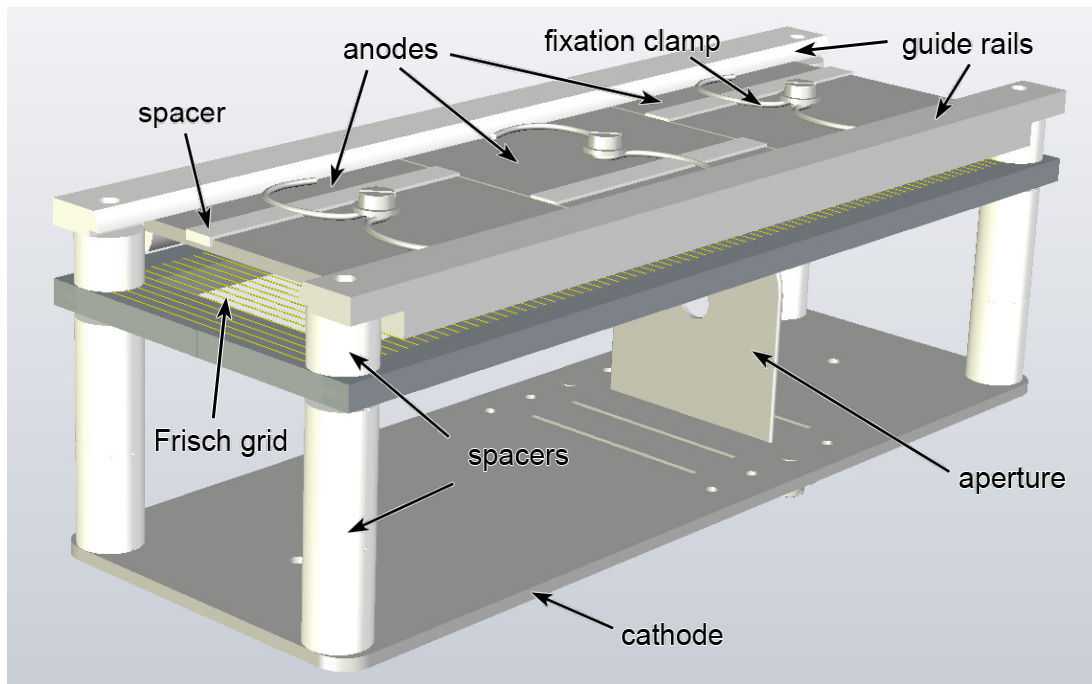
Figure 4.6: 3D model of the detector based on a SolidWorks drawing by Alfred Priller.

Basically our aim was to assemble a detector avoiding any materials that would
deteriorate the quality of the counter gas due to outgasing. This limited the choice
of suited materials and the options to bond parts. For example, the use of glue
has been avoided where possible.

---

[h]fluorocaoutchouc

4.3.1 Cathode & Anode design

All electrodes are made of 2 mm thick stainless steel. The cathode (150×40 mm) was equipped with several slots for putting in an optional aperture at different places. Threaded rods are linking the detector's bottom in a height-adjustable way with the support construction of the housing.

For the first measurements we decided to split the anode into three parts (each 50 mm). Due to the mounting of the anodes in guide rails, the detector is prepared for any thinkable configuration of anodes up to 150 mm total length. In order to avoid displacement of the anodes, they are held by fixation clamps. Spacers consisting of PTFE are separating the segments to avoid electrical contact between the anodes.

To set the distances between cathode and grid, and grid to anodes, respectively, various cylindrical spacers with different lengths are available. They can be stacked by lining up them on threaded rods. These spacers as well as the guide rails are made of Macor[i].

4.3.2 Frisch grid

The real challenge in building the new detector was the fabrication of the Frisch grid. The grid was planned to be built of gold coated tungsten wires attached to a frame of stainless steel. The pitch between the wires had to be as small as possible (cf. section 3.3.3). Since the wires are exposed to the force of gravity and in particular electrostatic forces, a minimum of wire tensioning is necessary. Loose or sagging wires would considerably harm the geometrical conditions and therefore the detector's performance.

The main challenge was to achieve enough and constant tension to all wires. Of course, the wires are very fragile due to their small diameter of only 20 μm. The maximum tension for our type of tungsten wire was experimentally determined to be ≈ 0.2 N. The force of tension from the wires working on the framework of the grid is scaling with the number of wires to be mounted. Having the intention to place them with a pitch of 0.5 mm, a force equivalent to several kg is acting on the frame. Although being made of 3 mm strong steel with 5 mm frame thickness, some deformation will take place. Simulations with Elmer[j] predicted a maximal deflection of 2-3 μm of the planned frame. Unfortunately, tungsten tends to be brittle and does not allow elastic deformation to an extent like steel. For minimal deformation of the frame, this means either loose or broken wires. Therefore, simply attaching wire by wire is not an option as it would continuously warp the frame and subsequently loosen earlier mounted wires.

---

[i]machinable glass-ceramic with excellent insulation characteristic and very little outgasing

[j]open source software for calculations of multi-physics problems by the finite element method (FEM)
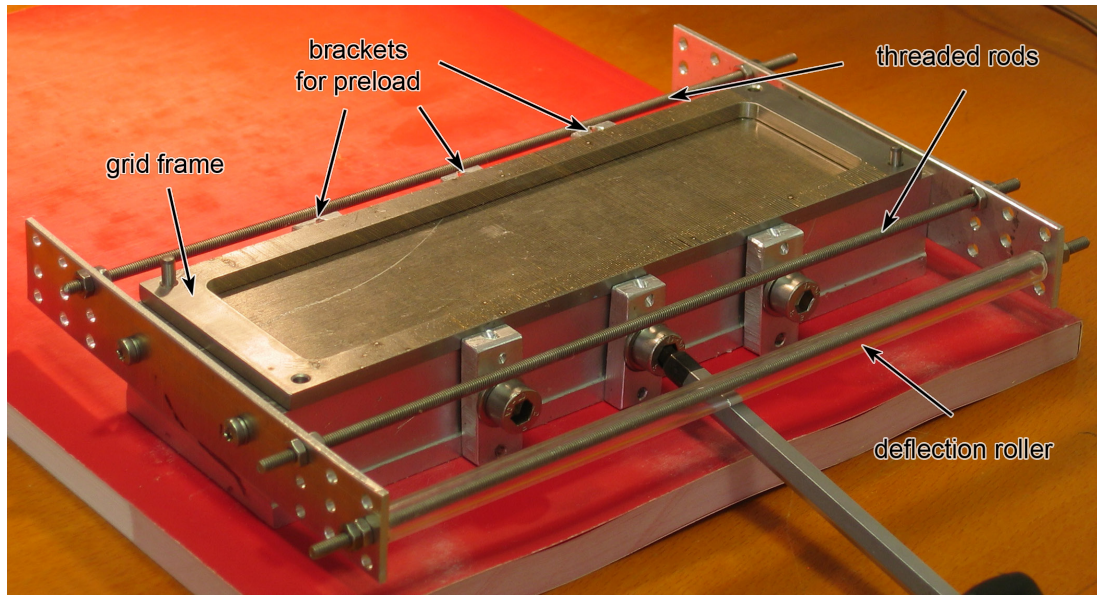
Figure 4.7: Mounting support for the Frisch grid. The picture shows the grid with all attached gold coated tungsten wires, before first relieve of preload.

To overcome this problem, a mounting support (figure 4.7) was built to preload the structure with a weight of 1.5 kg on each side of the frame, prior to bonding the wires. Additionally, threaded rods (with 0.5 mm pitch) on each side of the mounting support provide a guide for the wire. This ensure equal distances between the wires on the frame. A constant pretension of the wires was realized by directing the wire with guide pulleys and tightening it with a defined weight of 10 g (5 g are effectively acting due to a deflection roller). The sum of the initial tension of the wires and the preload of the frame should guarantee uniform distribution of forces onto the frame and the wires, respectively. The limit of load for every individual wire should not be exceeded in this way.

Our limitation not to use outgasing materials to fix the wires was another difficulty to be solved. Techniques used for the Frisch grid of the compact ionization chamber, like bonding with conductive glue, or soldering with tin solder could not be used due to their outgasing components.
Following the advice from a horologist, a special device was developed to squeeze the wires into prefabricated grooves carved into aluminum attachments. Unfortunately, it turned out that this method can not ensure sufficient tension of the wires.

Finally the fixation of the wires was engineered by point welding. By applying a short pulse of current, the wire is welded on the frame. With a simple piece of copper cable with stripped end, the pulse can be positioned punctiform. To prevent melting of the fragile wire before being bonded onto the frame, the current

must not be applied until contact between wire and frame is ensured. Because of producing a short-circuit, the fuse switch of the power supply is interrupting the current immediately after activation. As one can imagine, the whole procedure (see figure 4.8) is a wearing and time-consuming task.
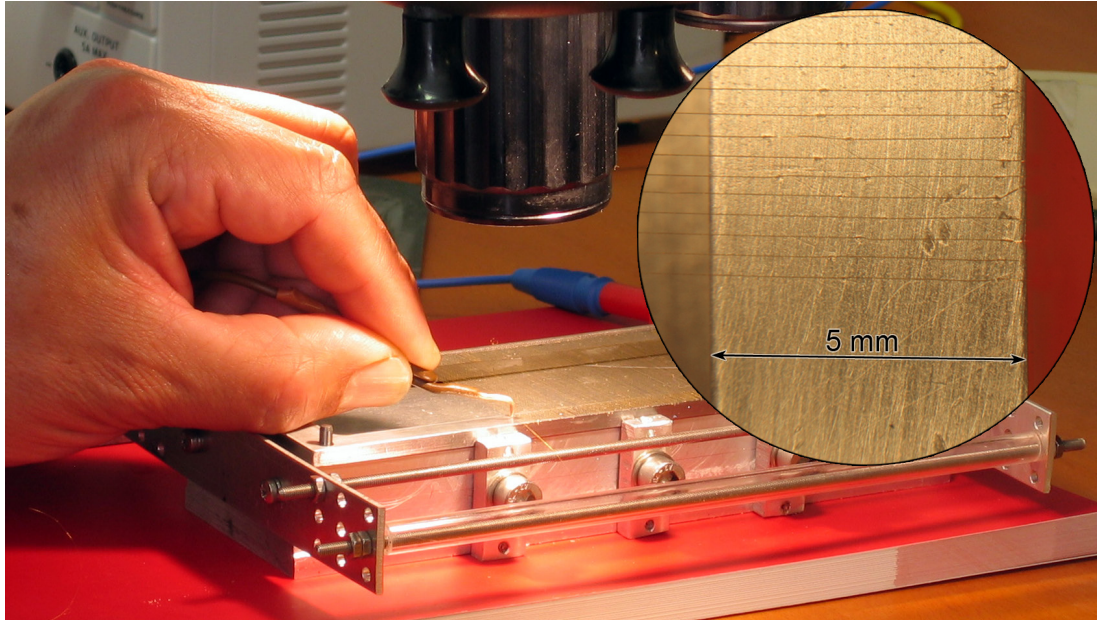
Figure 4.8: Picture of Alfred Priller welding point by point. The small picture shows the view through the microscope used for this procedure.

After attaching all 300 wires, the preload of the mounting support was taken away carefully (figure 4.7) and not one wire was demolished due to the increased strain. This bonding method seems to be a smart solution to fix the wires without using any additional ingredients harming the quality of the counting gas.

4.3.3 Internal signal processing

The reduction of capacitance is the most important means to reduce electronic noise (cf. section 3.3.4). Studying formula 3.7 (page 37) makes one recognize, that only reducing the permittivity (ϵ) and/or enlarging the denominator (r_{wire}/r_{shield}) can make this possible. The distances between anodes and flange (l_{cable}) are already defined due to the lengths and positions of the anodes.
Both values with the potential of improvement could be exploited by designing special low-capacitive conductors. Bearing in mind that any outgasing substances should be avoided, a reduction of permittivity was realized by omitting the dielectric. Dielectrics used for common coaxial cables usually have a relative permittivity greater than 2. In the gas volume at pressures in the range of some ten mbar

the relative permittivity is equivalent to vacuum ($\epsilon_r = 1$).

The ratio between wire radius and shielding radius could be improved by using stainless-steel pipes with square profile (17×17 mm inside) and tensioning a thin copper wire therein. Fixed on the rear flange by dedicated screws holding the bent up ends, these pipes provide a mounting and shielding of the electric conductor, respectively. This conductor is held and tightened by metal sheets mounted at the ends of the profile, where the wire is insulated by aluminum oxide beads in the center of these sheets.
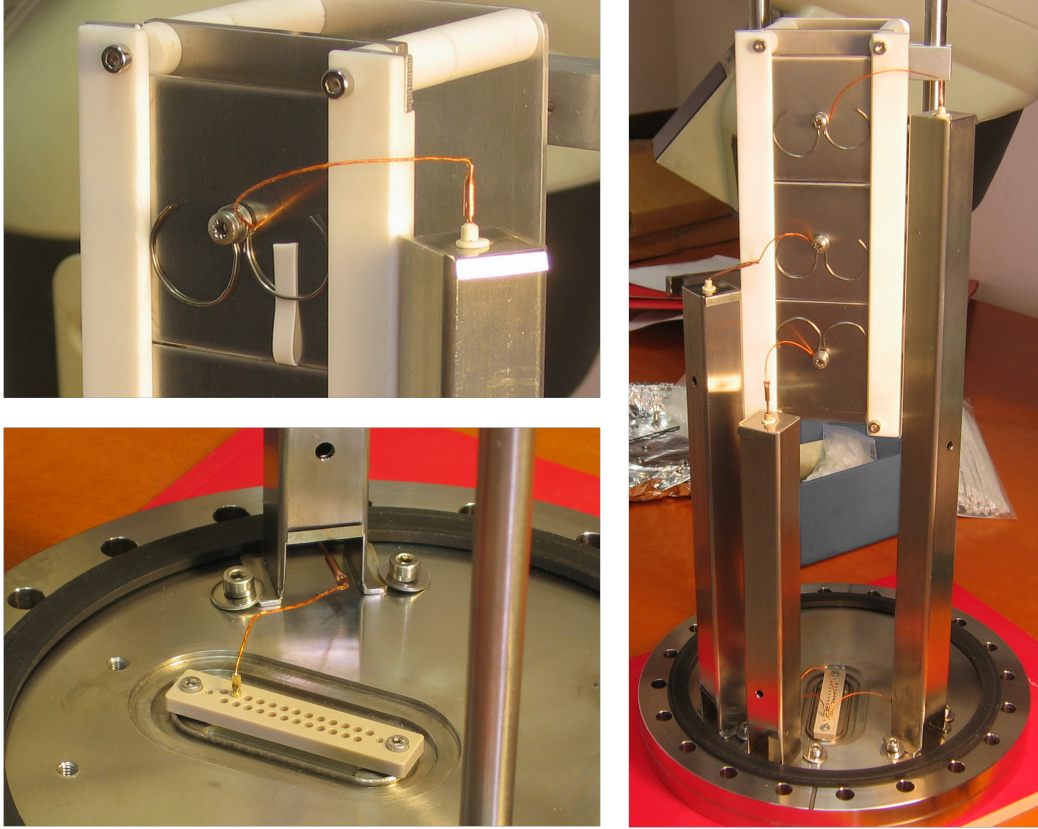
Figure 4.9: Pictures showing the assembly of the low-capacitive pipes and details about their connections.

To assure maximal shielding of the anode's signals, our aim was to bring this pipes as close as possible to the place of signal creation and the feedthroughs, respectively. So three pipes of different length were mounted near the feedthrough which is in the center of the rear flange and makes the signals available outside the detector housing. To complete the signal paths inside the gas volume, the ends of the copper wire were connected to the anodes and the feedthrough, respectively, by

thin wires covered with Kapton[k]. The Frisch grid and the cathode were connected directly with the feedthrough by Kapton-covered wires, too.

For the purpose of advanced anode designs in the future, there is additional space on the rear flange to add further pipes for low-capacitive signal lines.

In figure 4.9 the main arrangement of the low-capacitive pipes and detailed photos concerning their linkage are shown.

4.4 Signal processing

For the purpose of recording and evaluating the measurements, the sensitive charge signals have to be amplified, shaped, gained, converted and stored. The diagram in figure 4.10 shows, how this is done in principle.
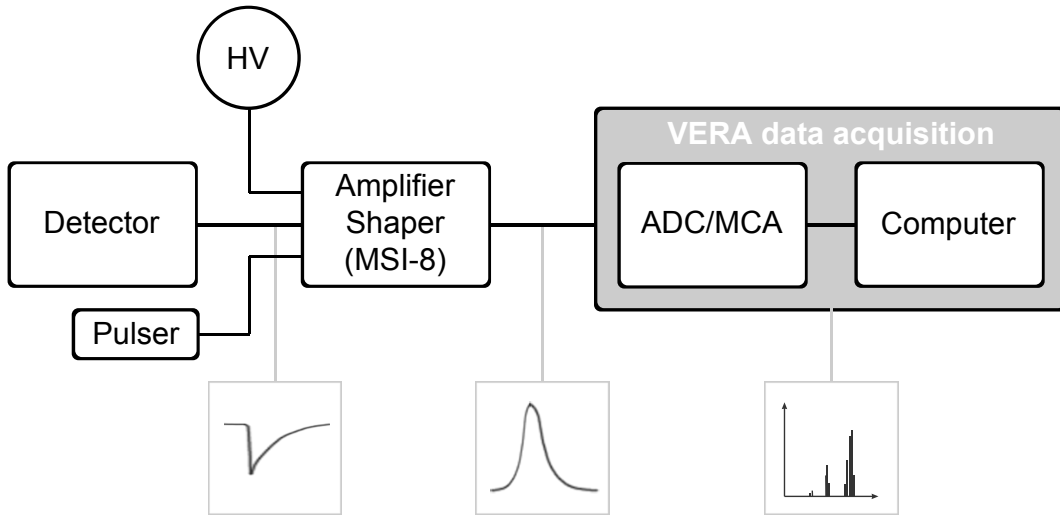
Figure 4.10: Diagram of the signal processing chain (HV = high voltage supply). The signal's typical shape for each section is indicated, too.

The detector signals are provided at the the back flange of the detector housing with a 25-pin D-sub feedthrough (specified for a voltage of 500 V on each pin). An adapter, ending with 15 cm long coaxial cables with LEMO-plugs, makes the signals available for the preamplifier/shaper box (Mesytec MSI-8).

On the bottom side the signals are fed into the amplifier, allowing to process up to eight of them individually. The converting of the charge pulses into voltage pulses, usually done by a separate preamplifier, is implemented via integrated preamplifier modules integrating the charge on a feedback capacitor [Mesb].

The high voltage supply [Ortb] and the pulser signal have to be connected also at

---

[k]polyimide film suitable for a wide range of temperatures and little outgassing

the bottom side of the box. The applicable voltage for the MSI-8 box is specified to be 400 V, and thus, the maximum voltage of the anodes is limited to this value, too.

The power supply for the amplifier is connected on the upper side of the box by a 9-pin D-sub connector, providing all necessary voltages. The outputs for the shaped signals and the knobs for the gain adjustment are also situated on the top of the amplifier's housing.

The shaping time (set to 1 μs) can be changed by setting jumpers inside the box. I leave out discussing further properties of the amplifier/shaper in detail here but refer to the dedicated user manual [Mesa].
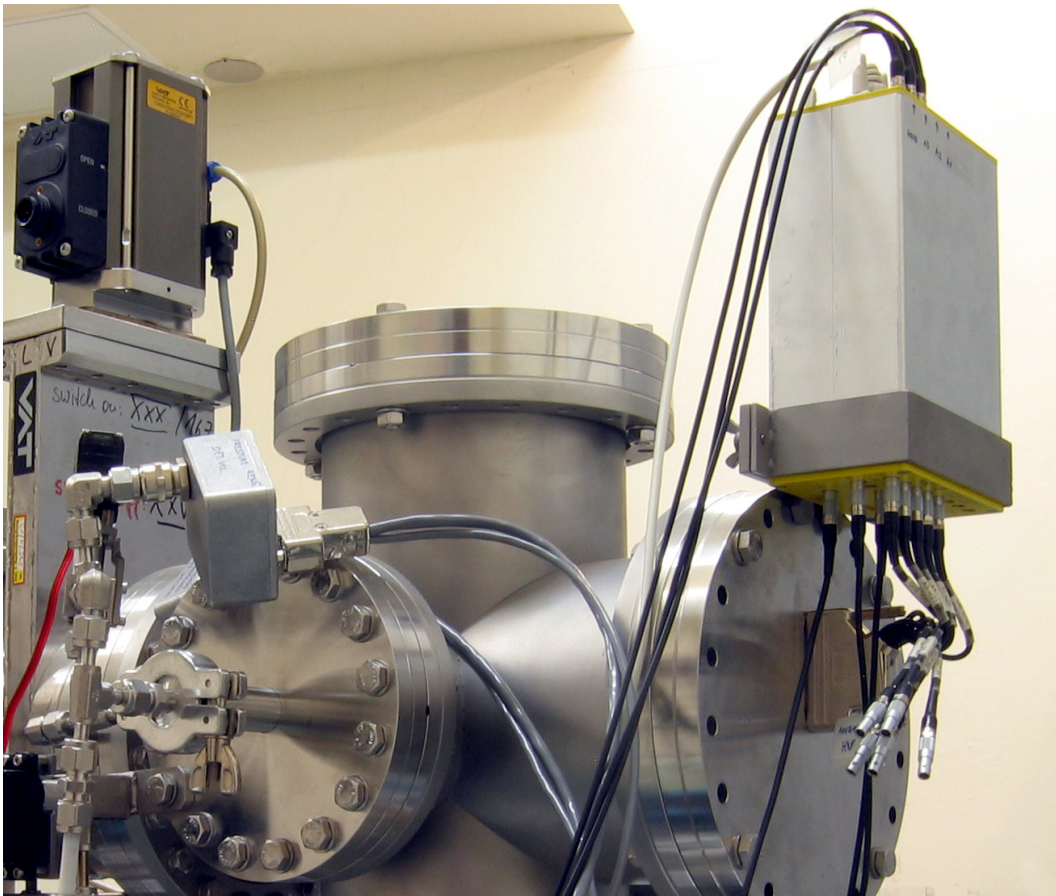
Figure 4.11: Mesytec MSI-8 amplifier/shaper box mounted on the rear flange.

The picture in figure 4.11 shows the installation of the amplifier/shaper box at the very end of the 20° beamline on the topside of the rear flange. Held by a clamp fixed with winged screws, the device can easily be dismantled for maintenance work.

Finally, the detector signals are available from the MSI-8 as voltage pulses in the

range of 0 to 10 V. During the following digitalization process, done by the VERA data acquisition, the analog signals are converted into 12 bit values (corresponding to 4096 channels) by an analog-digital-converter (ADC). The values from each anode are stored into a dedicated file structure, were several predefined procedures allow to evaluate the data for detailed analysis (see section 5.1.2).

5 Measurements & Results

5.1 Characterization tests

The first measurements to characterize the new detector were carried out with a detector geometry also being suited for measurements with large entrance windows. The parameters for this configuration of the ionization chamber together with the belonging window holder (h = 30 mm) are listed in table 5.1.

parameter	label	value
total anodes length	l	150.0 mm
anode partitions	$a1/a2/a3$	50.0/50.0/50.0 mm
anode width	b	40.0 mm
anode-grid clearance	p	7.0 mm
cathode-grid clearance	q	49.0 mm
grid wire diameter	$2r$	20 μm
grid wire spacing	d	0.5 mm

Table 5.1: Geometrical configuration parameters of the new detector for the first series of measurements ("MAIC.1").

As a consequence of these values, the grid inefficiency of this setup is 2.4% (cf. formula 3.2).
With a fixed ratio of field strengths (s), the voltage of the grid is given by the following formula[a]:

$$U_g = \frac{qU_a - spU_c}{sp + q} \tag{5.1}$$

The upper field is defined as

$$E_p = \frac{U_a - U_g}{p} \tag{5.2}$$

and the lower field as

$$E_q = \frac{U_g - U_c}{q} \tag{5.3}$$

---

[a]for variable definitions refer to table 3.1 (page 25) and/or figure 3.5 (page 33)

5.1.1 Electronics inspection

In order to set gain and shaping time correctly, the signal processing chain was checked by test pulses coming from a pulse generator [Orta]. The signals comparable with the detector outputs were connected to the test input of the Mesytec amplifier. Typical pulses and their alteration due to the shaper electronics have been analyzed with an oscilloscope (see table 5.2).

	rise time [μs]	fall time [μs]	amplitude [V]
pulser	0.028 $\pm$0.002	450 $\pm$25	-0.087 $\pm$0.001[a]
after MSI-8	0.970 $\pm$0.050	2.20 $\pm$0.05	8.9 $\pm$0.1[b]

Table 5.2: Comparison of pulse shapes (shaping time = $1\mu s$).

To make the signals of the anodes comparable to each other, and to exploit the range of the VERA data acquisition system optimally, the gain for each individual signal line has to be adjusted at the MSI-8 amplifier. Since not all ions lose the same amount of energy under the individual partitions, it is desirable to get output signals of equal height for detecting the same number of electrons.
The coarse adjustment of the gain can be done by using a pulser signal selecting a suitable pulse height. By using the signal from e.g. anode 1, a fine adjustment of the gain was done for each signal line individually. By considering all parts of the electronic chain this method is preferable. The gain was typically adjusted to achieve a signal height of 2 to 5 V at the output of the MSI-8 box.
Adjusting the gain only with the pulser signals would not consider the signal lines inside the detector housing and the linkage to the MSI-8 box, respectively. By repeating this procedure with one of the other anode's signals, the linearity of the signal's amplification could be verified.
Due to the different signal path lengths inside the detector housing ($\Delta l \approx 5$ cm), there is a small difference in the capacitance of the signal lines ($\Delta C_{cable} \approx 1$ pF). However, the gain of the charge sensitive preamplifiers should not be sensitive to changes in the detector's capacitance. This could be verified by comparing the signal heights of test measurements with and without an additional capacitance (about 2 pF) in the signal line in front of the preamplifier.
The proper functionality of the MSI-8 amplifier/shaper electronics was also verified by substituting the whole Mesytec electronics with Ortec 142 preamplifiers and separated Ortec 571 amplifiers. Several measurements with beryllium/boron (various shaping times, gains, count rates and gate lengths were tested) could not yield results for the total energy resolution below 1.08% ($\approx$ 77 keV) at conditions

---

[a]depending on the chosen pulse height at Ortec 419, this value was measured at pulse height position 5 (middle of the range) and attenuation factor 5
[b]depending on the gain factor, adjustable on the top side of MSI-8

similar to the tests discussed in the following sections. With the Mesytec electronics a total energy resolution for light ions of $(0.852\pm0.003)\%$ ($\approx$ 61 keV) could be achieved (see section 5.2.3).

5.1.2 Energy resolution with light ions

For the first assessment of the detector's resolution, a beam of ^{10}B/^{10}Be, mainly comprising boron, was measured. Especially light ions allow to investigate the electronic's contribution to the performance of the ionization chamber.

The pressure of isobutane was set to 50 mbar to stop all projectiles within the first 100 mm (first two anodes). A 50 nm thick silicon nitride window (window size = 5x5 mm) was mounted. An attenuated ion beam coming from a real ^{10}Be sample was used for this measurements. The ions with an initial energy of 7.17 MeV entered the detector volume with a rate of about 2000 cps.

Based on SRIM-simulations, an energy loss of 65 keV and an additional broadening of the energy distribution of about 13 keV in the entrance window, leads to a nearly mono-energetic ion beam. The combined width of the energy distribution behind the window is below 0.2% ($\sqrt{\delta E_{beam}^2 + E_{window}^2} \approx$ 14 keV).

A voltage of 250 V was applied to the anodes, 175 V to the grid, respectively, resulting in a ratio of the corresponding fields of 3.0 ($E_p/E_q = 107/35.7$). The cathode was kept on ground potential ($U_c = 0$ V), what is the case for all measurements discussed in this work.

In figure 5.1 the spectra (4096 total channels for each anode) recorded by the VERA data acquisition system are plotted. Apart from some noise below channel 50 and the pulser signal around channel 1825 on anode 3, the absence of further events confirms that the projectiles are stopped within the first two anodes. The pulser signal for anode 1 is visible around channel 1898, too. Due to the overlapping with detected boron events, the pulser signal for anode 2 is not apparent in this representation. The different positions of the pulser peaks is a hint, that the fine tuning of the gain with their signal would not lead to valid results concerning the comparability of the spectra (cf. section 5.1.1).

To calculate the detector's total energy resolution, the sum of the spectra has to be evaluated. The resolution of the single spectra would not be a meaningful value, because it is impaired by straggling effects, which cancel out for full energy determination (cf. section 3.3.5).

The spectrum resulting from this summation is shown in figure 5.2. The position of the main peak (around channel 3988) corresponds to the total loss of energy by boron ions in the active detector volume.

The resolution of the main peak of a similar measurement (run0037, same conditions as shown in figures 5.1 and 5.2, but without pulser) calculates to $(0.917\pm0.003)\%$ (FWHM [ch]: 36.65 ± 0.12, peakcenter [ch]: 3995.69 ± 0.05) for summation of all anodes. The indicated uncertainties are based on the fit method
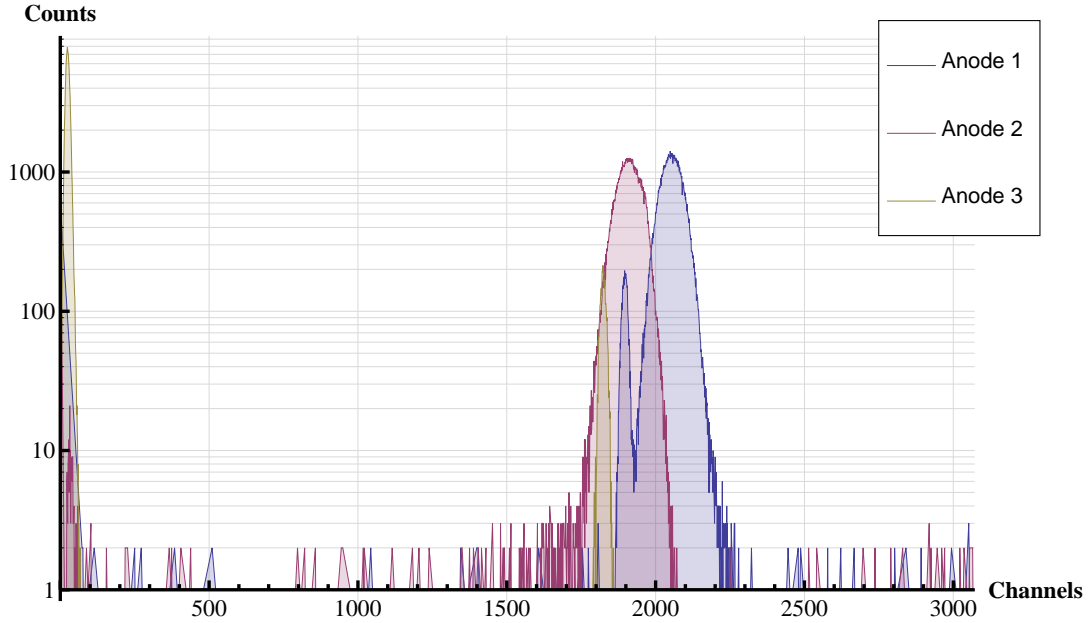
Figure 5.1: Single spectra of ^{10}B with 7.2 MeV initial energy in 50 mbar isobutane (run 0019 from "MAIC_test_Be2", about 134000 total counts). Pulser peaks near channel 2000 are visible, too.

explained in section 7.1 (page 79). Calling to mind that the mean energy of the ion beam after passing the foil is 7.11 MeV, this corresponds to an absolute energy resolution of 65.2±0.2 keV. This value is unnecessarily deteriorated by the electronic noise coming from the third anode. Due to the fact that all particles are stopped within the first two anodes, the summation of the last anode is dispensable. By fitting a Gauss function to the sum peak of the first two anodes, the total resolution for boron ions calculates to (0.856±0.003)% what corresponds to an absolute resolution of 60.8±0.2 keV.

Measurements under comparable conditions with the compact ionization camber could not reach that high performance (about 1% total energy resolution with beryllium/boron).

The difference in the resolution calculated with and without the third anode allows to assess the contribution of uncertainty due to the electronic noise of a single anode's electronic chain. Subtracting these values quadratically from each other leads to an absolute contribution of 24 keV. This experimentally determined value almost fits to the estimated one (22 keV) during the planning phase of the detector (cf. section 3.3.4, page 37 ff). The slight difference can be explained by additional cables and electronics (connection to the VERA data acquisition system), which were not considered in these prior estimations.
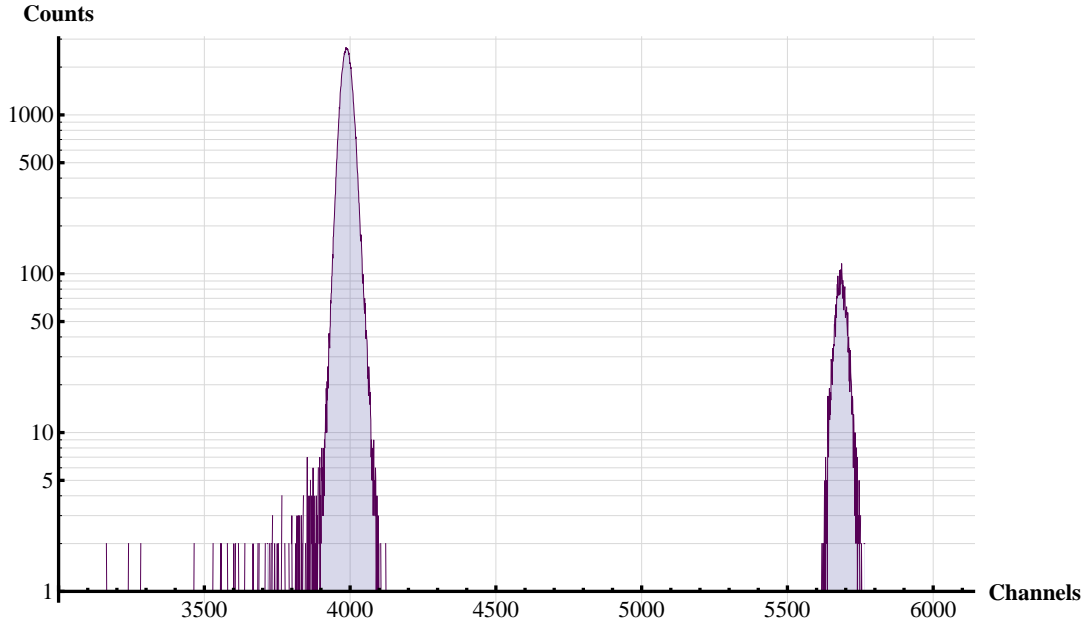
Figure 5.2: Sum spectrum of ^{10}B with 7.2 MeV initial energy in 50 mbar isobutane (anode 1 + anode 2 + anode 3, run0019). The main peak around channel 3988 represents the total deposit of energy by boron projectiles. The sum of the pulser signals is located around channel 5684.

5.1.3 Measurements with ions of intermediate mass

The evaluation of the energy resolution was repeated in a similar way with ions of medium mass. In contrast to light weighted ions, the gas and the geometry are now the dominant influences determining the detector's performance.

Using an unchanged detector geometry and the same silicon nitride entrance window (50 nm thickness), ^{36}Cl and mainly ^{36}S ions with an initial energy of 24.07 MeV were measured (see figure 5.3). SRIM-simulations allow to estimate an energy loss of about 287 keV for sulfur ions when passing the entrance window. The window's contribution to the widening of the energy is predicted to be about 42 keV for sulfur. Due to the higher atomic number, theses values are a little bit higher for chlorine ($\Delta E_{window} = 300$ keV, $\delta E_{window} = 45$ keV).

For the purpose of rejecting tilted particles and tuning of the ion beam, respectively, a 9 mm aperture was mounted between the last two anodes.

The voltages of the anodes and the grid were kept at 250 and 175 V, respectively, resulting in unchanged fields ($E_p = 107$ V/cm, $E_q = 35.7$ V/cm).

The gas pressure was set to 30 mbar, what is high enough to fully stop the sulfur ions within the active detector volume (cf. figure 2.3, page 22).

In figure 5.4 the sum-spectrum of a typical ^{36}Cl/^{36}S measurement is shown. In contrast to the prior measurements without an aperture, now there is another
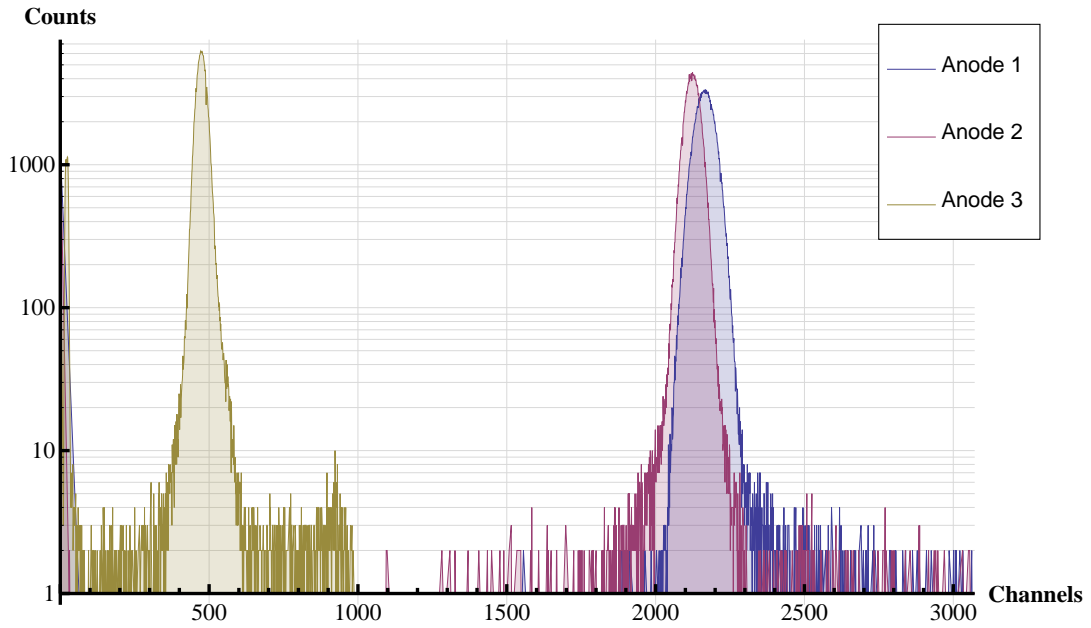
Figure 5.3: Single spectra of ^{36}S with 24.0 MeV initial energy in 30 mbar isobutane (run 0237 from "MAIC_test2", about 250000 total counts).
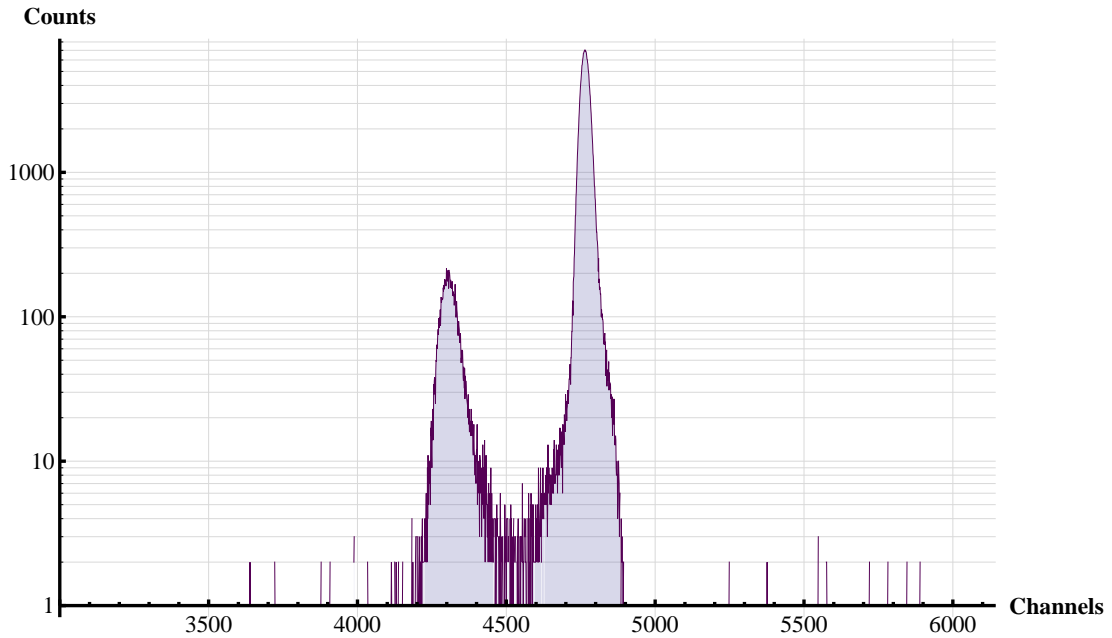
Figure 5.4: Sum spectrum of ^{36}S with 24.0 MeV initial energy in 30 mbar isobutane. The main peak is situated around channel 4765, whereas the left peak contains particles not passing the aperture.

peak, which is not caused by the pulser. The main peak (around channel 4765) is the sum of particle's energy contributing to all anodes. The smaller peak (around channel 4307) contains all particles having a trajectory tilted too much and therefore not being able to pass the aperture. Hence, only the energy deposited under the first two anodes contributes to the signal. The residual energy is lost by striking the aperture.

The total energy resolution for the full energy peak depicted in figure 5.4 calculates to $(0.708\pm0.004)\%$ (FWHM [ch]: 33.73 ± 0.17, peakcenter [ch]: 4764.62 ± 0.07), what corresponds to an absolute energy resolution of 168.4 ± 0.8 keV for particles with a kinetic energy of 23.78 MeV after passing the entrance window.

The use of an aperture also slightly improves the total resolution of the detector. Without aperture tilted projectiles would also reach the third anode. By evaluating only events passing through the aperture, the geometric beam diameter of effectively evaluated events is limited to its opening. Hence, the geometrical contribution to the total uncertainty is restricted.

In order to evaluate the separation capabilities of the new detector, different samples (Cl-blanks, Cl-standards) were measured. Once again the aperture plays an important role. By choosing the right aperture diameter, the high energy tails in the spectra of the first two anodes can be reduced. For this kind of isobar identification and suppression the sum spectrum of the first two anodes is plotted against the spectrum of anode 3 (see figure 5.5).

This two-dimensional representation of spectra is called density plot and allows to distinguish isobars in an easy way. The suppression of sulfur against chlorine can be determined by comparing the number of events located in the regions of interest (blue markings) and the total number of sulfur events. The calculation of this ratio with known materials allows to correct for sulfur-induced background.

The ability to separate the two isobars is a consequence of the energy resolution of the detector and as well strongly linked with the use of an aperture. Particles not flying straight ahead have to cover longer distances in the area of the first two anodes resulting in so called *high energy tails* in the associated spectra. By evaluating only coincident events on all three anodes, particles with tilted trajectories are excluded.

Using a very small aperture would reduce transmission through its opening and therefore poorer statistics would hamper the measurements. The use of a 9 mm aperture led to a suppression factor of about 9000 for sulfur at 50% chlorine detector efficiency.

To find a compromise between good transmission and sufficient cutting of the high energy tails, detailed SRIM-simulations resulted in an aperture diameter of 6 mm for the geometry actually used ("MAIC.1"). The optimum diameter of the aperture depends also on the gas pressure inside the detector volume. Finding the best ratio of energy deposit in front and after the aperture can increase the suppression factor additionally (see also [Mar12, page 22 ff.]).
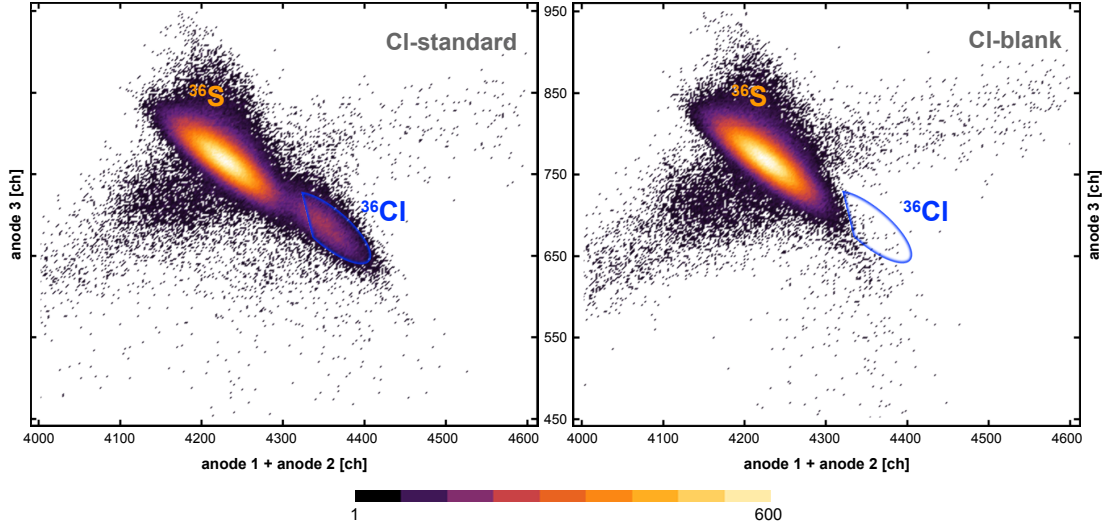
Figure 5.5: 2D-density plot for isobar identification and separation. The blue eye guides, marking the same positions, indicate the region of interest for chlorine. The figure shows a comparison of a Cl-standard material ($^{36}Cl/^{35}Cl = 10^{-11}$) and a Cl-blank at similar measurement conditions ($\approx$ 315000 events on each plot, 24.07 MeV initial energy, 50 nm silicon nitride window, 30 mbar isobutane, U_a = 300 V, s = 3, using a 9 mm aperture between anode 2 and 3).

Finally, a sulfur suppression factor of about 11000 at 50% chlorine detector efficiency could be achieved by measuring with a 6 mm apertur in 30 mbar isobutane.

5.1.4 Detection of heavy ions

For AMS with heavy ions, an entrance window of Mylar[®c] (1.4 μm thick, equal to 0.195 mg/cm^2) with a circular opening of 25 mm inner diameter was glued onto the window holder using a two-component adhesive.

Based on SRIM-simulations, the gas pressure was set to 20 mbar to stop ^{236}U ions of 16.6 MeV kinetic energy (11.1 MeV after passing the window) within 100 mm (first two anodes) in isobutane. A voltage of 200 V was applied to the anodes and 140 V to the grid, respectively, resulting in a ratio of the corresponding field strengths of 3.0 ($E_p/E_q = 86/28.6$).

First spectra of heavy ions were recorded at a count rate of about 1800 cps (figure 5.6). Due to the high energy loss ($\Delta E = 5530$ keV[d]) and the high energy straggling ($\delta E_{window} = 1780$ keV[d]) inside the relative thick entrance window, this

---

[c]polyester film with excellent properties concerning its tensile strength, stability, and electrical insulation
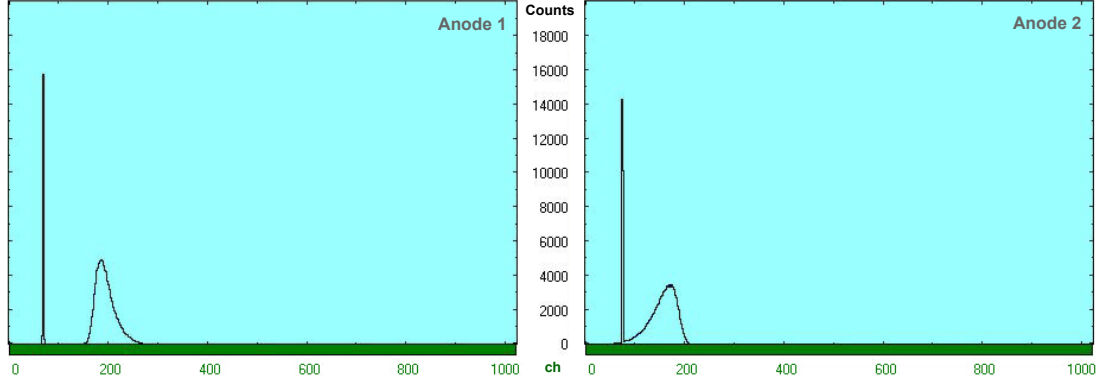
Figure 5.6: First spectra recorded from MAIC with heavy ions: ^{236}U with 16.6 MeV initial energy in 20 mbar isobutane, 1.4 μm Mylar window, the spectra are displayed with 1024 channels, the fine peaks indicate the pulser signals.

measurement is not well suited to derive information on the detectors resolution.

This measurement of heavy ions, which was the first test at all, demonstrated in a frictionless way the principal functionality of the new ionization chamber. Furthermore, the goal of a high transmission into the detector volume could be achieved by a bigger entrance window. In comparison to the Bragg detector, used in the past as last part of the TOF-detection, the detector's opening increased by a factor of about 2.2 (from 15×15 mm to 25 mm diameter).

5.2 Advanced detector examinations

In course of several beam times exclusively intended for further tests on the detector's performance, various dependencies between electrical and geometrical properties concerning the total energy resolution were explored. These measurements were also a detailed check for the reliability of the new gas handling system.
Unless otherwise indicated, all tests were performed with a 50 nm silicon nitride window (5×5 mm) and a circular aperture (6 mm diameter) mounted between anode 2 and anode 3. The typical count rate during the measurements was in the range of 1000 to 2000 cps for all types of ions. Several tests with higher count rates (up to 3×10^4 cps) demonstrated, that there is no significant influence on the detector's resolution at count rates of some thousand counts per second.

---

[d]based on SRIM-simulations

5.2.1 Gas regulation

During the first automated measurement series over a period of several hours it became apparent, that there was a shift of the sum-peak in the spectra. Measuring at pressures (25 and 20 mbar) where not the total energy of the projectiles is deposited in the active detector volume, this behavior indicates a change in the (areal) density of the detector gas. But also for the measurements at 30 mbar (full energy stopping) this change in the gas' density could be observed due to drifts of the peaks in the single spectra. The peak in the spectrum of the first anode was drifting towards higher values, while the peak in the spectrum of the third anode was drifting to lower values, and vice versa.

To verify this, a series of measurements was made with closed metering valves. That means, that apart from some negligible leakage, there is no exchange of gas and thereby the (areal) density in the gas volume is constant.
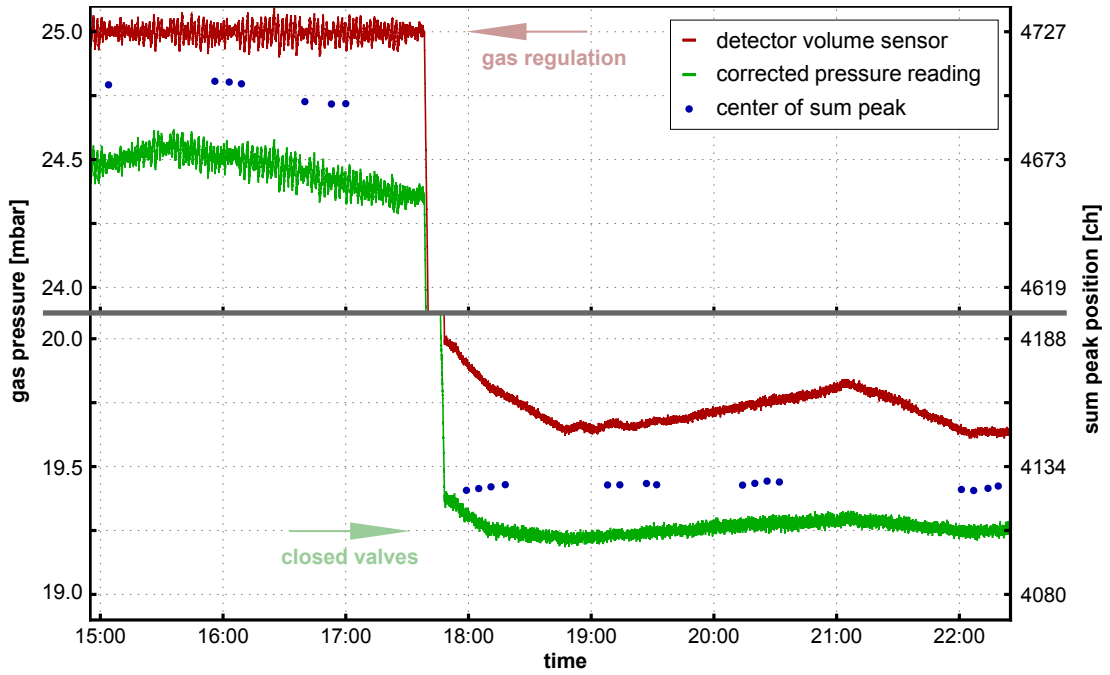
Figure 5.7: Pressure reading compared with the sum peak positions. The course of the pressure for the time domain of the measurements listed in tabular 7.1 (page 81) is shown. After 17:55 the metering valves were closed. The red line shows the pressure measured in the detector volume, the green line is the corrected signal, the uncertainties of the peak positions is less than the size of the blue symbols.

In figure 5.7 measurements with regulating gas handling system and closed metering valves, respectively, are compared. Originally, the regulation of the gas pressure was planned to be done by using the signal of the detector volume sensor for the PID-controller. Now this measurements showed that there is a drift

in density. This regulation error is caused by changes in the sensor's behavior on changing temperatures. Fortunately, this fault can be corrected by using the signal of the sensor measuring the pressure in the volume in front of the entrance window. Although this sensor always should "see" the same pressure (below 10^{-4} mbar, evacuated by a turbo pump), there is a similar drift in the signal, too.

Assuming that this drift depends only on the temperature allows to correct the detector volume's signal for this effect (green graph in figure 5.7). Looking at the correlation between the average course of the corrected pressure reading and the peak positions of the sum peaks makes one recognize, that regulating on this signal would improve the accuracy of the gas density regulation.

This assumption could be verified by measuring with closed metering valves. While the average pressure value from the detector volume sensor, seems to drift up and down ($19.8 - 19.9$ mbar), the variation of the average of the corrected signal is less than 0.05 mbar. The short-term fluctuation of the signals is caused by noise in the sensor electronics.

Thus, a consequence of this observation was a change of the control variable on which the PID-controller of the gas handling system is regulating for.

The energy resolution values derived during this series of measurements with Cl-blanks also demonstrate, that high total energy resolution only can be achieved by full energy stopping. SRIM-simulations showed, that pressures above 28 mbar are necessary to fully stop ^{36}Cl/^{36}S ions with 24.0 MeV initial energy within a penetration depth of 150 mm in isobutane. The decreased resolution at lower pressures is harmed by the contribution of straggling effects and the loss of energy outside (after) the active detector volume, respectively.

5.2.2 Reproducibility & experimental deviation

A series of measurements with unchanged detector parameters and similar count rates lasting over several hours was analyzed to check the reproducibility of the results.

In figure 5.8 the evaluated total resolution for each run (lasting over a few minutes) is shown over a period of about 2.5 hours. One has to consider that several other measurements (with deviating count rates and/or different samples) took place between the runs, used for this analysis. Hence, this series of data points is comparable to real measurement conditions. The indicated error bars, based on the calculation method mentioned in section 7.1, are in good agreement ($\chi_{red}^2 = 0.9$) with the experimental deviation resulting from the plotted values (cf. table 7.2 for detailed data).
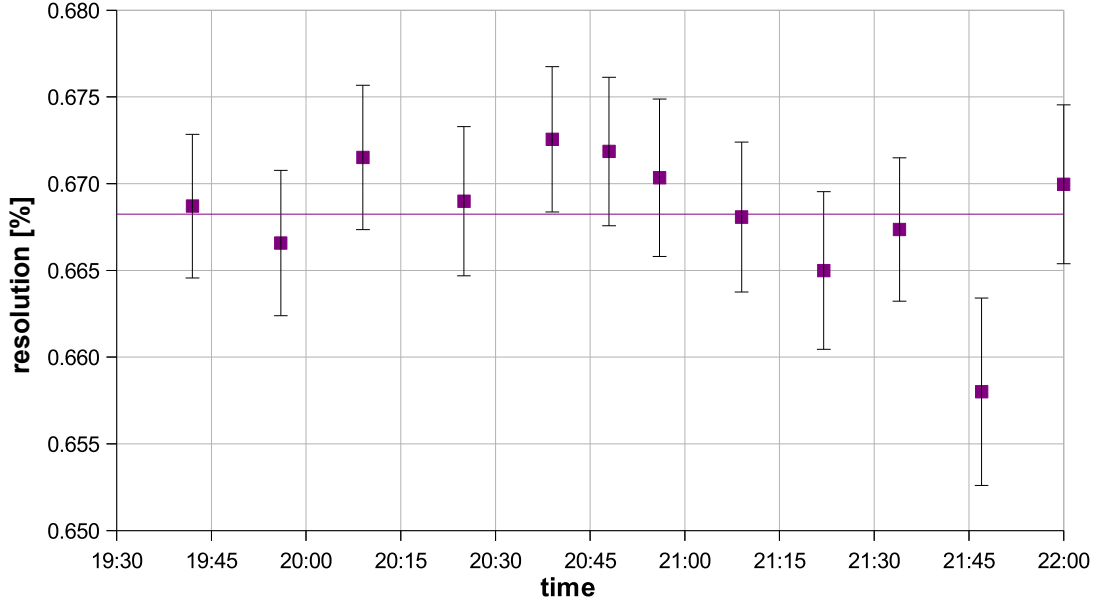
Figure 5.8: The diagram shows the reproducibility of the resolution measurements by comparing the total resolution of Cl-samples ("MAIC_test_Cl3" at 24.0 MeV) measured with constant detector parameters (cf. table 7.2) over a period of about 2.5 hours. The purple line represents the mean value of (0.669±0.004)% for the plotted data points.

5.2.3 Variation of field strengths

In order to find the optimum configuration of the electric fields inside the new ionization chamber, first the influence of the field strengths on the total resolution was examined. Starting with a field ratio similar to our compact ionization chamber, several measurements with different voltages were performed.

Results with beryllium/boron

For the measurements with light ions, a beam mainly comprising ^{10}B particles entered the detector with a mean initial energy of 7.2 MeV. The gas pressure of isobutane was set to 50 mbar in order to fully stop the projectiles within the first two anodes.

By changing the voltages of the anodes and the grid according to formula 5.1, various field strengths were tried out (see table 7.3). The total resolution for each run was evaluated for the sum of the first two anodes and is plotted against the lower field strength (E_q) in figure 5.9.

The chronological variation of the fields was chosen to be the same at the start and the end of the measurement series ($E_q = 35.7$ V/cm). So once again the reproducibility of the results was tested and showed, that no significant drifts occurred. Looking at the diagram (figure 5.9), one can assume an optimum range

Figure 5.9: The total resolution is plotted against different field strengths for 7.2 MeV beryllium/boron ("MAIC_test_Be2", gas pressure $= 50$ mbar, $p = 7$ mm, $q = 49$ mm, $s = 3.0$, cf. table 7.3).

Figure 5.10: The channel number of the peakcenter is plotted against different lower field strengths for 7.2 MeV beryllium/boron ("MAIC_test_Be2", gas pressure $= 50$ mbar, $p = 7$ mm, $q = 49$ mm, $s = 3.0$, cf. table 7.3).

for the lower field strength of around $30-40$ V/cm suitable for the actual geometry ($p = 7.0$ mm, $q = 49.0$ mm).

For decreased lower field strengths the achievable resolution is significantly harmed due to recombination processes in the gas volume. This behavior can be demonstrated more clearly by comparing the detected total energy (channel number of the sum peak) with the applied field strengths (see figure 5.10).
Above a certain value for the field strength (about 35 V/cm), almost all electrons of the ionization process seem to be collected, whereas the sum peak position is shifted towards lower channel numbers for decreased lower field strengths. This shift indicates a loss of electrons and therefore a loss of energy in the detection process.

Results with chlorine/sulfur

The kind of measurements discussed above, was repeated with unchanged geometry for medium weighted ions in order to verify these effects for chlorine/sulfur. An ion beam of mostly ^{36}S particles with an initial energy of 24.0 MeV was stopped in 30 mbar isobutane generating electron signals on all three anodes.
In these series of measurements also a sample of data points with a field ratio of $s = 4$ was produced. The comparison of the results obtained from these runs (figure 5.11) do not show a significant dependency on the tested field ratios.

The overall lower values for the total energy resolution can be explained by a higher amount of available electrons due to about three times higher kinetic energy of the incident particles.
Similar to the behavior with light ions, there is a lower limit for the field strengths (around 20 V/cm for the lower field), below which the recombination probability in the gas increases. This deterioration of the total resolution is once again emphasized by plotting the sum peak positions against the field strengths (figure 5.12).

For high lower field strengths (E_q above about 40 V/cm), the positions of the peaks slightly moves towards lower channel numbers. This behavior is presumably influenced by the drift velocity of the electrons and the ratio of field strengths. For increasing field strength the difference in drift velocity between lower part (place of ionization to grid) and upper part (grid to anode) becomes smaller (cf. figure 3.6 on page 36). Together with the ratio of the fields (see section 5.2.4), this ratio of drift velocities affects the influence of the grid's inefficiency. Hence, an inappropriate ratio of these velocities (small difference) can additionally harm the resolution of the detector.
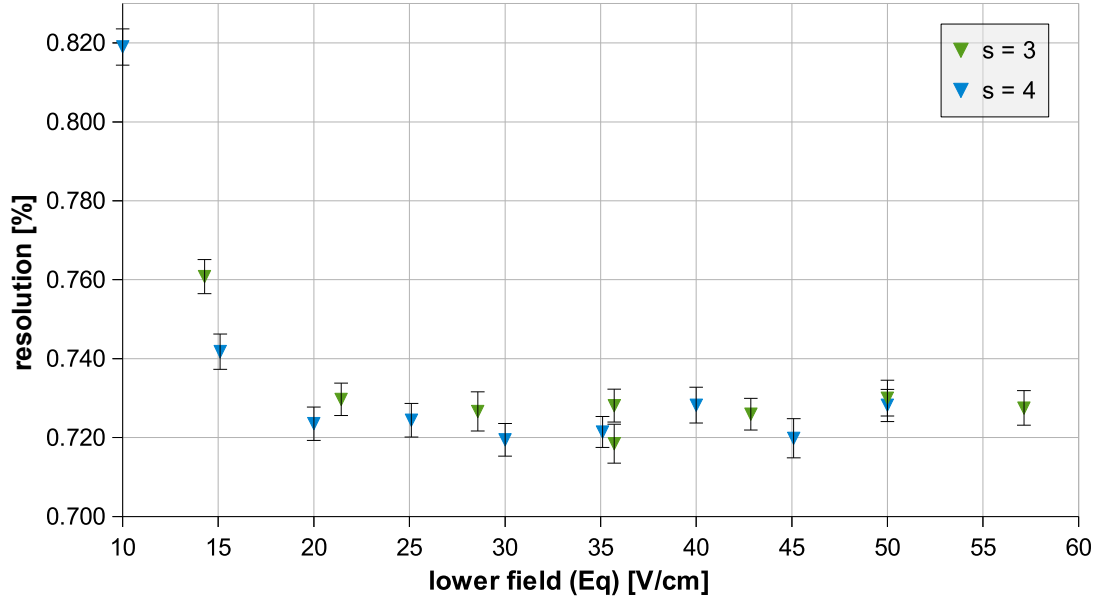
Figure 5.11: The total resolution is plotted against different field strengths for 24.0 MeV chlorine/sulfur ("MAIC_test_Cl3", gas pressure = 30 mbar, $p = 7$ mm, $q = 49$ mm, cf. table 7.4).
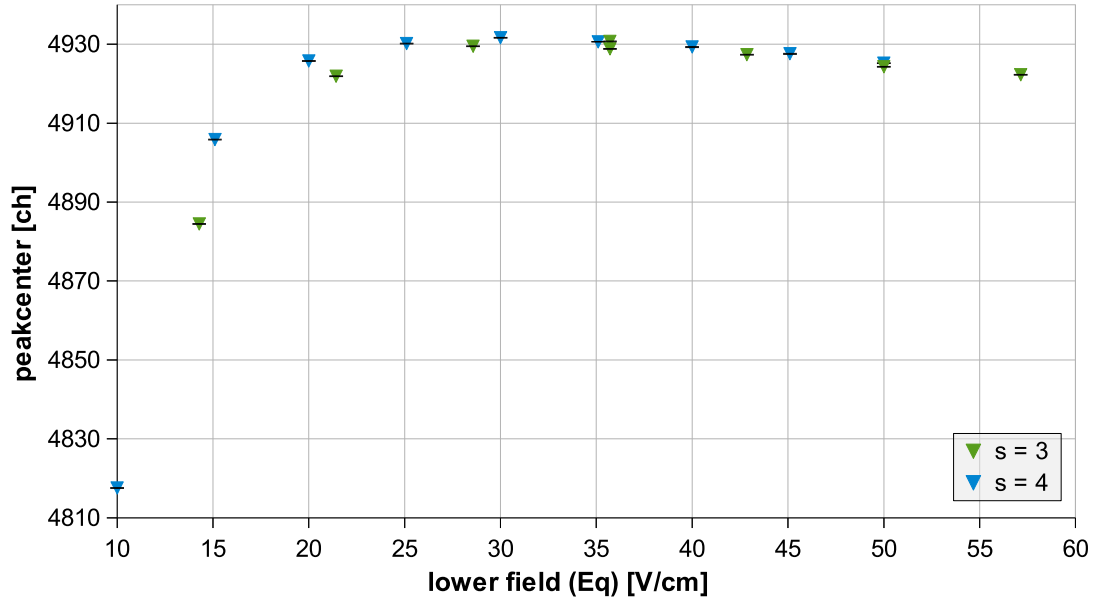
Figure 5.12: The channel number of the peakcenter is plotted against different lower field strengths for 24.0 MeV chlorine/sulfur ("MAIC_test_Cl3", gas pressure = 30 mbar, $p = 7$ mm, $q = 49$ mm, cf. table 7.4).

5.2.4 Variation of the field ratio

To find out the best ratio for the electric fields inside the new detector, another series of measurements with unchanged geometry ($p = 7.0$ mm, $q = 49.0$ mm) was done. In contrast to the compact ionization chamber, the ratio between the voltage of the anodes and the grid's voltage can be modified by applying them individually. The field ratio of the compact ionization chamber is fixed to $s = 3.5$. In turn only one high voltage supply is necessary, which is adapted to the grid by a resistive voltage divider inside the chamber.

Due to the flexible geometry and for the purpose of investigating the influence of this field ratio, two independent voltages have to be applied for MAIC. With formula 5.1 the correct grid voltage can be calculated for any ratio to be tested. In some cases the achievable ratio is limited by the maximum applicable voltage allowed at the MSI-8 box. The evaluation of the experimental data however showed that this boundary condition does not affect measurements at optimum values.

Results with beryllium/boron

Using the same beam of ions as described in section 5.2.3 (^{10}B at 7.2 MeV), several runs with constant lower field strengths were performed. In accordance with the optimum range determined before, the value for the lower field strength was kept constant at $E_q = 35.9$ V/cm, while the upper field strength (E_p) was varied to achieve different ratios of fields. Additionally, a series of measurements with a different lower field strength ($E_q = 21.4$ V/cm) was made for the purpose of comparison. The results of these runs are shown in figure 5.13.

In the range where the optimum ratio was presumed some measurements were repeated to increase the significance of the data. Although the measurement series with the smaller lower field strength was done with a sub-optimal value ($E_q = 21.4$ V/cm, cf. figure 5.9), the achieved resolution is still good.

But looking at the diagram (figure 5.14), where the positions of the peakcenters are plotted against the tested ratio of fields, one can recognize, that less electrons and therefore less energy is collected using the smaller field strength in the lower part of the ionization chamber. In comparison to increasing the field strength (cf. section 5.2.3), selecting higher ratios for the fields does not really change the detector's behavior. However, decreasing the ratio of fields below a certain value (about $s = 2$) dramatically deteriorates the total energy resolution. This effect is caused by the loss of electrons on the grid due to the reduced permeability in case of lower field ratios. The amount of detected electrons for run 0028 (cf. table 7.5) at a field ratio of $s = 1$ is reduced by about 16% in comparison with runs at ratios of 3 or more. This result is in good agreement with the theoretical value for the actual grid geometry ($2\pi r/d = \rho \approx 0.13$) for $s = 1$ [BCH49, figure 4 (page 198)].
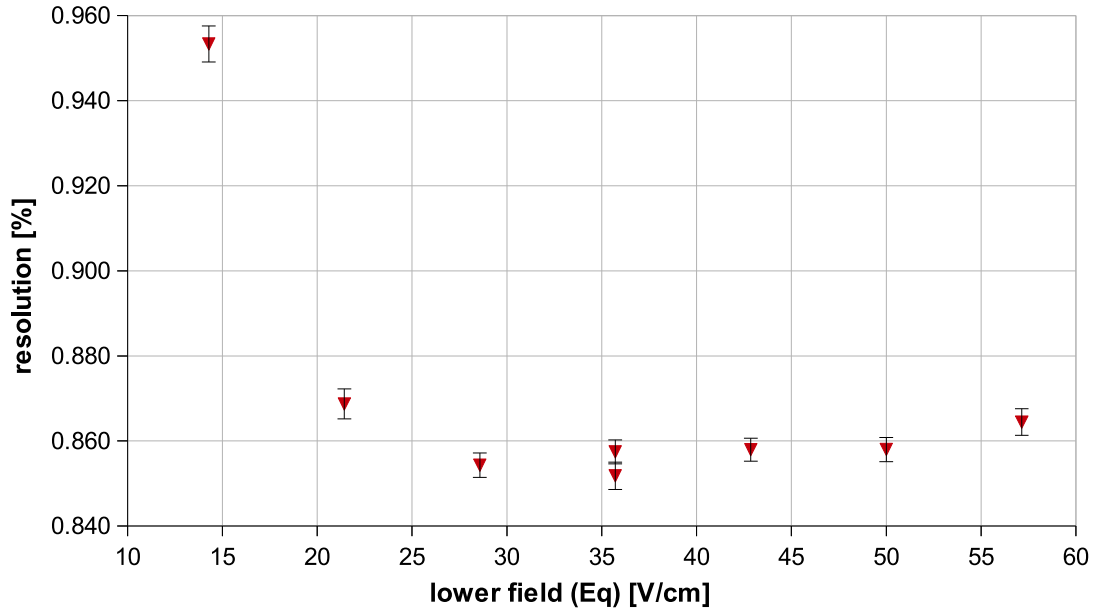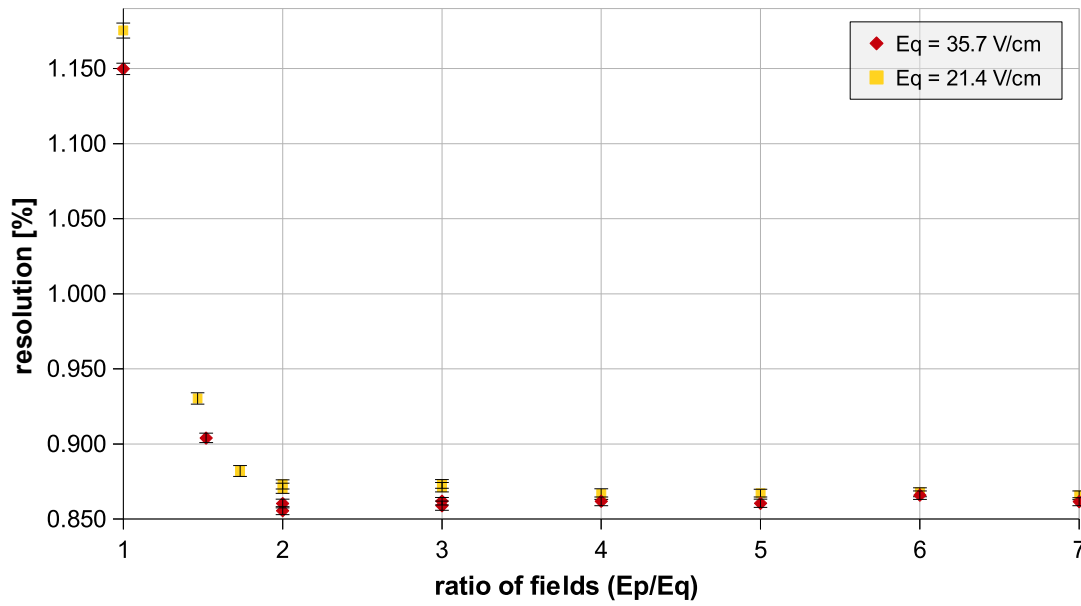
Figure 5.13: The total energy resolution is plotted against different field ratios for 7.2 MeV beryllium/boron ("MAIC_test_Be2", gas pressure = 50 mbar, $p = 7$ mm, $q = 49$ mm, cf. table 7.5).
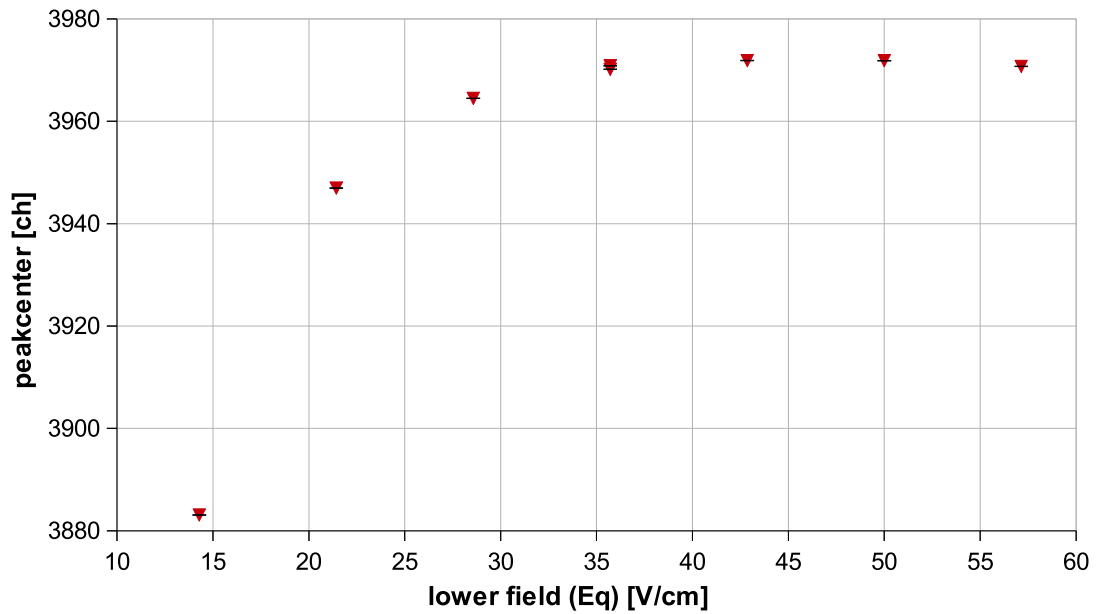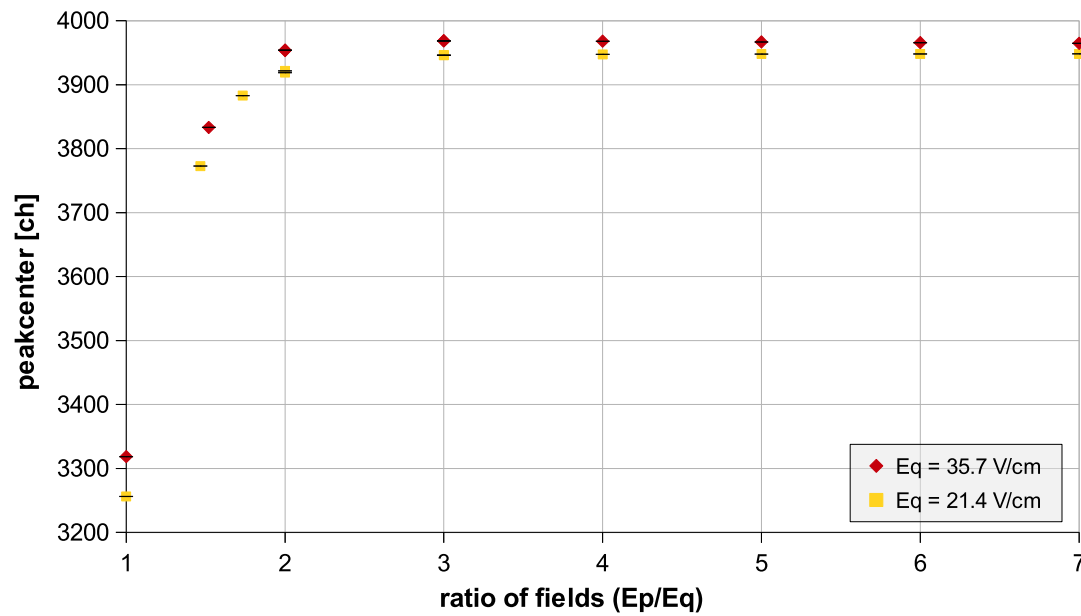

Figure 5.14: The channel number of the peakcenter is plotted against different field ratios for 7.2 MeV beryllium/boron ("MAIC_test_Be2", gas pressure = 50 mbar, $p = 7$ mm, $q = 49$ mm, cf. table 7.5).

Results with chlorine/sulfur

The measurements concerning the variation of the ratio of the electrical field strengths were repeated for chlorine/sulfur samples in a similar way as described above for light ions.

Once again an ion beam of mainly ^{36}S projectiles with 24.0 MeV initial energy was used to perform the runs. With a gas pressure of 30 mbar and unchanged geometry, similar dependencies for the total resolution were observed. Using the same lower field strength ($E_q = 35.9$ V/cm), a field ratio higher than $s = 2.5$ seems to be sufficient for complete electron detection. The plotted results for this series of measurements is included in figure 5.16 (data set "MAIC.1").

5.2.5 Variation of detector geometry

Based on the knowledge from the results of the different measurements discussed above, the influence of the clearance between electrodes and grid was investigated with chlorine/sulfur samples.

For this purpose the detector was modified several times to test distances, where an increase of performance was expected. This procedure of modification (venting the detector housing, extracting the detector via the rear flange, reassembling of the cathode/grid/anodes, evacuating the detector housing, gas regulation) takes about two hours each time, until new measurements can take place.

In order to allow a reasonable comparison of the received data, the measurements were performed at similar fields and ratios, respectively, if practical. The values selected for the new distances (p and q) were chosen according to the estimations done in the planning phase (cf. table 3.3).

An ion beam of mainly ^{36}S projectiles with an initial energy of 24.0 MeV was used for the various measurements. The entrance window (50 nm silicon nitride) and the 6 mm aperture between anode 2 and anode 3 were unchanged, too.

In figure 5.15 the results from measurements with various field strengths are compared for optimum field ratios. The resolution's dependency on the ratio of the fields was also examined for the different geometries. The results from measurements with a lower field strength of 36 V/cm are depicted in figure 5.16.

The reduction of the cathode to grid distance (q) by 10 mm (from 49 mm to 39 mm) entails a shortening of the lower drift path by 5 mm. Resulting in shorter drift times and a decrease in electron diffusion along their path to the anode, this modification allowed to record spectra with a total energy resolution of $(0.660\pm0.005)\%$. For chlorine/sulfur ions with 23.7 MeV kinetic energy after passing the entrance window, this corresponds to an absolute energy resolution of (157 ± 1) keV.

Nevertheless, during several measurements it turned out, that this detector configuration is very sensitive for geometrical deviations. In comparison to the "higher"
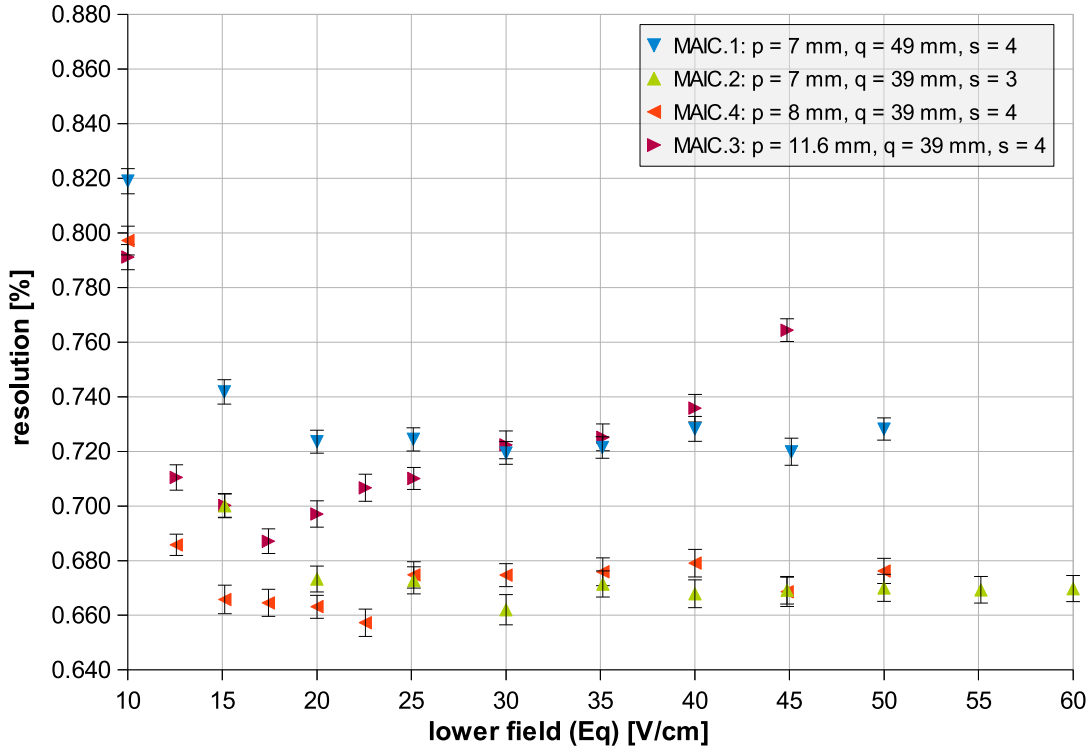
Figure 5.15: The total energy resolution is plotted against lower field strength for different geometries with 24.0 MeV chlorine/sulfur, cf. tables 7.6 (MAIC.1), 7.7 (MAIC.2), 7.8 (MAIC.4) and 7.9 (MAIC.3) for detailed data ("MAIC_test_Cl3", gas pressure = 30 mbar).

geometry (cf. MAIC.1) the total resolution can significantly be harmed by an inappropriately wide beam inside the detector. By an adequate tuning of the ion-optical components in front of the detector, a "slim" beam of ions can be assured. Tests with less cathode to grid clearance were postponed, because it would be very hard to tune for an even more accurate beam without further beam diagnostic elements near the detector.

By increasing the grid to anode clearance (p), also the inefficiency's influence on the total resolution of the detector was explored. Changing the upper distance from 7 mm to 8 mm (cf. "MAIC.4"), resulting in a lower value for the inefficiency (from 2.4% to 2.1%), did not lead to noticeable effects. However, the substantial enlargement of the distance between grid and anodes to $p = 11.6$ mm (cf. "MAIC.3") caused an overall decrease of the total detector resolution.

Apart from this, a new behavior concerning higher field strengths and ratios of fields, respectively, was observed. In contrast to the effects already discussed in sections 5.2.3 and 5.2.4, with an inefficiency of $\sigma = 1.4\%$ a higher sensitivity for the optima of field strength and ratio of fields were determined. Looking on the
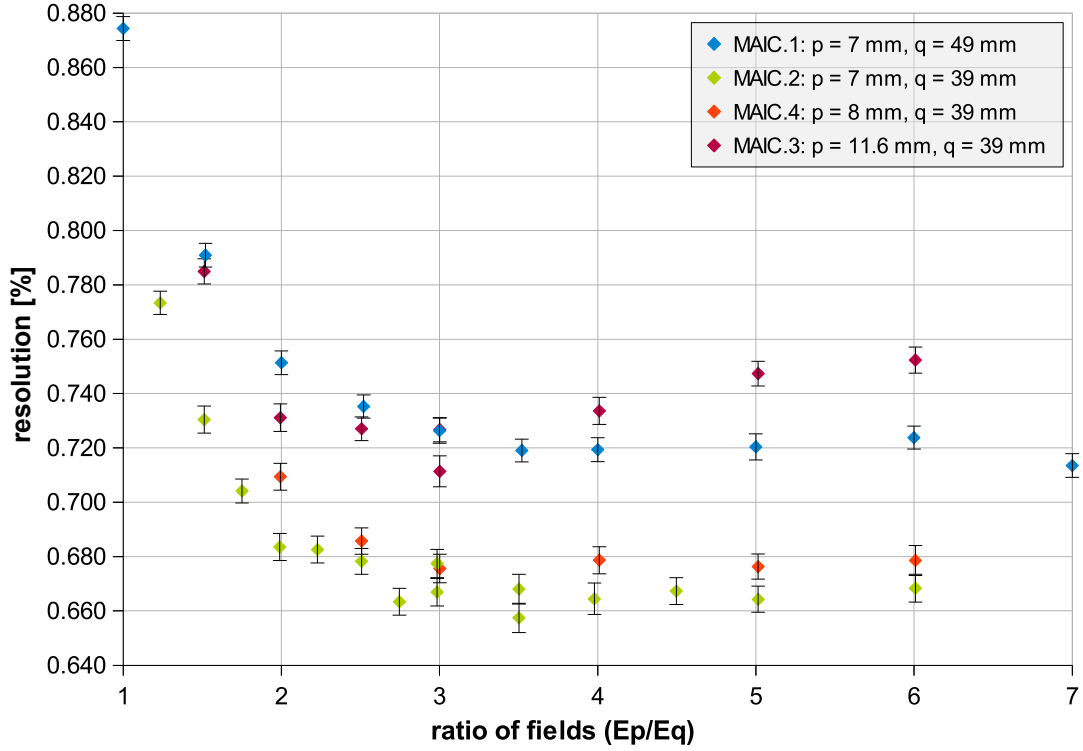
Figure 5.16: The total energy resolution is plotted against field ratio for different geometries with 24.0 MeV chlorine/sulfur, cf. tables 7.10 (MAIC.1), 7.11 (MAIC.2), 7.12 (MAIC.4) and 7.13 (MAIC.3) for detailed data ("MAIC_test_Cl3", gas pressure = 30 mbar, $U_g = 36$ V).

dataset for "MAIC.3" in figures 5.15 and 5.16 makes one recognize, that there is a explicite minimum for the graphs in both plots. This is in contrast to all other plots were no significant rise of the points towards higher x-values is noticeable. Both, the reduced performance of total energy resolution and the higher sensitivity on appropriate field ratios and field strengths, respectively, are probably correlated with the increase of the drift path lengths for the electrons. Hence, some beneficial effects expected from the reduced inefficiency are obviously predominated by adverse consequences of this geometry. Further measurements are desirable to attain more profound understanding on this interrelations.

6 Conclusions & Outlook

The construction of the new multi-anode ionization chamber for VERA led to a high resolution energy detector with versatile abilities. One of the main goals was an enhancement of the detector's energy resolution for the purpose of identification and separation of medium weighted ions like chlorine vs. sulfur.

Starting with the design of the compact ionization chamber, detailed simulations and calculations predicted an increase of absolute energy resolution from 200 keV to about 180 keV for 24 MeV ^{36}Cl/^{36}S. This estimation could be outperformed by measuring values down to 157 keV, corresponding to a relative energy resolution of 0.66%.

Based on the results from [Mar12] the contribution of the gas to the total uncertainty was estimated to be about 170 keV. The evaluation of the experimental data from the new detector suggests to revise this assumption. With regard to the other contributions, which were theoretically calculated and partly also measured (contribution of the beam and the electronics), the contribution of the gas has to be smaller. By subtracting these contributions (beam, window, electronics) quadratically from the total resolution, a combined contribution due to geometrical effects and the gas calculates to about 143 keV. Unfortunately, it is hard to disentangle the interrelations between geometrical effects and the influence of the detector gas. Assuming, that the estimations concerning the geometrical influences are of the right order ($20 - 30$ keV), a contribution of the gas of about 140 keV seems to be plausible.

The aim of simplifying the detection setup for the suppression of sulfur against chlorine also could be achieved by omitting the silicon strip detector (cf. [Mar12, page 32 ff]). With the new ionization chamber an equal sulfur suppression factor of 11000 at 50% chlorine detector efficiency was obtained. By optimizing the length of the individual anodes some additional improvement of this separation performance can be expected.

Due to the modular design of MAIC[a] various uses of the detector are possible. Apart from having three different sizes of window holder, especially the mounting of the anodes in slide rails opens up individual setups in the future. Advanced anode designs, like diagonal splitting, possibly can enhance the detector's isobar separation capabilities even more.

For further investigations (e.g. the interrelation between gas and detector ge-

---

[a]Multi Anode Ionization Chamber

ometry and their contribution to energy uncertainty) it would be desirable to have even more convenient tools to modify the detector. Having a kind of feedthrough to manipulate the detector's geometry without breaking the vacuum would considerably speed up the measurements to find new/better setups.

For the purpose of an optimally shaped ion beam, additional diagnostic elements near the detector would be useful. The availability of slits or different types of retractable apertures would allow to tune for a more accurate, "slim" ion beam.

During this work only isobutane was used as counting gas in the detector volume. The use of other gas types like argon, methane and mixtures of them, possibly allows further improvements for some applications.

Additionally, a new gas handling system was built to achive a much more precise and convenient gas regulation.

7 Appendix

7.1 Gauss fit & uncertainties

Expecting a normal distribution for the energy values represented in a spectrum, the resolution of a peak has to be evaluated by fitting a Gauss function. Figure 7.1 illustrates the relevant parameters to calculate the resolution with the following formula:

$$res = \frac{w}{p_{max}} \tag{7.1}$$

w ...   full width at half maximum (FWHM)
p_{max} ...   center of peak maximum
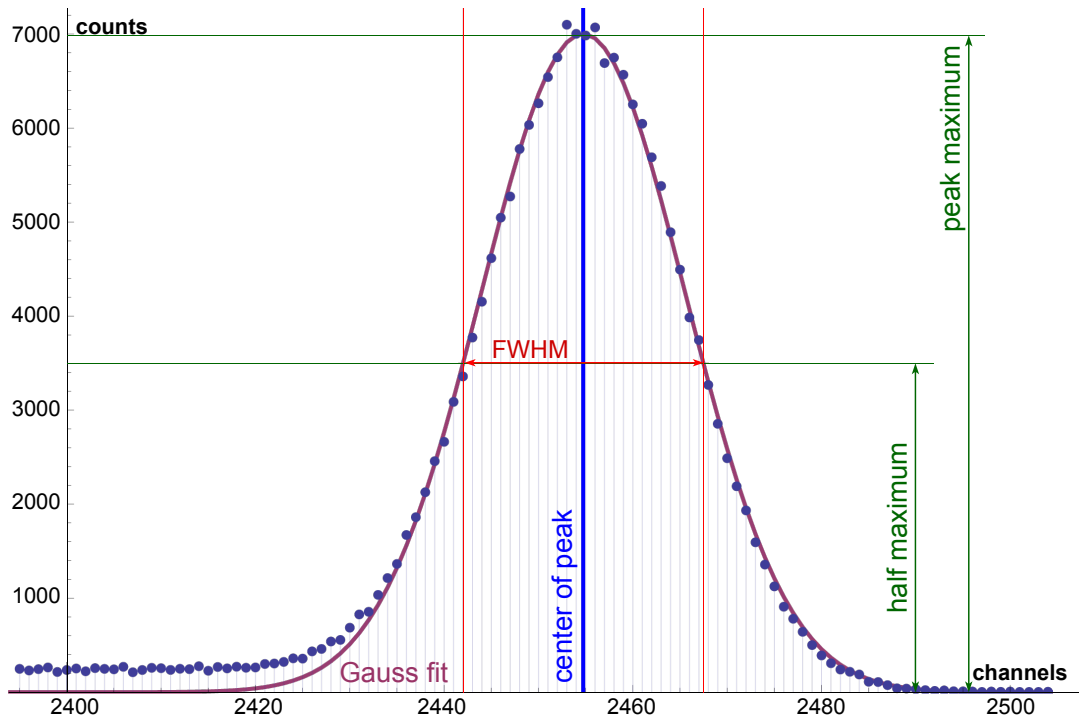
Figure 7.1: Parameters to calculate resolution of a Gaussian-shaped peak. Values for the illustrated example: 189784 counts belonging to the fitted Gauss function, center of peak = 2454.74±0.03 [ch], FWHM = 25.47±0.07 [ch], resolution = 1.037±0.003%.

In order to speed up this fitting procedure and to standardize the assessment of the uncertainties of the calculated values, I wrote a Mathematica routine automatically evaluating the data.
One can select which spectra shall be summed and how they have to be weighted. Based on these data the routine evaluates the center of the highest peak in the range where the sum peak is supposed to be. With the obtained channel number and a selectable fit width (typical $\pm 3\sigma$) the following Gauss function is fitted:

$$f(x) = \frac{1}{\sigma A} e^{-\frac{1}{2}\left(\frac{x-\mu}{\sigma}\right)^2} \tag{7.2}$$

The uncertainties received for the fitted parameters (μ = maximum, σ = standard deviation) are compared with an error estimation following from the statistical model of a Poisson distribution (σ correlates with the square root of the number of events associated with a peak). All indicated uncertainties in this work are the maximum of these two values.

7.2 Value tables & example files

The following column labels are used in the tables listed in this section[a]:

run-path	path in the measurement directory, where the data-files are stored, the name of the measurement usually is given in the caption
time	time, when measurement (run) was started
gpr	gas pressure of isobutane in mbar
counts	counts belonging to fitted Gauss function
Ua	voltage of the anodes in V
Ug	voltage of the grid in V
Ep	upper field strength in V/cm
Eq	lower field strength in V/cm
s	ratio of upper to lower field strength
peakcenter [ch]	channel number of the maximum (center) of the fitted Gauss function $\pm$ absolute uncertainty
FWHM [ch]	full width at half maximum of the fitted Gauss function $\pm$ absolute uncertainty
resolution [%]	total resolution (cf. formula 7.1) $\pm$ absolute uncertainty

---

[a]cf. variable definitions in table 3.1 (page 25) and/or figure 3.5 (page 33)

run-path	time	gpr	counts	peakcenter [ch]	FWHM [ch]	resolution [%]
cat10\run0014	12:58	30.0	712838	5001.41 ± 0.08	42.24 ± 0.18	0.845 ± 0.004
cat10\run0015	13:09	30.0	411316	5000.72 ± 0.06	41.57 ± 0.15	0.831 ± 0.003
cat13\run0016	13:16	30.0	696290	4999.10 ± 0.07	42.75 ± 0.17	0.855 ± 0.003
cat10\run0020	14:01	30.0	482892	4994.85 ± 0.06	41.93 ± 0.15	0.839 ± 0.003
cat10\run0031	14:50	25.0	443241	4701.69 ± 0.05	54.52 ± 0.11	1.160 ± 0.002
cat10\run0032	14:57	25.0	373130	4703.34 ± 0.05	54.41 ± 0.13	1.157 ± 0.003
cat13\run0033	15:04	25.0	363974	4705.03 ± 0.05	54.07 ± 0.13	1.149 ± 0.003
cat10\run0037	15:56	25.0	453720	4706.53 ± 0.05	54.27 ± 0.11	1.153 ± 0.002
cat10\run0038	16:03	25.0	332895	4706.19 ± 0.05	54.63 ± 0.12	1.161 ± 0.003
cat13\run0039	16:09	25.0	353241	4705.45 ± 0.05	54.97 ± 0.12	1.168 ± 0.003
cat10\run0043	16:40	25.0	469404	4697.93 ± 0.05	55.11 ± 0.11	1.173 ± 0.002
cat10\run0044	16:53	25.0	440249	4696.92 ± 0.05	55.00 ± 0.13	1.171 ± 0.003
cat13\run0045	17:00	25.0	367564	4697.06 ± 0.05	55.18 ± 0.12	1.175 ± 0.003
cat10\run0076	17:59	20.0	350948	4123.49 ± 0.07	75.65 ± 0.15	1.835 ± 0.004
cat10\run0077	18:05	20.0	326554	4124.24 ± 0.07	75.82 ± 0.16	1.838 ± 0.004
cat13\run0078	18:11	20.0	304846	4124.96 ± 0.07	75.80 ± 0.17	1.838 ± 0.004
cat13\run0079	18:18	20.0	284059	4125.87 ± 0.08	76.32 ± 0.18	1.850 ± 0.004
cat10\run0083	19:08	20.0	413507	4125.75 ± 0.06	75.94 ± 0.14	1.841 ± 0.003
cat10\run0084	19:14	20.0	341852	4125.81 ± 0.07	75.88 ± 0.16	1.839 ± 0.004
cat13\run0085	19:27	20.0	336353	4126.37 ± 0.06	76.33 ± 0.15	1.850 ± 0.004
cat13\run0086	19:32	20.0	314710	4125.84 ± 0.07	75.73 ± 0.16	1.835 ± 0.004
cat10\run0090	20:14	20.0	364732	4125.68 ± 0.06	75.72 ± 0.14	1.835 ± 0.003
cat10\run0091	20:20	20.0	280125	4126.43 ± 0.07	75.96 ± 0.16	1.841 ± 0.004
cat13\run0092	20:26	20.0	256445	4127.38 ± 0.07	75.92 ± 0.16	1.839 ± 0.004
cat13\run0093	20:32	20.0	283462	4127.00 ± 0.06	76.00 ± 0.15	1.841 ± 0.004
cat10\run0097	22:01	20.0	293003	4123.85 ± 0.07	75.89 ± 0.17	1.840 ± 0.004
cat10\run0098	22:07	20.0	149727	4123.40 ± 0.09	75.88 ± 0.22	1.840 ± 0.005
cat13\run0099	22:14	20.0	215960	4124.32 ± 0.07	75.66 ± 0.17	1.835 ± 0.004
cat13\run0100	22:19	20.0	268002	4125.29 ± 0.07	75.92 ± 0.17	1.840 ± 0.004

Table 7.1: Detector resolution with 24.0 MeV ^{36}S ions at different gas pressures ("MAIC_test_Cl", ca. 5000 cps, $p = 7$ mm, $q = 49$ mm, $U_a = 300$ V, $U_g = 210$ V, $E_p = 129$ V/cm, $E_q = 42.9$ V/cm, s = 3.0, cf. figure 5.7).

run-path	time	counts	peakcenter [ch]	FWHM [ch]	resolution [%]
cat05\run0350	19:42	470948	5010.73 ± 0.09	33.51 ± 0.21	0.669 ± 0.004
cat05\run0351	19:56	338794	5010.92 ± 0.09	33.40 ± 0.21	0.667 ± 0.004
cat06\run0352	20:09	590854	5010.28 ± 0.09	33.64 ± 0.21	0.672 ± 0.004
cat06\run0353	20:25	512223	5010.81 ± 0.09	33.52 ± 0.22	0.669 ± 0.004
cat11\run0354	20:39	305841	5010.40 ± 0.09	33.70 ± 0.21	0.673 ± 0.004
cat11\run0355	20:48	231789	5011.36 ± 0.09	33.67 ± 0.21	0.672 ± 0.004
cat12\run0356	20:56	219184	5011.86 ± 0.10	33.60 ± 0.23	0.670 ± 0.005
cat12\run0357	21:09	166881	5012.03 ± 0.09	33.48 ± 0.22	0.668 ± 0.004
cat13\run0358	21:22	182384	5011.76 ± 0.10	33.33 ± 0.23	0.665 ± 0.005
cat13\run0359	21:34	189255	5011.70 ± 0.09	33.45 ± 0.21	0.667 ± 0.004
cat24\run0360	21:47	63728	5011.69 ± 0.11	32.98 ± 0.27	0.658 ± 0.005
cat24\run0361	22:00	56765	5012.12 ± 0.10	33.58 ± 0.23	0.670 ± 0.005

Table 7.2: Data for reproducibility measurements with Cl-samples at 24.0 MeV ("MAIC_test_Cl3", gas pressure = 30.0 mbar, $p = 8$ mm, $q = 39$ mm, $U_a = 255$ V, $U_g = 140$ V, $E_p = 144$ V/cm, $E_q = 35.9$ V/cm, $s = 4.0$, cf. figure 5.8).

run-path	time	Ua	Ug	Ep	Eq	counts	peakcenter [ch]	FWHM [ch]	resolution [%]
cat37\run0038	16:08	250	175	107.1	35.7	109486	3970.84 ± 0.05	34.05 ± 0.11	0.857 ± 0.003
cat37\run0039	16:10	200	140	85.7	28.6	109531	3964.49 ± 0.05	33.87 ± 0.11	0.854 ± 0.003
cat37\run0040	16:13	150	105	64.3	21.4	108139	3946.94 ± 0.06	34.29 ± 0.14	0.869 ± 0.004
cat37\run0041	16:16	100	70	42.9	14.3	106226	3883.06 ± 0.07	37.02 ± 0.16	0.953 ± 0.004
cat37\run0042	16:19	400	280	171.4	57.1	107153	3970.72 ± 0.05	34.33 ± 0.12	0.864 ± 0.003
cat37\run0043	16:22	350	245	150.0	50.0	106505	3971.83 ± 0.05	34.08 ± 0.11	0.858 ± 0.003
cat37\run0044	16:26	300	210	128.6	42.9	105382	3971.86 ± 0.05	34.08 ± 0.11	0.858 ± 0.003
cat37\run0045	16:29	250	175	107.1	35.7	104436	3970.15 ± 0.05	33.82 ± 0.13	0.852 ± 0.003

Table 7.3: Data for comparison of different field strengths with 7.2 MeV ^{10}Be/^{10}B ions ("MAIC_test_Be2", gas pressure = 50 mbar, $p = 7$ mm, $q = 49$ mm, $s = 3.0$, cf. figures 5.9 and 5.10).

run-path	time	Ua	Ug	Ep	Eq	s	counts	peakcenter [ch]	FWHM [ch]	resolution [%]
cat03\run0001	21:25	250	175	107.1	35.7	3.0	51282	4930.69 ± 0.10	35.43 ± 0.24	0.718 ± 0.005
cat03\run0002	21:27	200	140	85.7	28.6	3.0	50943	4929.47 ± 0.10	35.82 ± 0.25	0.727 ± 0.005
cat03\run0003	21:29	150	105	64.3	21.4	3.0	54543	4921.90 ± 0.09	35.92 ± 0.20	0.730 ± 0.004
cat03\run0004	21:32	100	70	42.9	14.3	3.0	51933	4884.46 ± 0.09	37.16 ± 0.21	0.761 ± 0.004
cat03\run0005	21:34	400	280	171.4	57.1	3.0	51833	4922.24 ± 0.09	35.81 ± 0.22	0.728 ± 0.004
cat03\run0006	21:37	350	245	150.0	50.0	3.0	54419	4924.26 ± 0.09	35.95 ± 0.22	0.730 ± 0.005
cat03\run0007	21:39	300	210	128.6	42.9	3.0	52485	4927.35 ± 0.08	35.77 ± 0.20	0.726 ± 0.004
cat03\run0008	21:41	250	175	107.1	35.7	3.0	54859	4928.81 ± 0.09	35.89 ± 0.21	0.728 ± 0.004
cat03\run0020	22:31	385	245	200.0	50.0	4.0	53197	4925.19 ± 0.09	35.86 ± 0.20	0.728 ± 0.004
cat03\run0021	22:33	346	221	178.6	45.1	4.0	51729	4927.54 ± 0.10	35.47 ± 0.24	0.720 ± 0.005
cat03\run0022	22:35	307	196	158.6	40.0	4.0	48714	4929.26 ± 0.10	35.90 ± 0.22	0.728 ± 0.005
cat03\run0023	22:37	270	172	140.0	35.1	4.0	56493	4930.60 ± 0.08	35.57 ± 0.19	0.721 ± 0.004
cat03\run0024	22:39	230	147	118.6	30.0	4.0	48019	4931.61 ± 0.09	35.48 ± 0.20	0.719 ± 0.004
cat03\run0025	22:42	194	123	101.4	25.1	4.0	58876	4930.13 ± 0.09	35.71 ± 0.21	0.724 ± 0.004
cat03\run0026	22:44	154	98	80.0	20.0	4.0	50978	4925.76 ± 0.09	35.64 ± 0.21	0.724 ± 0.004
cat03\run0027	22:46	116	74	60.0	15.1	4.0	56251	4905.83 ± 0.09	36.39 ± 0.22	0.742 ± 0.004
cat03\run0028	22:49	77	49	40.0	10.0	4.0	53283	4817.52 ± 0.09	39.45 ± 0.22	0.819 ± 0.005

Table 7.4: Data for comparison of different field strengths with 24.0 MeV ^{36}Cl/^{36}S ions ("MAIC_test_Cl3", gas pressure = 30 mbar, $p = 7$ mm, $q = 49$ mm, cf. figures 5.11 and 5.12).

run-path	time	Ua	Ug	Ep	Eq	s	counts	peakcenter [ch]	FWHM [ch]	resolution [%]
cat37\run0025	14:34	250	175	107.1	35.7	3.0	120825	3968.38 ± 0.04	34.20 ± 0.10	0.862 ± 0.002
cat37\run0026	14:40	225	175	71.4	35.7	2.0	119828	3954.10 ± 0.05	34.02 ± 0.12	0.860 ± 0.003
cat37\run0027	14:48	213	175	54.3	35.7	1.5	118815	3833.31 ± 0.05	34.65 ± 0.12	0.904 ± 0.003
cat37\run0028	14:50	200	175	35.7	35.7	1.0	119010	3318.50 ± 0.05	38.16 ± 0.12	1.150 ± 0.004
cat37\run0029	14:53	350	175	250.0	35.7	7.0	119428	3964.77 ± 0.04	34.16 ± 0.11	0.862 ± 0.003
cat37\run0030	14:56	325	175	214.3	35.7	6.0	119031	3965.76 ± 0.05	34.34 ± 0.11	0.866 ± 0.003
cat37\run0031	14:58	300	175	178.6	35.7	5.0	116991	3966.91 ± 0.05	34.13 ± 0.11	0.860 ± 0.003
cat37\run0032	15:01	275	175	142.9	35.7	4.0	118356	3968.01 ± 0.05	34.19 ± 0.12	0.862 ± 0.003
cat37\run0033	15:04	250	175	107.1	35.7	3.0	121083	3968.73 ± 0.05	34.08 ± 0.12	0.859 ± 0.003
cat37\run0034	15:07	225	175	71.4	35.7	2.0	121385	3953.58 ± 0.05	33.83 ± 0.11	0.856 ± 0.003
cat37\run0047	16:41	150	105	64.3	21.4	3.0	105712	3946.20 ± 0.05	34.46 ± 0.11	0.873 ± 0.003
cat37\run0048	16:44	135	105	42.9	21.4	2.0	105515	3921.54 ± 0.05	34.24 ± 0.12	0.873 ± 0.003
cat37\run0049	16:47	131	105	37.1	21.4	1.7	106548	3882.96 ± 0.06	34.24 ± 0.14	0.882 ± 0.004
cat37\run0050	16:49	127	105	31.4	21.4	1.5	106614	3772.75 ± 0.06	35.10 ± 0.14	0.930 ± 0.004
cat37\run0051	16:52	120	105	21.4	21.4	1.0	107258	3256.30 ± 0.07	38.27 ± 0.16	1.175 ± 0.005
cat37\run0054	17:02	210	105	150.0	21.4	7.0	110702	3948.10 ± 0.05	34.18 ± 0.11	0.866 ± 0.003
cat37\run0055	17:04	195	105	128.6	21.4	6.0	112864	3948.01 ± 0.05	34.26 ± 0.12	0.868 ± 0.003
cat37\run0056	17:07	180	105	107.1	21.4	5.0	112243	3947.96 ± 0.04	34.24 ± 0.10	0.867 ± 0.003
cat37\run0057	17:10	165	105	85.7	21.4	4.0	114612	3947.38 ± 0.06	34.21 ± 0.14	0.867 ± 0.004
cat37\run0058	17:13	150	105	64.3	21.4	3.0	114111	3946.04 ± 0.05	34.38 ± 0.12	0.871 ± 0.003
cat37\run0059	17:16	135	105	42.9	21.4	2.0	114980	3918.93 ± 0.06	34.11 ± 0.13	0.870 ± 0.003

Table 7.5: Data for comparison of different field ratios with 7.2 MeV ^{10}Be/^{10}B ions ("MAIC_test_Be2", gas pressure = 50 mbar, $p = 7$ mm, $q = 49$ mm, cf. figures 5.13 and 5.14).

run-path	date	time	Ua	Ug	Ep	Eq	counts	peakcenter [ch]	FWHM [ch]	resolution [%]
cat03\run0020	17.12.	22:31	385	245	200.0	50.0	53197	4925.19 ± 0.09	35.86 ± 0.20	0.728 ± 0.004
cat03\run0021	17.12.	22:33	346	221	178.6	45.1	51729	4927.54 ± 0.10	35.47 ± 0.24	0.720 ± 0.005
cat03\run0022	17.12.	22:35	307	196	158.6	40.0	48714	4929.26 ± 0.10	35.90 ± 0.22	0.728 ± 0.005
cat03\run0023	17.12.	22:37	270	172	140.0	35.1	56493	4930.60 ± 0.08	35.57 ± 0.19	0.721 ± 0.004
cat03\run0024	17.12.	22:39	230	147	118.6	30.0	48019	4931.61 ± 0.09	35.48 ± 0.20	0.719 ± 0.004
cat03\run0025	17.12.	22:42	194	123	101.4	25.1	58876	4930.13 ± 0.09	35.71 ± 0.21	0.724 ± 0.004
cat03\run0026	17.12.	22:44	154	98	80.0	20.0	50978	4925.76 ± 0.09	35.64 ± 0.21	0.724 ± 0.004
cat03\run0027	17.12.	22:46	116	74	60.0	15.1	56251	4905.83 ± 0.09	36.39 ± 0.22	0.742 ± 0.004
cat03\run0028	17.12.	22:49	77	49	40.0	10.0	53283	4817.52 ± 0.09	39.45 ± 0.22	0.819 ± 0.005

Table 7.6: Data for MAIC.1 at various field strengths with ^{36}Cl/^{36}S at 24.0 MeV ("MAIC_test_Cl3", gpr = 30 mbar, $p = 7$ mm, $q = 49$ mm, $s = 4$, cf. figure 5.15).

run-path	date	time	Ua	Ug	Ep	Eq	counts	peakcenter [ch]	FWHM [ch]	resolution [%]
cat03\run0080	18.12.	13:33	260	185	117.1	45.7	51357	4703.99 ± 0.20	61.74 ± 0.48	1.313 ± 0.010
cat03\run0081	18.12.	13:36	91	59	45.7	15.1	58281	4909.36 ± 0.09	34.37 ± 0.21	0.700 ± 0.004
cat03\run0082	18.12.	13:39	120	78	60.0	20.0	53669	4953.44 ± 0.10	33.35 ± 0.23	0.673 ± 0.005
cat03\run0083	18.12.	13:41	150	98	74.3	25.1	49544	4972.66 ± 0.10	33.45 ± 0.25	0.673 ± 0.005
cat03\run0084	18.12.	13:44	180	117	90.0	30.0	52731	4981.70 ± 0.12	32.98 ± 0.28	0.662 ± 0.006
cat03\run0085	18.12.	13:47	210	137	104.3	35.1	52766	4986.77 ± 0.10	33.48 ± 0.24	0.671 ± 0.005
cat03\run0086	18.12.	13:49	240	156	120.0	40.0	52179	4989.68 ± 0.11	33.33 ± 0.25	0.668 ± 0.005
cat03\run0087	18.12.	13:52	270	175	135.7	44.9	47579	4990.95 ± 0.11	33.40 ± 0.25	0.669 ± 0.005
cat03\run0088	18.12.	13:55	300	195	150.0	50.0	50715	4991.10 ± 0.10	33.44 ± 0.25	0.670 ± 0.005
cat03\run0089	18.12.	13:57	330	215	164.3	55.1	46049	4990.41 ± 0.10	33.40 ± 0.24	0.669 ± 0.005
cat03\run0090	18.12.	13:59	360	234	180.0	60.0	54842	4990.19 ± 0.10	33.42 ± 0.24	0.670 ± 0.005
cat03\run0091	18.12.	14:01	390	254	194.3	65.1	54688	4989.29 ± 0.10	33.54 ± 0.24	0.672 ± 0.005

Table 7.7: Data for MAIC.2 at various field strengths with ^{36}Cl/^{36}S at 24.0 MeV ("MAIC_test_Cl3", gpr = 30 mbar, $p = 7$ mm, $q = 39$ mm, $s = 3$, cf. figure 5.15).

run-path	date	time	Ua	Ug	Ep	Eq	counts	peakcenter [ch]	FWHM [ch]	resolution [%]
cat04\run0301	19.12.	15:48	71	39	40.0	10.0	49612	4775.92 ± 0.11	38.07 ± 0.25	0.797 ± 0.005
cat04\run0302	19.12.	15:50	89	49	50.0	12.6	52752	4869.86 ± 0.08	33.40 ± 0.19	0.686 ± 0.004
cat04\run0303	19.12.	15:52	107	59	60.0	15.1	54370	4912.58 ± 0.11	32.71 ± 0.26	0.666 ± 0.005
cat04\run0304	19.12.	15:54	124	68	70.0	17.4	50556	4932.97 ± 0.10	32.78 ± 0.24	0.665 ± 0.005
cat04\run0305	19.12.	15:56	142	78	80.0	20.0	52044	4946.93 ± 0.09	32.80 ± 0.21	0.663 ± 0.004
cat04\run0306	19.12.	15:58	160	88	90.0	22.6	48070	4955.70 ± 0.11	32.57 ± 0.25	0.657 ± 0.005
cat04\run0307	19.12.	16:00	178	98	100.0	25.1	58202	4962.34 ± 0.10	33.49 ± 0.24	0.675 ± 0.005
cat04\run0308	19.12.	16:03	213	117	120.0	30.0	60736	4968.88 ± 0.09	33.53 ± 0.21	0.675 ± 0.004
cat04\run0309	19.12.	16:05	249	137	140.0	35.1	59160	4972.39 ± 0.11	33.61 ± 0.25	0.676 ± 0.005
cat04\run0310	19.12.	16:08	284	156	160.0	40.0	55954	4974.14 ± 0.11	33.78 ± 0.25	0.679 ± 0.005
cat04\run0311	19.12.	16:10	319	175	180.0	44.9	54094	4974.11 ± 0.11	33.26 ± 0.27	0.669 ± 0.005
cat04\run0312	19.12.	16:12	354	195	198.8	50.0	61394	4973.94 ± 0.10	33.63 ± 0.23	0.676 ± 0.005

Table 7.8: Data for MAIC.4 at various field strengths with ^{36}Cl/^{36}S at 24.0 MeV ("MAIC_test_Cl3", gpr = 30 mbar, $p = 8$ mm, $q = 39$ mm, $s = 4$, cf. figure 5.15).

run-path	date	time	Ua	Ug	Ep	Eq	counts	peakcenter [ch]	FWHM [ch]	resolution [%]
cat04\run0250	19.12.	12:40	256	117	120.0	30.0	59888	4946.52 ± 0.11	35.73 ± 0.25	0.722 ± 0.005
cat04\run0251	19.12.	12:42	300	137	140.5	35.1	52700	4951.50 ± 0.10	35.90 ± 0.24	0.725 ± 0.005
cat04\run0252	19.12.	12:46	342	156	160.0	40.0	50094	4954.29 ± 0.11	36.45 ± 0.25	0.736 ± 0.005
cat04\run0253	19.12.	12:48	383	175	179.5	44.9	58602	4953.98 ± 0.09	37.87 ± 0.21	0.764 ± 0.004
cat04\run0254	19.12.	12:50	85	39	40.0	10.0	51400	4746.35 ± 0.09	37.55 ± 0.22	0.791 ± 0.005
cat04\run0255	19.12.	12:53	107	49	50.0	12.6	52508	4838.05 ± 0.10	34.37 ± 0.23	0.710 ± 0.005
cat04\run0256	19.12.	12:55	129	59	60.5	15.1	48688	4883.84 ± 0.09	34.20 ± 0.21	0.700 ± 0.004
cat04\run0257	19.12.	12:59	149	68	69.7	17.4	47735	4907.85 ± 0.09	33.72 ± 0.22	0.687 ± 0.005
cat04\run0258	19.12.	13:01	171	78	80.0	20.0	52666	4924.46 ± 0.10	34.33 ± 0.24	0.697 ± 0.005
cat04\run0259	19.12.	13:03	193	88	90.3	22.6	46667	4934.46 ± 0.10	34.87 ± 0.24	0.707 ± 0.005
cat04\run0260	19.12.	13:06	215	98	100.5	25.1	53493	4941.30 ± 0.08	35.09 ± 0.20	0.710 ± 0.004

Table 7.9: Data for MAIC.3 at various field strengths with ^{36}Cl/^{36}S at 24.0 MeV ("MAIC_test_Cl3", gpr = 30 mbar, $p = 11.6$ mm, $q = 39$ mm, $s = 4$, cf. figure 5.15).

run-path	date	time	Ua	Ep	s	counts	peakcenter [ch]	FWHM [ch]	resolution [%]
cat03\run0010	17.12.	21:51	200	35.7	1.0	60374	4082.76 ± 0.08	35.70 ± 0.18	0.874 ± 0.004
cat03\run0011	17.12.	21:53	213	54.3	1.5	49650	4658.75 ± 0.09	36.85 ± 0.20	0.791 ± 0.004
cat03\run0012	17.12.	21:55	225	71.4	2.0	57482	4851.10 ± 0.09	36.45 ± 0.21	0.751 ± 0.004
cat03\run0013	17.12.	21:57	250	107.1	3.0	48123	4928.11 ± 0.10	35.79 ± 0.23	0.726 ± 0.005
cat03\run0014	17.12.	22:00	275	142.9	4.0	50748	4931.97 ± 0.09	35.48 ± 0.22	0.719 ± 0.004
cat03\run0015	17.12.	22:03	300	178.6	5.0	50780	4933.64 ± 0.10	35.54 ± 0.24	0.720 ± 0.005
cat03\run0016	17.12.	22:05	325	214.3	6.0	54619	4933.67 ± 0.09	35.71 ± 0.21	0.724 ± 0.004
cat03\run0017	17.12.	22:07	350	250.0	7.0	51431	4934.13 ± 0.09	35.21 ± 0.21	0.714 ± 0.004
cat03\run0018	17.12.	22:13	263	125.7	3.5	56746	4930.34 ± 0.09	35.45 ± 0.21	0.719 ± 0.004
cat03\run0019	17.12.	22:15	238	90.0	2.5	54746	4911.47 ± 0.09	36.11 ± 0.21	0.735 ± 0.004

Table 7.10: Data for MAIC.1 at various field ratios with ^{36}Cl/^{36}S at 24.0 MeV ("MAIC_test_Cl3", gpr = 30 mbar, $p = 7$ mm, $q = 49$ mm, $U_g = 175$ V, $E_q = 35.7$ V/cm, cf. figure 5.16).

run-path	date	time	Ua	Ep	s	counts	peakcenter [ch]	FWHM [ch]	resolution [%]
cat03\run0092	18.12.	14:09	215	107.1	3.0	51218	4991.17 ± 0.11	33.29 ± 0.25	0.667 ± 0.005
cat03\run0093	18.12.	14:12	228	125.7	3.5	53960	4994.36 ± 0.11	32.84 ± 0.27	0.657 ± 0.005
cat03\run0094	18.12.	14:14	240	142.9	4.0	53652	4996.17 ± 0.12	33.20 ± 0.29	0.664 ± 0.006
cat03\run0095	18.12.	14:16	253	161.4	4.5	58069	4996.57 ± 0.10	33.34 ± 0.25	0.667 ± 0.005
cat03\run0096	18.12.	14:18	266	180.0	5.0	56772	4997.55 ± 0.10	33.20 ± 0.24	0.664 ± 0.005
cat03\run0097	18.12.	14:21	291	215.7	6.0	57790	4998.25 ± 0.11	33.41 ± 0.25	0.668 ± 0.005
cat03\run0098	18.12.	14:23	316	251.4	7.0	63294	4998.27 ± 0.11	33.16 ± 0.26	0.663 ± 0.005
cat03\run0099	18.12.	14:25	165	35.7	1.0	57551	4323.62 ± 0.08	35.13 ± 0.20	0.813 ± 0.005
cat03\run0100	18.12.	14:27	171	44.3	1.2	64238	4604.99 ± 0.08	35.61 ± 0.20	0.773 ± 0.004
cat03\run0101	18.12.	14:29	178	54.3	1.5	56771	4810.83 ± 0.10	35.14 ± 0.24	0.730 ± 0.005
cat03\run0102	18.12.	14:32	184	62.9	1.8	62341	4907.00 ± 0.09	34.55 ± 0.22	0.704 ± 0.004
cat03\run0103	18.12.	14:34	190	71.4	2.0	55757	4951.41 ± 0.10	33.84 ± 0.25	0.684 ± 0.005
cat03\run0104	18.12.	14:36	196	80.0	2.2	66099	4974.98 ± 0.10	33.96 ± 0.24	0.683 ± 0.005
cat03\run0105	18.12.	14:38	203	90.0	2.5	58642	4988.84 ± 0.10	33.84 ± 0.24	0.678 ± 0.005
cat03\run0106	18.12.	14:41	209	98.6	2.7	61026	4993.60 ± 0.11	33.13 ± 0.25	0.663 ± 0.005
cat03\run0107	18.12.	14:43	215	107.1	3.0	62392	4995.86 ± 0.11	33.85 ± 0.26	0.677 ± 0.005
cat03\run0108	18.12.	14:45	228	125.7	3.5	69570	4997.61 ± 0.12	33.39 ± 0.27	0.668 ± 0.005

Table 7.11: Data for MAIC.2 at various field ratios with ^{36}Cl/^{36}S at 24.0 MeV ("MAIC_test_Cl3", gpr = 30 mbar, $p = 7$ mm, $q = 39$ mm, $U_g = 140$ V, $E_q = 35.9$ V/cm, cf. figure 5.16).

run-path	date	time	Ua	Ep	s	counts	peakcenter [ch]	FWHM [ch]	resolution [%]
cat04\run0325	19.12.	16:41	169	35.7	1.0	52357	4288.10 ± 0.09	35.38 ± 0.21	0.825 ± 0.005
cat04\run0326	19.12.	16:44	197	71.6	2.0	50507	4926.21 ± 0.10	34.95 ± 0.24	0.709 ± 0.005
cat04\run0327	19.12.	16:45	212	90.0	2.5	56509	4969.99 ± 0.10	34.08 ± 0.24	0.686 ± 0.005
cat04\run0328	19.12.	16:47	226	107.8	3.0	52452	4979.22 ± 0.11	33.64 ± 0.26	0.676 ± 0.005
cat04\run0329	19.12.	16:49	255	144.0	4.0	62749	4981.88 ± 0.11	33.81 ± 0.25	0.679 ± 0.005
cat04\run0330	19.12.	16:51	284	180.0	5.0	61579	4982.37 ± 0.10	33.70 ± 0.23	0.676 ± 0.005
cat04\run0331	19.12.	16:54	313	215.7	6.0	61398	4982.86 ± 0.12	33.81 ± 0.28	0.679 ± 0.006

Table 7.12: Data for MAIC.4 at various field ratios with ^{36}Cl/^{36}S at 24.0 MeV ("MAIC_test_Cl3", gpr = 30 mbar, $p = 8$ mm, $q = 39$ mm, $U_g = 140$ V, $E_q = 35.9$ V/cm, cf. figure 5.16).

run-path	date	time	Ua	Ep	s	counts	peakcenter [ch]	FWHM [ch]	resolution [%]
cat04\run0261	19.12.	13:16	265	107.8	3.0	44960	4951.39 ± 0.09	35.98 ± 0.22	0.727 ± 0.004
cat04\run0262	19.12.	13:18	307	144.0	4.0	44071	4952.26 ± 0.11	36.33 ± 0.25	0.734 ± 0.005
cat04\run0263	19.12.	13:20	349	180.0	5.0	41336	4952.24 ± 0.09	37.01 ± 0.22	0.747 ± 0.005
cat04\run0264	19.12.	13:22	390	215.7	6.0	46920	4950.13 ± 0.10	37.24 ± 0.24	0.752 ± 0.005
cat04\run0265	19.12.	13:24	181	35.7	1.0	40709	4255.56 ± 0.09	37.29 ± 0.21	0.876 ± 0.005
cat04\run0266	19.12.	13:26	203	54.3	1.5	47273	4758.18 ± 0.09	37.35 ± 0.22	0.785 ± 0.005
cat04\run0267	19.12.	13:28	223	71.6	2.0	43200	4898.79 ± 0.11	35.82 ± 0.25	0.731 ± 0.005
cat04\run0268	19.12.	13:29	244	90.0	2.5	43471	4939.93 ± 0.09	35.92 ± 0.22	0.727 ± 0.004
cat04\run0269	19.12.	13:31	265	107.8	3.0	39511	4950.50 ± 0.12	35.22 ± 0.28	0.711 ± 0.006

Table 7.13: Data for MAIC.3 at various field ratios with ^{36}Cl/^{36}S at 24.0 MeV ("MAIC_test_Cl3", gpr = 30 mbar, $p = 11.6$ mm, $q = 39$ mm, $U_g = 140$ V, $E_q = 35.9$ V/cm, cf. figure 5.16).

```
(* Config-File for MAIC-Sim-1f *)
(* ========================== *)

SimName = "TestSim";
Ions = 1000;

(*_____Ion-Properties *)
(*Ion1 = {2, He, 4.002603, 3.};*)
(*Ion2 = {4, Be, 10.013534, 7.2};*)
(*Ion3 = {5, B, 10.012937, 7.};*)
(*Ion4 = {6, C, 14.003242, 10.9};*)
(*Ion5 = {13, Al, 25.986892, 12.};*)
Ion6 = {16, S, 35.967081, 24.07};
Ion7 = {17, Cl, 35.968307, 24.07};
(*Ion8 = {53, I, 128.904988, 18.};*)
(*Ion9 = {92, U, 236.045562, 15.};*)

EnergySigma = 0.000212; (* relative *)
BeamDiameter = 2; (* FWHM in mm *)

(*_____Foil-Stack *)
Foils = 0; (* 0 = no foils *)
FoilThickness = 500; (* nm *)
FoilDesign = "q"; (* "q"=quadratic, ""=circular *)
FoilDia = 7.07; (* diagonal/diameter in mm *)
FoilDensity = 3.1; (* g/cm^3 *)
FoilInterspace = 1; (* mm *)
FoiltoWindowDistance = 3; (* mm *)
FoilPath = "Data_in\\SiN_TRIM.IN"; (* relative path *)
VacuumPath = "Data_in\\Air@1013_TRIM.IN"; (* relative path *)

(*_____Detector-Window *)
WindowThickness = 50; (* nm *)
WindowDesign = "q"; (* "q"=quadratic, " "=circular *)
WindowDia = 7.07; (* diagonal/diameter in mm *)
WindowPath = "Data_in\\SiN_TRIM.IN"; (* relative path *)

(*_____MAIC-Properties *)
GasPressure = 30; (* mbar *)
GasPath = "Data_in\\Isobutan@1013_TRIM.IN"; (* relative path *)
AnodeSplitting = {}; (* mm *)
  Anodes = 3; (* alternative, max. 999 *)
AnodeLengthTotal = 150; (* mm *)

(*_____Outputs *)
(* 0 = no output files will be saved *)
Ranges = 0;
ExyzInc = 0; (* eV *)
CollisionPlot = 0;
ZIPfiles = 1; (* 1 = output files are stored as compressed ZIP-file *)
```

Table 7.14: Configuration file for AutoSRIM giving an impression of the available setup possibilities.

Bibliography

[AB05]   G. Amsel and G. Battistig. The impact on materials science of ion beam analysis with electrostatic accelerators. *Nuclear Instruments and Methods in Physics Research B*, 240:1–12, 2005.

[BCH49]   O. Bunemann, T. E. Cranshaw, and J. A. Harvey. Design of grid ionization chambers. *Canadian Journal of Research*, 27A:191–206, 1949.

[DFG+10]   Franz Dellinger, Oliver Forstner, Robin Golser, Walter Kutschera, Alfred Priller, Peter Steier, Anton Wallner, and G. Winkler. Search for a superheavy nuclide with A=292 and neutron-deficient thorium isotopes in natural thorianite. *Nuclear Instruments and Methods in Physics Research B*, 268:1287–1290, 2010.

[DKS+04]   M. Döbeli, C. Kottler, M. Stocker, S. Weinmann, H.-A. Synal, M. Grajcar, and M. Suter. Gas ionization chambers with silicon nitride windows for the detection and identification of low energy ions. *Nuclear Instruments and Methods in Physics Research B*, 219-220:415–419, 2004.

[FMA+08]   Oliver Forstner, Leonard Michlmayr, M. Auer, Robin Golser, Walter Kutschera, Alfred Priller, Peter Steier, and Anton Wallner. Applications of a compact ionization chamber in AMS at energies below 1 MeV/amu. *Nuclear Instruments and Methods in Physics Research B*, 266:2213–2216, 2008.

[FS93]   R.C. Finkel and Martin Suter. *AMS in the Earth Sciences: Technique and Applications.* Jai, 1993.

[Ful79]   H. W. Fulbright. Ionization chambers. *Nuclear Instruments and Methods*, 162:21–28, 1979.

[Göö08]   Alf Göök. *Investigation of the Frisch-grid inefficiency by means of wave-form digitization.* PhD thesis, Örebro Universitet, 2008.

[IRC79]   IRCU. Average energy required to produce an ion pair, report no. 31, 1979.

[Kut90]   Walter Kutschera. Accelerator mass spectrometry: A versatile tool for research. *Nuclear Instruments and Methods in Physics Research B*, 50:252–261, 1990.

[Mar12]   Martin Martschini. *Development of methods for isobar suppression in AMS and measurements of Cl-36 with the VERA 3-MV-tandem accelerator.* PhD thesis, Universität Wien, 2012.

[Mesa]   Mesytec.   Manual   for   Mesytec   MSI-8. www.mesytec.com/datasheets/MSI-8.pdf.

[Mesb]   Mesytec. Manual for Mesytec preamplifier module MMPR1. www.mesytec.com/datasheets/MMPR1.pdf.

[Mesc]   Mesytec GmbH & Co. KG. www.mesytec.com.

[Mül09]   Arnold Müller. *Entwicklung von universellen AMS Anlagen bei tiefen Energien.* PhD thesis, ETH Zürich, 2009.

[MRA+08]   Petra Milota, Ina Reiche, Duval Alain, Oliver Forstner, Hélène Guicharnaud, Walter Kutschera, Silke Merchel, Alfred Priller, Manfred Schreiner, Peter Steier, Elisabeth Thobois, Anton Wallner, Barbara Wünschek, and Robin Golser. PIXE measurements of renaissance silverpoint drawings at VERA. *Nuclear Instruments and Methods in Physics Research B*, 266:2279–2285, 2008.

[Nat]   National Instruments.   Computer   program   LabVIEW   2011. www.ni.com/labview.

[Orta]   Ortec®. Manual for Precision Pulse Generator 419. www.ortec-online.com/download/419.pdf.

[Ortb]   Ortec®. Manual for Quad 1-kV Bias Supply 710. www.ortec-online.com/download/710.pdf.

[Pas89]   Friedrich Paschen. Über die zum Funkenübertrag in Luft, Wasserstoff und Kohlensäure bei verschiedenen Drücken erforderliche Potentialdifferenz. *Annalen der Physik*, 5:69–75, 1889.

[PBC97]   A. Pansky, A. Breskin, and R. Chechik. Fano factor and the mean energy per ion pair in counting gases, at low x-ray energies. *Journal of Applied Physics*, 82(2):871–877, 1997.

[Say77]   R. O. Sayer. Semi-empirical formulas for heavy-ion stripping data. *Revue de physique appliquée*, 12:1543–1546, 1977.

[SBH78]   H. Schmidt-Böcking and H. Hornung. Energy Straggling of Cl Ions in Gases. *Zeitschrift für Physik A*, 286:253–261, 1978.

[SG78]   G. Schultz and J. Gresser. A study of transport coefficients of electrons in some gases used in proportional and drift chambers. *Nuclear Instruments And Methods*, 151:413–431, 1978.

[SGK$^+$04] Peter Steier, Robin Golser, Walter Kutschera, Alfred Priller, Christof Vockenhuber, and Stephan Winkler. VERA, an AMS facility for "all" isotopes. *Nuclear Instruments and Methods in Physics Research B*, 223-224:67–71, 2004.

[Sil]   Silson Ltd. www.silson.com.

[SSS07]   Hans-Arno Synal, Martin Stocker, and Martin Suter. MICADAS: A new compact radiocarbon AMS system. *Nuclear Instruments and Methods in Physics Research B*, 259:7–13, 2007.

[VGK$^+$05] Christof Vockenhuber, Robin Golser, Walter Kutschera, Alfred Priller, Peter Steier, Katharina Vorderwinkler, and Anton Wallner. The TOF detector for isobar separation at ion energies below 1 MeV/amu. *Nuclear Instruments and Methods in Physics Research B*, 240:490–494, 2005.

[Wol]   Wolfram Research. Computer program Mathematica 8. www.wolfram.com/mathematica.

[ZB08]   James F. Ziegler and Jochen P. Biersack. Computer program SRIM-2008.04. www.srim.org, 2008.

Acknowledgments

At first I want to thank Prof. Robin Golser for giving me the opportunity to do my diploma thesis at the VERA laboratory and making me acquainted to the world of isotope research. I am grateful for the broad support of the whole VERA staff during all stages of my work.
Especially, I want to thank...

...Alfred Priller for guiding me patiently towards concrete solutions and giving me encouragement even in non-physical matters.

...Martin Martschini for performing the measurements with the accelerator, a lot of profound discussions and proofreading this work.

...Peter Steier for multiple suggestions and support, especially with the gas handling system.

...Oliver Forstner for sharing his knowledge on ionization chambers and software related issues.

...the VERA workshop, Ewald Friedl, Johann Lukas, Gabi Obstmayer and Wolfgang Hieß for their pleasant support during the assembling phase.

...Johanna, Manuel and Reinhard for their nice collaboration concerning the gas handling system.

...my colleagues, Edith, Jenny, Klaus, Leonard, Thomas for their contribution to an enjoyable ambiance at the institute.

Finally, I want to thank my friends and parents encouraging me to reorient my professional career towards more challenging tasks.

Curriculum vitae

Name:	**Josef Buchriegler**
Place of birth:	Waidhofen/Ybbs, Austria
Nationality:	Austria

Education

since Sept. 2011:	Diploma thesis at the VERA Laboratory, Faculty of Physics, University of Vienna (supervisor: Prof. Robin Golser): *"Construction of a Multi-Anode Ionization Chamber for AMS at VERA"*
since Oct. 2006:	Diploma study in Physics, University of Vienna
2005 – 2006:	Study in Astronomy, University of Vienna
June 1999:	Graduation (Matura)
1994 – 1999:	Horticultural College and Research Institutes in Vienna
1990 – 1994:	Secondary school in Hollenstein/Ybbs, Austria
1986 – 1990:	Elementary school in Hollenstein/Ybbs, Austria

Working Experience

2002 – 2005:	Technician in landscape gardening at Schubert & Partner Gartengestaltungs GmbH in Vienna
2001 – 2002:	Alternative service at Red Cross in Vienna
1999 – 2001:	Foreman in landscape gardening at Schubert Landschaftsbau GmbH in Vienna
Spring 1997:	3 month practice stay at Roth Pflanzen AG in Kesswil, Switzerland

Conference contributions

Annual ÖPG Meeting, 18 – 21 Sept. 2012, Graz, Austria
"A multi-anode Ionization Chamber for AMS at VERA", presented as talk